Quantitative Measurement of Nanomechanical Properties in Composite Materials

A Dissertation Presented

by

Wei Zhao

to

The Graduate School

in Partial Fulfillment of the

Requirements

for the Degree of

Doctor of Philosophy

in

Mechanical Engineering

Stony Brook University

May 2010

Stony Brook University

The Graduate School

Wei Zhao

We, the dissertation committee for the above candidate for the
Doctor of Philosophy degree, hereby recommend
acceptance of this dissertation.

Dr. Chad S. Korach – Dissertation Advisor,
Assistant Professor, Mechanical Engineering

Dr. Toshio Nakamura – Chairperson of Defense,
Professor, Mechanical Engineering

Dr. Oscar Lopez-Pamies – Member,
Assistant Professor, Mechanical Engineering

Dr. Gary P. Halada – Outside Member,
Associate Professor, Materials Science and Engineering

This dissertation is accepted by the Graduate School

Lawrence Martin
Dean of the Graduate School

Abstract of the Dissertation

Quantitative Measurement of Nanomechanical Properties in Composite Materials

by

Wei Zhao

Doctor of Philosophy

in

Mechanical Engineering

Stony Brook University

2010

In this work, quantitative Atomic force acoustic microscopy (AFAM) was used to measure nanomechanical properties and to determine microstructural morphology in fiber reinforced composites and hard calcified tissue. In carbon fiber reinforced composites, the fiber-matrix interphase is of interest as it affects the primary load-transfer process and thereby bulk mechanical properties of reinforced composites. The study of properties in the interphase region is important for an understanding of the bulk mechanical properties, which have been shown affected by moisture-based environmental degradation. Single point AFAM testing has been used to quantitatively determine elastic properties at the fiber-matrix interphase by taking advantage of the high spatial scanning resolution capable of measuring interphase dimensions. Carbon-fiber epoxy composite samples were degraded in laboratory conditions by exposure to a accelerated hydrothermal degradation environment in deionized water and salt water. Composite degradation has been characterized by the change in the epoxy matrix contact stiffness and the interphase properties. A decrease in matrix stiffness was found to coincide with the environmental exposure and moisture absorption of the samples. Interphase stiffness measurements indicate a constant interphase thickness as a function of environmental exposure. Chemical analysis of the epoxy using FTIR and Raman spectroscopy indicate hydrolysis of the C-O-C and Epoxide bonds which contribute to the decrease in epoxy mechanical properties. Accelerated degradation by salt water and deionized water both resulted in degradation of the epoxy, though the presence of sodium chloride showed less degradation. From SEM, debonding of the fiber-matrix interface was observed to be more severe when exposed to a salt water environment. In performing quantitative AFAM measurements, the effects of tip shape on the contact mechanics at the epoxy interface were found to influence the reported results significantly, and new, power-law body of revolution models of the probe tip geometry have been applied. Due to the low yield strength of polymers compared with other engineering materials, elastic-plastic contact is considered to better represent the epoxy surface response and was used to acquire more accurate quantitative measurements. Visco-elastic contact response was introduced in the boundary condition of the AFAM cantilever vibration model, due to the creep nature of epoxy, to determine time-dependent effects. These methods have direct impact on the quantitative measurement capabilities of near-filler interphase regions in polymers and composites and the long-term influence of environmental conditions on composites. In addition, quantitative AFAM scans were made on distal surfaces of human bicuspids and molars, to determine the microstructural and spatial variation in nanomechanical properties of the enamel biocomposite. Single point AFAM measurements were performed on individual enamel prism and sheath locations to determine spatial elastic modulus. Mechanical property variation of enamel is associated to the differences in the mineral to organic content and the apatite crystal orientations within the enamel microstructure. Also, variation in the elastic modulus of the enamel ultrastructure was observed in measurements at the outer enamel versus near the dentine enamel junction (DEJ).

Keywords: Elastic modulus, AFM, AFAM, Enamel, Polymer Matrix Composite,
Surface Chemistry, Interface/Interphase, Environmental Degradation

Dedicated to My family

Table of Contents

List of Tables

List of Figures

ACKNOLWLEDGEMENTS

Through my Ph.D study in Stony Brook, I have been fortunate to meet many individuals who all have made indelible imprints in this important portion of my academic journey.

First of all, I would like sincerely express my gratitude to Dr. Chad S. Korach, my Ph.D advisor, for his knowledgeable and helpful guidance and mentorship throughout the work on this dissertation. It is him that introduced me into the world of tribology and molded me by his enthusiastic fulfills and creative passions for my future career.

I would also like to thank the members of my dissertation committee, Dr. Toshio Nakamura, Dr. Gary P. Halada, Dr. Oscar Lopez-Pamies for their insightful comments, reviews and mentorships on my work.

Dr. Raman P. Singh and his lab in OSU must be appreciated for manufacturing the carbon fiber reinforced composites specimens in this study.

Throughout this three and half years' research, I have been dedicating on the methodologies and instruments from multiple departments within the engineering disciplines. My great appreciation should credit the researchers that had kindly helped me and sometime scarified their own experimental time on instruments usage, and most importantly shared their expertise opinions. They are, Dr. Brain Choi, Mr. Chris Young, Dr. Yang Tan and Dr. Gary P. Halada from Materials Science and Engineering Department; Mr. Yu Zhang and Dr. Robert Jonhson from Chemistry Department; and Dr. Wurigen Bo from Applied Mathmatics Department. Special thanks shall go to Dr. Jim Quinn, who trained me valuable sample preparation techniques and SEM, both of which had enlightened me with some incredible improvements for this research.

One of my unique appreciations goes to the unique senior lab colleague in the nanotribology laboratory, Dr. Joo Hoon Choi, with who, our widely collaborations and broad discussions had greatly benefited this presented research. I would also like to highlight my thanks to my other lab colleagues, Karl Nelson, Changhong Cao, Cunyou lu, Puiying Lo and Chris Bergho, all of them let me enjoy unforgettable joyful collaborations on researches. It is also my great pleasure to work with my other group members, Oliver Sha, Yangro Lee, Hani, Richard Anger. Together, I would like to thank the lab members in all for their warm hearts and amities that make the lab as home to me.

Dr. Ling Liu from Columbia University must be attributed for his diligent helps and bridging me the opportunities to access broader research literature reading.

I must not forget the pertinent and prompt assistance of the Graduate Program Secretaries, Ms. Diane Van Tronk and MaryAnn Caprari on their academic and administrative orientations and helps. A special appreciation should credit to Ms. Diane Van Tronk, who had brought my Ph.D studies with many joys besides academics. Grateful thanks shall go to the departmental sectaries, Ms. Castelbuono, Melissa and Ms. Kuhn, Augusta for many of their kindness helps.

Acknowledgement should also given to the support of this work by National Science Foundation Award CMMI-0626025, without it I could not have experienced and enjoyed this three and half years' enjoyable research journey.

Last but not least, all my love goes to my wife Fanfan Meng for her unselfish endurance, support, and given up her own Ph.D opportunities at University of Waterloo for family reunion, and especially for her devotion to our lovely daughter. The deepest love is for my lovely daughter, Joanna Zhao, who has the strongest passion of meeting her parents at the other hemisphere of earth through video cameras for the past year. I am sincerely indebted to my parents and parents-in-law who had been dedicating in taking care of my daughter at their families. It is their unconditional supports that encouraged me to accomplish this research in such a short time. Thank all of you!

Chapter One

Introduction

Traditional mechanical testing techniques have created databases of bulk material properties and benefited engineering and manufacturing applications. With the growth of new materials, especially for composites that contain multiple phases, the need for mechanical testing instruments that can provide detailed property information at many scales are essential to the understanding of the overall material properties. Among many of the newly developed mechanical instrumentations, atomic force acoustic microscopy (AFAM) is a promising one that is able to retain submicron resolution in obtaining nanomechanical features. In addition, AFAM is shown to be able to provide quantitative mechanical measurement. Therefore, in this thesis, quantitative elastic property measurement has been performed on some of the critical submicron regions in composites by taking advantage of the high scanning resolution of AFAM. To provide more accurate quantitative characterization, contact mechanics analysis with new geometry effects and elastic-plastic and visco-elastic material property effects are addressed.

1.1. Quantitative Nanomechanical Characterization on Composites

1.1.1. Quantitative determination

Among many other techniques, Atomic Force Microscopy (AFM) provides spatial resolution necessary for interfacial measurements in composites between filler and matrix, though AFM techniques can only provide topographic imaging and qualitative determination of surface stiffness by phase imaging or force modulation techniques [1.1-3]. The nanoscratch friction test could be used to determine surface coefficient of friction with nanoindentation instruments though lacks the ability to provide quantitative elastic modulus results [1.4]. AFM phase imaging is shown to be able to detect qualitative modulus changes over the surface on a submicron resolution [1.2]. Though AFM based indentation could perform quantitative elastic measurements, the large radius curvature tips are not sufficiently small to offer high enough resolution for composite interphase measurements [1.5]. Atomic Force Acoustic Microscopy (AFAM), which combines an ultrasonic excitation and retains the same excellent lateral resolution of AFM, is able to achieve quantitative mechanical property measurements [1.6-10].

AFAM with an ultrasonic transducer that emits longitudinal acoustic waves [1.10], in conjunction with an AFM (NT-MDT SolverProM) has been simplified to achieve convenience analytical solution[1.1, 11-12], though a non-linear representation of the surface forces would be necessary [1.13]. Atomic force acoustic microscopy (AFAM) has been successfully applied to imaging material differences of and thin film polymers [A8,9][1.14-15], patterned wafers [1.16], thin-film magnetic ferrite grains [1.17], and nanocrystalline Ni [1.18], with order of nanometer resolution in measuring features. The two-folded advantages that include spatial resolution on the order of the probe tip size (~20 nm) and minimal to no plastic indentation, improve the spatial accuracy and resolution of the measured mechanical properties.

1.1.2. AFAM quantitative determination on Tooth Enamel

The nanomechanical properties of dental enamel are important for understanding the effects on restorative dental materials and other foreign particles or objects on the enamel. The enamel microstructure is known as a composite of mineralized material and bio-polymers formed by organized prisms surrounded by sheaths [1.19-20]. Beside AFM, the micro-indentation tests has been extensively applied on measurement of the hardness and other mechanical properties on enamel surfaces[1.21-22]. A critical region that may govern the strength and toughness of enamel is the interplay between the sheath and prism regions of the structure. [1.19-21, 23-25]. Stiffness differences of the sheath and prism have been shown by AFM-based nanoindentation, at the scale of the indenter tip, which is on the order of 100's of nanometers [1.26-29]. AFM has been used to measure the enamel topography and for mechanical testing techniques, including, AFM-based nanoindentation of hardness and elastic modulus [1.27, 29-30], force modulation of the DEJ [1.31], nanoscale friction across prism and sheaths [1.32], and the piezo-electric response of enamel crystals [1.33]. Due to the variations from the prism to sheath occurring at small length scales estimated to be on the order of a few 100 nanometers, the AFAM technique with length scale resolution below 100 nm is appropriate to probe mechanical properties of the enamel microstructure.

1.1.3. Environmental Degradation of Carbon Fiber Reinforced Composite Interphase

It is critical for composites to prove their superior mechanical characteristics in terms of long-term durability when used in harsh and demanding environmental conditions for infrastructure and other engineering structural applications, however, moisture is found to be absorbed by most polymer matrices and interphase and leads to changes in their mechanical characteristics [1.6-7, 9, 34-38].

The interphase region, which is on the order of micrometers between a fiber and matrix in epoxy composites, controls the fundamental load-transfer and makes the quantitative measurement of the mechanical properties at interphases of critical importance. AFAM that retains the same excellent lateral resolution of a scanning probe microscope has exhibited its ability to characterize the epoxy interphase as a function of degradation time [1.8, 39].

Due to the necessity of time to test samples in real-time environments and determine durability, accelerated environmental degradation chambers and moisture immersion techniques have been employed to decrease the amount of exposure time [1.40-42]. The quantitative comparison of salt and deionized water as the source of environmental degradation is also important since composite materials will potentially be introduced in different environments.

1.1.4. Chemical Analysis of Epoxy Degradation

Raman spectroscopy and Fourier transform infrared spectroscopy (FTIR) are spectroscopic techniques used to study vibrational, rotational, and other low-frequency modes in desired sample materials[1.43]. Both of techniques can be used to identify bonding conditions, identify compounds, or investigate sample composition.

The employment of Raman and FTIR are used to assist the qualitative identification of the chemical damage that governs the mechanical degradation of epoxy when exposed to environmental conditions. Epoxies are susceptible to attack by polymer hydrolysis process, wherein backbone polymer chains are “cut” by bonding with water [1.44-46]. Polymer hydrolysis with the scission of susceptible molecular groups reacted with H_2O, may be caused by acid, base or enzyme catalysts. It has been demonstrated that the Raman and FTIR analysis can be utilized to achieved the chemical understanding of the reactions in coatings[1.47-49] polymers[1.50-51] and especially EPON862 [1.52].

1.2. Contact Mechanics Effects in AFAM Quantitative Determination

1.2.1. Elastic Contact Models

High resolution AFAM nanomechanical measurements on an epoxy matrix is a technique which can be used to measure environmental degradation effects [1.8]. Contact mechanics at the tip-sample interface are essential to accurate quantitative determination of elastic properties. Two commonly employed quantitative AFAM techniques, Hertzian and flat punch models [1.8, 10, 53], which assume hemispherical and flat tip shapes respectively, exhibit large variations in results with applied load [1.12, 54]. Scanning electron microscope obtained probe geometry for quantitative elastic modulus determination, indicates the power law body of revolution model would fit the probe profile in a better form than the previous two models[1.55-56]. Due to the fact that the probe geometry is unpredictable, the study of geometry effects measurements are addressed by different types of tip shapes, in order to find a suitable contact mechanics model in conjunction with geometry profiles.

A high static applied load is often required for accurate AFAM quantitative elastic modulus measurements[1.57]. The quantitative analysis which primarily relies on the probe geometry, needs to consider the probe wear during the contact measurement. Moreover, contact mechanics models that are less sensitive to applied load will allow smaller applied loads and thus minimize the probe wear, increasing the resolution of AFAM probes into finer measurements and longer usage time. Reference materials with already known elastic modulus can be used in AFAM quantitative elastic modulus determination as a more reliable approach than traditional methods without comparisons [1.53, 58-59].

1.2.2. Elastic-Plastic Contact Effects on AFAM Analysis

As a result of the high applied load for AFAM testing, plastic deformation will be introduced while the elastic contact is still playing a important role, thereby, the elastic-plastic contact investigation is critical for accurate quantitative determination[1.53, 60-63]. Contact pressure distribution in the elastic-plastic contact had been studied by many efforts analytically and numerically [1.53, 60, 64-65]. The analytical solution of elastic-plastic contact conditions is advantageous to quantitative AFAM analysis and also for the fundamental contact stiffness understanding. The investigation on elastic-plastic contact for different probe geometries is implemented using the geometric models that have been introduced in this study[1.66]. The results of the elastic-plastic contact models are compared with the elastic models results, showing an improvement for specific probe geometries.

1.2.3. Visco-Elastic Contact Effects on AFAM Analysis

The visco-elastic response of polymer materials has been introduced into the AFAM quantitative analysis in many studies [1.67-69]. Investigations have characterized the visco-elastic properties often in a vibrational model [1.70-71]. This is valid when the applied load is sufficient small and the deflection of the cantilever is within the same order of magnitude to the vibration amplitude. In our quantitative studies, the cantilever deflection due to vibration is negligible due to the required high loads, and thus the efforts for visco-elastic models are focused in this study. The simplest visco-elastic models (Maxwell and Kelvin-Voigt) and complex conditions that includes Standard Linear Solid, the Delayed Elasticity and Maxwell–Weichert contact conditions[1.13, 68-69] will be considered in this study, for achievement of visco-elastic quantitative AFAM determination.

1.3. Outline of this work

In this work, quantitative atomic force acoustic microscopy (AFAM) was used to measure the nanomechanical properties on the prism and sheath regions of enamel tooth, as well as the matrix and matrix-fiber interphase region of composites. AFAM scans were made on distal surfaces of human bicuspids and molar, and matrix phase and interphases in carbon fiber reinforced epoxy composites.

For the enamel, the single point AFAM testing was performed on individual prism and sheath locations. For the measurement of premolar and molar, mean modulus results of the prismatic enamel and the enamel sheath were both measured on the surface outer enamel. On the molar, quantitative results of the transverse surfaces and inner surfaces close to DEJ regions have achieved along with the top surface to better understand enamel mechanical property variation throughout the tooth.

AFAM single point measurements was performed on carbon fiber reinforced composite samples exposed to accelerated moisture-temperature environmental degradation, in boiling deionized and sea water. The contact stiffness measurements have been performed on the matrix and the matrix interphase region surrounding the fibers. Changes in contact stiffness for the matrix epoxy and dimensions of the interphase as a function of exposure time observed the effects of environmental degradation on the fiber-matrix interphase region.

The AFAM quantitative analysis that primary relies on the geometry measurement and contact mechanics models is sensitive to applied load variations. The power law body of revolution model is introduced and compared with the two commonly employed models, Hertzian and flat punch. Associated with different AFAM probe and size, the validation of these contact mechanics principals are discussed. In addition, the elastic-plastic analysis is introduced to these models as the contact pressures reach the yield stress during AFAM quantitative determination of epoxy. Due the nature of the measured polymer material, Epon 862, the visco-elastic effects on the experimental measurements are studied. Since the contact resonance frequency is not able to be acquired in a precise time manner, the damping coefficient is introduced but not calculated in the studied visco-elastic models.

1.4 References

[1.1] Wright Ob, Nishiguchi N. Vibrational dynamics of force microscopy: Effect of tip dimensions. Applied Physics Letters. 1997;71:626-8.

[1.2] Gao S-L, Mäder E. Characterisation of interphase nanoscale property variations in glass fiber reinforced polypropylene and epoxy resin composites. Composites: Part A. 2002;33:559-76.

[1.3] Ying Wang, Thomas H. Hahn. AFM characterization of the interfacial properties of carbon fiber reinforced polymer composites subjected to hygrothermal treatments. Composites Science and Technology. 2007;67:92–101.

[1.4] Kim Jk, Hodzic A. Nanoscale characterisation of thickness and properties of interphase in polymer matrix composites. Journal Of Adhesion. 2003;79(4):383-414.

[1.5] Vanlandingham, M. R., Dagastine, R. R., Eduljee, R. F., Mccullough, R. L., Gillespie, J. W. Characterization of nanoscale property variations in polymer composite systems: 1. Experimental results. CompositesPart A. 1999;30:75-83.

[1.6] Liao K, Shultheisz Cr, Hunston Dl, Brinson Lk. Long-term Durability of Fiber-Reinforced Polymer-Matrix Composite Materials for Infrastructure Applications: A Review. SAMPE Journal of Advanced Materials 1998;30(4):3-40.

[1.7] Jones Fr. Durability of Reinforced Plastics in Liquid Environments. In: Pritchard G, editor. Reinforced Plastics Durability: Woodhead Publishing Company; 1999. p. 70-110.

[1.8] Hurley Dc, Shen K, Jennett Nm, Turner Ja. Atomic force acoustic microscopy methods to determine thin-film elastic properties. Journal of Applied Physics. 2003;94(4):2347-54.

[1.9] Springer Gs. Environmental Effects on Composite Materials: Technomic; 1984.

[1.10] Rabe U, Amelio S, Kester E, Scherer V, Hirsekorn S, Arnold W. Quantitative determination of contact stiffness using atomic force acoustic microscopy. Ultrasonics. 2000;38:430-7.

[1.11] Rabe U, Janser K, Arnold W. Vibrations of free and surface-coupled atomic force microscope cantilevers: Theory and experiment. Review of Scientific Instruments. 1996;67:3281-93.

[1.12] Yamanaka K, Nakano S. Quantitative elasticity evaluation by contact resonance in an atomic force microscope. Applied Physics Materials a- Science & Processing. 1998;66:313-7.

[1.13] Hirsekorn S, Rabe U, Arnold W. Theoretical description of the transfer of vibrations from a sample to the cantilever of an atomic force microscope. Nanotechnology. 1997;8(2):57-66.

[1.14] Hirsekorn S, Arnold W. High-resolution materials characterization by conventional and near-field acoustic microscopy. Ultrasonics. 1998;36(1-5):491-8.

[1.15] Ngwa W, Luo W, Kamanyi a, Fomba Kw, Grill W. Characterization of polymer thin films by phase-sensitive acoustic microscopy and atomic force microscopy: a comparative review. Journal of Microscopy-Oxford. 2005;218:208-18.

[1.16] Rabe U, Arnold W. Acoustic Microscopy by Atomic-Force Microscopy. Applied Physics Letters. 1994;64(12):1493-5.

[1.17] Kester E, Rabe U, Presmanes L, Tailhades P, Arnold W. Measurement of mechanical properties of nanoscaled ferrites using atomic force microscopy at ultrasonic frequencies. Nanostructured Materials. 1999;12(5-8):779-82.

[1.18] Hurley Dc, Geiss Rh, Kopycinska-Muller M, Muller J, Read Dt, Wright Je, Jennett Nm, Maxwell As. Anisotropic elastic properties of nanocrystalline nickel thin films. Journal of Materials Research. 2005;20(5):1186-93.

[1.19] Tencate Ar. Oral Histology: Development, Structure, and Function. 4th ed: Mosby; 1994.

[1.20] Miles Aew. Structural and Chemical Organization of Teeth, Vol. II: Academic Press 1967.

[1.21] Xu Hhk, Smith Dt, Jahanmir S, Romberg E, Kelly Jr, Thompson Vp, Rekow Ed.

Indentation damage and mechanical properties of human enamel and dentin. J of Dental Res. 1998;77:472-80.

[1.22] Park S, Wang Dh, Zhang D, Romberg E, Arola D. Mechanical properties of human enamel as a function of age and location in the tooth. J of Matls Sci: Matls in Med. 2008(19):2317-24.

[1.23] Meckel Ah, Griebstein Wj, Neal Rj. Structure of mature human dental enamel as observed by electron microscopy. Arch Oral Biol. 1965;10:775-84.

[1.24] Meckel Ah, Griebstein Wj, Neal Rj. Ultrastructure of fully calcified human dental enamel. In Tooth enamel, its composition, properties and fundamental structure (eds. Stack MV, Fearnhead RW): John Wright; 1962.

[1.25] Arola Dd Bajaj D. On the R-curve behavior of human tooth enamel. Biomaterials. 2009;30:4037-46.

[1.26] Willems G, Celis Jp, Lambrechts P, Braem M, Vanherle G. Hardness and Young's modulus determined by nanoindentation technique of filler particles of dental restorative materials compared with human enamel. J Biomed Matls Res. 1993(27):747-55.

[1.27] Habelitz S, Marshall Sj, Marshall Gw, Balooch M. Mechanical properties of human dental enamel on the nanometer scale. Arch Oral Biol. 2001;46:173-83.

[1.28] Cuy Jl, Mann Ab, Livi Kj, Teaford Mf, Weihs Tp. Nanoindentation mapping of the mechanical properties of human molar tooth enamel. Arch Oral Biol. 2002;47:281-91.

[1.29] Ge J, Cui Fz, Wang Xm, Feng Hl. Property variations in the prism and organic sheath within enamel by nanoindentation. Biomaterials. 2005;26:3333-9.

[1.30] Lippert F, Parker Dm, Jandt Kd. In vitro demineralization/remineralization cycles at human tooth enamel surfaces investigated by AFM and nanoindentation. J Colloid Interf Sci. 2004;280(442-448).

[1.31] Balooch G, Marshall Gw, Marshall Sj, Warren Ol, Asif Sa, Balooch M. Evaluation of a new modulus mapping technique to investigate microstructural features of human teeth. J Biomech. 2004;37:1223-32.

[1.32] Habelitz S, Marshall Sj, Marshall Gw, Balooch M. The functional width of the dentino-enamel junction determined by AFM-based nanoscratching. J of Struct Biol. 2001;135:294-301.

[1.33] Rodriguez Bj, Kalinin Sv, Shin J, Jesse S, Grichko V, Thundat T, Baddorf Ap, Gruverman A. Electromechanical imaging of biomaterials by scanning probe microscopy. J Struct Biol. 2006;153:151-9.

[1.34] Hodzic a, Stachurski Zh, Kim Jk. Nano-indentation of polymer-glass interfaces Part I. Experimental and mechanical analysis. Polymer. 2000;41(18):6895-905.

[1.35] Hodzic a, Kim Jk, Lowe Ae, Stachurski, Zh. The effects of water aging on the interphase region and interlaminar fracture toughness in polymer-glass composites. Composites Science and Technology. 2004;64(13-14):2185-95.

[1.36] Darvell Bw. Materials science for dentistry. 5th ed. Hong Kong: BW Darvell; 1998.

[1.37] Mary P. Walker, Paulette Spencer, J. David Eick. Mechanical property characterization of resin cement after aqueous aging with and without cyclic loading. Dental Materials. 2003;19:645-52.

[1.38] Kazuto Tanaka, Kohji Minoshima, Witold Grela, Kenjiro Komai. Characterization of the aramid/epoxy interfacial properties by means of pull-out test and influence of water absorption. Composites Science and Technology. 2002;62:2169-77.

[1.39] Rabe U, Amelio S, Kester E, Scherer V, Hirsekorn S, Arnold W. Quantitative determination of contact stiffness using atomic force acoustic microscopy. Ultrasonics. 2000;38(1-8):430-7.

[1.40] Holliday L. Composite Materials. Amsterdam: Elsevier; 1966.

[1.41] Jozef Stabik. Ageing of laminates in boiling NaCl water solution. Polymer Testing 2005;24:101–3

[1.42] Nakamura K, Hatakeyama T, Hatakeyama H. Relationship between hydrogen bonding and bound water in polyhydroxystyrene derivatives. Polymer. 1983;24:871-6.

[1.43] Gardiner, D.J. Practical Raman spectroscopy: Springer-Verlag; 1989.

[1.44] Black J. Biological performance of materials. 3rd ed. New York: Marcel Dekker; 1999.

[1.45] G. Z. Xiao, M. E. R. Shanahan. Water Absorption and Desorption in an Epoxy Resin with Degradation

Journal of Polymer Science: Part B: Polymer Physics. 1997;35:2659-70.

[1.46] Li-Rong Bao, Albert F.Yee. Effect of temperature on moisture absorption in a bismaleimide resin and its carbon fiber composites. Polymer 2002;43:3987-97.

[1.47] Lionel T. Keene, Gary P. Halada, Clive R. Clayton. Failure of navy coating systems 1: chemical depth profiling ofartificially and naturally weathered high-solids aliphatic poly(ester-urethane) military coating systems. Progress in Organic Coatings. 2005;52:173–86.

[1.48] Lionel T. Keene, M. Jaime Vasquez, Clive R. Clayton, Gary P. Halada. Failure of navy coating systems 2: failure pathways of artificially weathered navy coating systems applied to chromate conversion coated AA2024-T3 substrates. Progress in Organic Coatings. 2005; 52:187–95.

[1.49] Lionel T. Keene, Thomas Fiero, Clive R. Clayton, Gary P. Halada, David Cardoza, Tom Weinacht. On the use of femtosecond laser ablation to facilitate spectroscopic depth profiling of heterogeneous polymeric coatings. Polymer Degradation and Stability.

2005; 89:393-409.

[1.50] Hilmar Koerner, Devesh Misra, Ashley Tan, Lawrence Drummy, Peter Mirau, Richard Vaia Montmorillonite-thermoset nanocomposites via cryo-compounding. Polymer 2006;47:3426–35.

[1.51] Maria Partini, Roberto Pantani. FTIR analysis of hydrolysis in aliphatic polyesters. Polymer Degradation and Stability. 2007;92:1491-7.

[1.52] Saeed Ziaee Erik T. Thostenson , Tsu-Wei Chou. Processing and electrical properties of carbon nanotube/vinyl ester nanocomposites. Composites Science and Technology. 2009;69:801–4.

[1.53] K.L. Johnson. Contact Mechanics. Cambridge: Cambridge University Press; 1985.

[1.54] Wei Zhao, Raman P. Singh, Chad S. Korach. Effects of environmental degradation on near-fiber nanomechanical properties of carbon fiber epoxy composites. Composites Part A. 2009;40(5):675-8.

[1.55] L.S. Dongmo, J.S. Villarubia, S.N. Jones, T.B. Renegar, M.T. Postek, J.F. Song. Experimental test of blind tip reconstruction for scanning probe microscopy Ultramicroscopy. 2000;85:141-53.

[1.56] M. Kopycinska-Mu¨ Ller, R.H. Geiss, P. Rice, D.C. Hurley, In: S.V.Kalinin, B. Goldberg, L.M. Eng, B.D. Huey. Scanning-probe and other novel microscopies of local phenomena in nanostructured materials. Materials Research Symposium Proceedings 838E. Warrendale, PA, electronic only publication. p. O-10.6.

[1.57] Malgorzata Kopycinska-Muller, Roy H. Geiss, Donna C. Hurley. Contact mechanics and tip shape in AFM-based nanomechanical measurements. Ultramicroscopy. 2006;106:466-74.

[1.58] F. Stahl, B. Cretin, In: J.P. Jones (Ed.). Acoustical Imaging. Plenum, New York, 1995.

[1.59] Hutter JI, Bechhoefer J. Calibration of atomic-force microscope tips. Rev Sci Instrum 1993;64(7):1868-73.

[1.60] J. Jamari, D. J. Schipper. Experimental Investigation of Fully Plastic Contact of a Sphere Against a Hard Flat. Journal of Tribology. 2006;128:230-5.

[1.61] Poh Chieh Benny Poon. A critical appraisal of nanoindentation with application to elastic-plastic solids and soft materials. Pasadena, California: CALIFORNIA INSTITUTE OF TECHNOLOGY; 2009.

[1.62] Yongwu Zhao, David M. Maietta, L. Chang. An asperity microcontact model incorporating the transition from elastic deformation to fully plastic flow. Journal of Tribology. 2000;122:86-93.

[1.63] Yeau-Ren Jeng, Pei-Ying Wang. An Elliptical Microcontact Model Considering

Elastic, Elastoplastic, and Plastic Deformation. Journal of Tribology. 2003;125:232-40.

[1.64] L. Kogut, I. Etsion. Elastic-plastic contact analysis of a sphere and a rigid flat. Journal of Applied Mechanics. 2002;69:657-62.

[1.65] N. Ye, K. Komvopoulos. Indentation Analysis of Elastic-Plastic Homogeneous and Layered Media: Criteria for Determining the Real Material Hardness. Journal of Tribology. 2003;125:685-9.

[1.66] C. Hardy, C. N. Baronet, G. V. Tordion. The elasto-plastic indentation of a half-space by a rigid sphere. INTERNATIONAL JOURNAL FOR NIJMERICAL METHODS IN ENGINEERING. 1971;3:451-62.

[1.67] P.A.Yuya, D.C. Hurley, J.A. Turner. Contact-resonance atomic force microscopy for viscoelasticity. Journal of Applied Physics. 2008;104(074916):1-7.

[1.68] Win-Jin Chang, Chao-Ming Lin, Jenn-Fa Lee, Shu-Lian Lin. Determination of damping force between atomic force microscope tips and sample using an inverse methodology. Physics Letters A. 2005;343:79-84.

[1.69] Daniel Rupp, Ute Rabe, Sigrun Hirsekorn, Walter Arnold. Nonlinear contact resonance spectroscopy in atomic force microscopy. Journal of Physics D: Applied Physics. 2007;40:7136-45.

[1.70] C-Y Hui, J.M. Baney, E.J. Kramer. Contact Mechanics and Adhesion of

Viscoelastic Spheres. Langmuir 1998;14:6570-8.

[1.71] M. L. Oyen. Analytical techniques for indentation of viscoelastic materials. philosophical Magazine 2006;86:5625-41.

Chapter Two

Nanomechanical Properties of Enamel Microstructure

Quantitative atomic force acoustic microscopy (AFAM) was used to determine the microstructural differences in human enamel and to measure the nanomechanical properties associated with the prism and sheath regions. AFAM scans were made on distal surfaces of human bicuspids and molars, and single point AFAM testing was performed on individual prism and sheath locations. Due to the small probe tip radius and the precise lateral control of the scanning probe, high resolution elastic modulus results were able to be obtained at the prism and sheath using AFAM. For the measurement of the bicuspid and molar samples, modulus of the enamel prism and sheath were measured on the outer enamel surface. Mechanical property variation through the enamel thickness was measured on surfaces parallel and perpendicular to the enamel prisms for locations near the enamel surface on the inner enamel close to the dentine enamel junction (DEJ). General property variation between the sheath and prism is associated with the differences in the mineral to organic content and the apatite crystal orientations within the enamel microstructure.

2.1. Introduction

The mechanical properties of dental enamel are important for understanding the response of restorative dental materials and the interactions of dentifrice and other particles on the enamel surface. The enamel microstructure is a composite of mineralized crystalline hydroxyapatite and bio-polymers formed in parallel rods approximately normal to the tooth surface [2.1]. The rods, also referred to as prisms, extend continuously from the dentine-enamel junction (DEJ) to the surface and consist of a sheath region, richer in organic content, surrounding the prism, which retains a diameter around 5~7 micrometers. The prism contains a three-dimensional variation of the hydroxyapatite crystal orientation, with crystals oriented parallel to the prism in a tail region and perpendicular in the head region (Figure 2.1). A continuous orientation change exists between the prism tail and head. The prism and sheath together create a keyhole-shaped structure when observed with a high resolution microscope [2.1-2]. The enamel microstructure consists of a unit cell containing the prism and sheath regions, where the prism head presents towards the crown of the tooth, and is repeated throughout the enamel bulk. At the prism interfaces, crystal orientation is near 90-degrees different. The prism sheath may act a compliant interface between the incoherent crystal orientations. When observed at the macroscale, the enamel exhibits an ultrastructure consisting of disruptions in the enamel mineralization (e.g. Rentzis lines), prism twisting, and an inner enamel closer to the DEJ [2.2].

For the establishment of bulk enamel modeling and the development of an effective macroscale mechanical response, an understanding of the mechanical properties of the enamel at the microstructural scale is necessary. The effects of the unidirectional prism microstructure have been investigated by microindentation and demonstrated changes in the hardness in the normal (oclussal surface) versus longitudinal (in the cross-section) directions of enamel [2.3]. Indentation in the longitudinal direction has also allowed the identification of a variation in mechanical properties from the inner enamel near the DEJ towards the surface outer enamel [2.4].

A region of interest that potentially performs a critical role in the strength and toughness of enamel is between the sheath (also called the interrod or interprismatic enamel) and prism regions of the microstructure. The sheath is formed at the location of and abrupt variation in the hydryoxyapatite crystal orientation, at the interfaces between prisms. Throughout the prism there is a continuous variation in the hydroxyapatite crystal orientation from the tail towards the head, which points in the direction of the occlusal surface, and also in the perpendicular direction to the sides of the prism centerline [2.5-6]. Sharp interfaces of hydroxyapatite orientation are present and lead to a sheath region that is less structured and high in organic content, and thus believed to be more compliant. Since the crystal orientation is strongly dissimilar (~90º in some locations) along the prism-sheath interface it would be naturally weak and prone to a high degree of failure. The presence of the higher organic content is believed to act as a natural toughening interface in the enamel, slowing down fractures and failure by absorbing energy and impeding fracture growth. Stiffness differences of the sheath and prism have been shown by using AFM-based nanoindentation with probe tip radii on the order of 100 nm [2.7-10]. A full understanding of the structural importance of the separate sheath and prism regions is not complete, though it has been shown that fractures, which are common in enamel, preferentially occur along the prism interfaces (i.e. the sheath) [2.3, 11]. The sheath may act as a toughening region for slowing down and abating fracture growth by a ductile rather than brittle fracture mechanism [2.11].

Length scales of the enamel sheath are estimated to be on the order of a few 100 nm, which is a small percentage of the overall prism diameters. Measurement of sheath properties is limited by techniques which have spatial resolutions of less than 100 nm and small spot sizes. Nanoindentation is an excellent technique for measuring thin film and near-surface material hardness and elastic modulus, though the extent of the plastic zone surrounding an indent could be as much as twice the indent width [2.12]. Interaction of the contact stress field with neighboring prismatic material would yield effective properties of the sheath-prism region, and not sheath properties directly. Due to this, a technique with length scale resolution below 100 nm is necessary to probe mechanical properties of the enamel microstructure.

The use of atomic force microscopy (AFM) has been used to measure enamel topography, AFM-based nanoindentation of enamel hardness and elastic modulus [2.8, 10, 13], force modulation of the DEJ [2.14], nanoscale friction across prism and sheaths [2.15] and the DEJ, piezo-electric response of enamel proteins and HA crystals [2.16], and qualitative acoustic force microscopy of enamel HA crystals [2.17]. In this work, we utilize the high resolution of AFM probes and scanners, combined with an ultrasonic acoustic transducer, to measure quantitative nanomechanical properties of dental enamel prisms and sheaths. Atomic force acoustic microscopy (AFAM) has successfully been applied to imaging material differences of organic thin films [2.18], as well as inorganic materials [2.19-20], measuring features on the order of nanometer resolution. The advantages of AFAM are two-fold, 1), the spatial resolution is on the order of the probe tip size, ~20 nm, and 2), minimal to no plastic indentation is necessary. This improves the spatial accuracy and resolution of the measured mechanical properties over techniques such as nanoindentation. Here, the elastic modulus between the prism and sheath in outer, transverse surfaces, and inner enamel close to the DEJ will be compared using AFAM.

2.2. Quantitative AFAM

2.2.1. AFAM Background

AFAM is performed by insonifying a sample mounted on an ultrasonic transducer that emits longitudinal acoustic waves [2.21], in conjunction with an AFM (NT-MDT SolverProM), shown as Figure 2.2. An AFM cantilever is modeled as a clamped beam with a distributed mass that can vibrate in different modes, such as flexural, torsional, and extensional. Analyzing flexural and torsional vibration modes for the free state can result in closed form solutions of the equations of motion [2.22-24]. If the beam is fixed at any length L_1 and coupled to a surface through a linear spring with stiffness k^*, the altered boundary conditions representing the forces due to tip-sample contact, the equations of motion can be solved analytically using a simplified beam contact model, if amplitudes are kept sufficiently small (Figure 2.3). For larger amplitudes, a non-linear representation of the surface forces would be necessary [2.25]. A representative characteristic equation for the modal flexural stiffness is given as [2.22]:

$$\frac{k^*}{k_c}[-(\cosh k_n L_1 \sin k_n L_1 - \sinh k_n L_1 \cos k_n L_1)(1+\cos k_n L' \cosh k_n L')$$

$$+\left(\cosh k_n L' \sin k_n L' - \sinh k_n L' \cos k_n L'\right)\left(1 - \cos k_n L \cosh k_n L\right)\Big] = 2\frac{\left(k_n L_1\right)^3}{3}\left(1 + \cos k_n L \cosh k_n L\right)$$

(2.1)

where *k** is the tip-sample contact stiffness, *L* is the total cantilever length, L_1 is the tip position along the cantilever, and $L' = L - L_1$. The modal contact stiffness, k_n, is given by equation (2),

$$k_n = c_c\sqrt{f_n} \tag{2.2}$$

where f_n are the vibration frequencies ($n = 1, 2, \ldots$), and c_c is a characteristic cantilever constant,

$$c_c = \sqrt{\frac{48\pi^2\rho}{b^2 E_i}} \tag{2.3}$$

$$k_c = \frac{E_i b^3 a}{4L_1^3} \tag{2.4}$$

which is a function of the silicon cantilever modulus E_i (=169GPa), the cantilever mass density (ρ= 2330 kg m^{-3}) , and the cantilever thickness, *b*. The cantilever spring constant (k_c) can be calculated by the mechanical properties and geometry or a direct method as described in the following section. Typical values of cantilever spring constants used in the AFAM measurements (k_c= 5~20 N/m) are larger than used for contact imaging, allowing higher normal loads to be applied to the contact interface while retaining small cantilever deflection. If smaller k_c values are used, the adhesive interaction forces between the AFM tip and the sample surface are on the same order or larger than the contact forces applied by the cantilever, and must be considered viscous damping and lateral forces can be added into the theoretical model [2.22] though their influence on k^* is small compared with the normal forces and errors generated by tip geometry and position [2.26]. In this study, the applied load is considered at least two orders larger than adhesive forces, which can then be neglected. The resonance frequencies are sensitive to the applied normal loads and increase with applied load due to a stiffer contact created between the tip and sample, though are stable within a certain range of loads.

Utilizing Hertzian contact model, the elastic modulus of the sample surface is calculated, after obtaining the experimental contact stiffness (k*). In the three dimensional Hertz analysis [2.27], the contact is assumed to be a parabolic indenter in contact with a flat surface. The indenter tip and the surface have elastic modulus of E_i and E_s, and Poisson's ratios of v_i (=0.3) and v_s (=0.36), where i and s represent the indenter and the surface, respectively. For a statically applied force, $F_c = k_c \times z$, where z is the cantilever deflection. In our experiments the tip-sample forces F_c are sufficiently large to overcome surface interaction forces to ensure that the elastic contact forces are the main contribution to the analysis. For small deflections, the radius of contact, a_c, and the effective elastic modulus, E^*, are given as, (Figure 2.4)

$$a_c = \sqrt[3]{\frac{3F_c R}{4E^*}} \tag{2.5}$$

$$\frac{1}{E^*} = \frac{1-\nu_s^2}{E_s} + \frac{1-\nu_i^2}{E_i} \tag{2.6}$$

where R is the radius of curvature of the indenter tip. Using equation (2.5) and the mutual approach between surfaces, $\delta = \frac{a^2}{R}$, the contact stiffness can be represented by,

$$k^* = \sqrt[3]{6E^{*2} R F_c} \tag{2.7}$$

and relates the contact stiffness k^* to the sample surface elastic modulus (E_s), as a function of the applied contact force and the probe tip radius of curvature.

The radius of curvature R, can either be directly obtained by measuring the probe tip from high resolution microscopy, e.g. SEM in this study, or indirectly calibrated from reference materials with known material properties [2.28]. Based on the Hertzian contact mechanics model, quantitative results for E_s calculated utilizing the tip curvature measured by SEM is often found higher than the desired results. Similar findings have been report from other’s AFAM quantitative measurement studies[2.29]. These contact mechanics issues will be addressed systemically in Chapter 4. However, the problem of probe tip shape calibration can be addressed by using standard materials as references with similar elastic modulus to quantitatively calibrate R necessary in AFAM quantitative measurements [2.29-30]. In doing so, the consistency of the cantilever mounting conditions and orientation will be guaranteed throughout the measurements. A correct effective tip radius value that bridges the contact stiffness to the quantitative elastic modulus will be calculated, and most importantly, can be conveniently determined as often as needed to monitor tip geometry change. In this study, two materials (silica and indium) were utilized as reference materials. The silica reference, with modulus of 71.6 GPa ([2.31]), is used when measuring tooth enamel, as they have close elastic modulus values to each other. Likewise, for the epoxy and interphase measurements, Indium (E~11 GPa) was used, as the epoxy elastic modulus is often found to be in the range of a few GPa.

2.2.2. Cantilever Selection

Cantilever geometry was measured by combination of scanning electron and optical microscopy. Tip radius of curvature is typically in the range of 10 nm to 100 nm, and was checked for accuracy during experiments [2.22]. Initial topography scanning to locate regions of interest for quantitative testing was performed at low applied loads, making radius of curvature more consistent through out the experiments.

The cantilever spring constant (k_c) measurement is of essential importance, since as equation 2.7 shows, contact force F_c is the only unknown parameter that relates contact stiffness, k^*, and the reduced elastic modulus, E^*. Though AFM cantilever manufacturers provide a typical range for k_c, for accurate nanomechanical results the direct calibration of the spring constant was determined by the thermal turning method [2.32].

To achieve the best sensitivity with the AFAM technique, the ratio of k^* / k_c guides selection of the most appropriate cantilever. Since many materials of quantitative interest contain two or more materials of different stiffness (E_{sheath} is different with E_{prism}, due to the nature of their difference in mineral and protein composition [2.10]), to obtain correct results each material should be measured with a cantilever of an appropriate spring constant. Incorrect cantilever selection can lead to erroneous evaluation of AFAM results, due to contact stiffness (k^*) of tip-material pairs which are out of measurable range. Equation 2.1 can be rewritten as,

$$\frac{k^*}{k_c} = \frac{1+\cos(c_c\sqrt{f_n})\cosh(c_c\sqrt{f_n})}{\sinh(c_c\sqrt{f_n})\cos(c_c\sqrt{f_n}) - \sin(c_c\sqrt{f_n})\cosh(c_c\sqrt{f_n})} \cdot \frac{(c_c\sqrt{f_n})^3}{3} \tag{2.8}$$

and provided a direct relationship between k^*/k_c and the measured resonance frequency. By evaluating equation 2.8 as a function of frequency, the contact stiffness can be plotted in Figure 2.5. The contact stiffness, k^* has singularities of positive and negative infinity at the contact resonance frequencies, which could lead to sensitivity problems in calculating the sample elastic modulus, E_S. This implies that for a specific sample, cantilevers should be chosen with ratios of k^*/k_c to achieve correct results. Large normal loads are found necessary for stable results using AFAM to provide a coherent contact area. Single point testing, where the probe tip lands at a specific measurement location, has been performed for all the quantitative measurements so as not to increase the tip radius of curvature significantly by high load scanning. The landing speed and load have been reduced to minimize the occurrence of fracture due to the landing impact, which is believed to be a major contribution to the tip bluntness. This was experimentally examined by SEM in comparison before and after several landings with different speeds and loads. In this study, rectangular geometry polysilicon cantilevers (AIST fpN11S), were found the most suitable for testing the enamel.

2.3. Tooth Enamel Microstructure and Preparation

2.3.1. Enamel Microstructure

A human tooth is composed of a crown and root portions (see Figure 2.6). Dentin composes most of the tooth structure, with cementum covering the outer root surface, the top surface covered with a 1-2 mm thick enamel [2.1]. The schematic of a molar is depicted in Figure 2.7, showing the typical location of a sample used in the AFAM measurements, and the outer and inner enamel surfaces of the crown (position A and D, respectively). These locations are for measurements normal to the enamel. The transverse enamel surfaces are located in the outer enamel surface and near the DEJ interface (position B and C, respectively).

The polished oclusal surface of outer enamel (Figure 2.8), shows the sheath and prism keyhole structure when observed by optical microscopy. The topographical variation between the sheath and prism are due to the differences in wear resistance to the polishing media. Figure 2.9 is an optical micrograph of the enamel transverse surface. For the transverse surfaces, optical microscopy shows that the enamel prisms are more unidirectional in the outer enamel than the inner enamel region adjacent to the DEJ. Also, a higher surface topography is exhibited in the inner enamel region close to the DEJ surface, which is confirmed with AFM profile scans.

2.3.2 Enamel Sample Preparation

Samples were placed in a container of deionized water and refrigerated at ~ 2~3 ^{o}C, after removal from the original biological support. A 10% ClO_2 solution was used for sterilization. The specimens were machined by diamond saw from the distal sides of adult human bicuspids and molars for AFAM testing. Deionized water lubrication was provided to the specimen surface to reduce friction and heat generation during cutting. Due to the low roughness requirement to obtain results with AFAM, samples underwent metallographic polishing steps with 3 μm, 1 μm, and 0.05 μm alumina particles. Polishing time was ~ 10 minutes total and was only applied long enough to obtain a flat region for testing. Samples were placed in a beaker filled with deionized water and ultrasonically cleaned to remove residual polishing particles remaining on the specimen surface. After polishing and cleaning, sample surfaces were examined by optical microscopy (Keyence VHX-500) to insure a smooth, flat region for testing (Figures 2.8-2.9) where the enamel microstructure was visible. Specimens were attached to the AFAM transducer with honey and allowed to rest for one hour prior to starting measurements. During this period, the sample surface remained hydrated by placing deionized water drops by pipette as needed. Water was added to the surface when a visible meniscus began to disappear. For the molar specimen, which had multiple testing locations, immediately after one surface had been tested the sample was hydrated.

2.4. AFAM Measurements on Enamel

2.4.1 AFAM Scanning

AFAM measurements were performed on 4 separate lactations on enamel surfaces. Contact with the enamel surface commenced immediately after the visible water on top of the sample surface evaporated. This was done to insure the sample surface was kept in a hydrated state as long as possible prior to measurement, though it allowed for the near-surface moisture to have evaporated which can affect adhesive forces. Phase angle changes in the cantilever resonance frequency while in contact with the ultrasonically perturbed enamel specimen were recorded simultaneously with the topography. Surface topography measurements are compared with AFAM results, since large changes in topography can affect the measured phase changes. The enamel sheath and prism, can be identified from the AFM topography images. Height variations occur due to differences in the polishing rate of the sheath and prism regions (Figures 2.10-2.12). Phase images (Figures 2.10~2.12(b)), constructed of the AFAM phase data, show the sheath to have a larger (lighter) phase angle change in comparison with the prisms (darker). For the 10~20 x 10~20 μm scan (Figures 2.10~12(b)), due to the reference frequency point chosen, this translates to a decreased stiffness of the sheath compared with the prism. The phase angle maps in figures 2.10-2.12 are at excitation frequencies of 2536.7 kHz, 1835.2 kHz, 928.386 kHz, respectively, using three different AFM probes (fpN11s, AIST-NT). The transducer frequency was chosen after preliminary observations to provide the best possible signal strength. Though AFAM (and any SPM-based feedback system) is susceptible to artifacts in results created from abrupt height variations, the spatial variations of interest between the prism and sheath are large compared with the probe tip radius and sampling rate. When AFAM scanning is applied to a smaller region of the enamel, on the scale of individual prisms, the difference between prism and sheath becomes more evident. For the AFAM phase angle scanning, probe tip loads were kept at low values (~ 0.5 μN) to avoid wear of the silicon AFM probe. Variations in probe radius directly affect the sample-probe contact area, which affects the contact stiffness. The use of low contact loads to avoid tip wear achieves the most accurate stiffness mapping, though resolution and clarity of variations are affected. To obtain accurate quantitative contact stiffness by AFAM, single point spatial testing is used. The C, B, A, D surfaces were imaged in sequence and AFAM single point testing was performed on these locations. AFAM single point testing used a dedicated probe to measure quantitative surface properties, different than those of the topography scanning. This ensured the pre-characterized probe had a known geometry at the start of testing. The locations of the AFAM point tests were determined using the profile height variation measured between sheath and prisms.

Based on the AFM profile of the surface obtained, the sheath widths on the outer surface (region A) are about 400-500 nm, and at the inner enamel surface (region D), range from 500 nm to 1 m (see Figures 2.10 and 2.11 (c)).

Unlike the normal surfaces of the outer and inner enamel locations, where the enamel microstructure possesses similar size and shape across the surface, the enamel in the transverse surface has more variations. Within the transverse region, different sections of the enamel prism will be present. The center of an enamel prism is represented by the blue arrow in Figure 2.12 (a), and has a uniform width. When the enamel prism have been cut through at an angle or different depths, the cross sectional areas exposed on the surface will have variations. In contrast, for exposed sheaths located at the top and bottom of the prisms (indicated by the black arrow in the Figure 2.12 (a)), a depth on the order of 100 nm is present. It was observed that small regions (~2 x 0.2 μm) in the transverse surfaces exist where enamel comes out vertically to the surface, in the way similar to the top and DEJ surface regions. The topography profile between the prism and sheath regions for locations B and C are deeper (on the order of 50 nm) than for locations A and D. The sheath region in the transverse surfaces is 200 nm to 1 μm in width along the Region B and C.

2.4.2 AFAM Single Point Testing

a) Bicuspids specimens

To achieve quantitative stiffness measurements directly related to materials properties, AFAM single point testing was utilized [2.33]. For the most accurate results, a coherent contact between probe and sample is necessary. To ensure the contact of the probe to the testing surface during ultrasonic vibration, normal loads between the probe and sample are needed that are typically not used in AFM scanning (order of μN). Single point testing not only allows more accurate results, but also avoids changes in the probe tip geometry (radius of curvature), which has been observed for high load scanning. The single point testing utilizes topography images scanned in a semi-contact mode. Based on the AFM topography, regions of interest for prisms and sheaths were identified to perform the AFM point measurements. The semi-contact mode topography scanning imparts very low normal and lateral loads (order of nN) on the sample from the probe, minimizing damage during topography scanning to the sample surface which may alter stiffness measurement results. The distance between testing points were chosen to be at least 100 nm, though spatial resolution on the order of the tip radius (~20nm) is achievable with the technique, shown in Figures 2.13. On the bicuspids specimen, three different applied loads (F_c = 2.9, 3.4, and 3.9 μN) were used to perform spatial point testing on four different locations of prisms and sheaths. When the AFM probe comes in contact with the surface, the cantilever resonance frequency will increase from the free state, as shown in Figure 2.14, due to a change in the cantilever boundary conditions. The contact resonance frequency as the probe is located within different regions of the enamel surface will shift based on the sample stiffness, e.g. from the enamel sheath to the prism, and is demonstrated on the right side of Figure 2.14. From the point contact resonance frequencies for the first vibrational mode, the contact stiffness (k^*) is determined by equations (1-8) as described in section 2.2. The resulting k^* values at different locations of the enamel surface are compiled in Tables 2.1-2.2. Contact stiffness was found to increase with applied normal load, which is expected with Hertzian contact mechanics. The values of the contact stiffness in the enamel prism region showed an overall increase versus the sheath region, and indicate that the single point testing data corresponds to the trend observed in the AFAM scanning results.

b) Molar specimens

In the molar specimens, along with the outer surface (location A), the transverse and inner enamel surfaces are tested with AFAM using cantilevers with spring constant of 7.8 N/m (fpN11s, AIST-NT). The testing for each surface was carried out following by above mentioned mechanical principals and procedures on bicuspids specimen. For molar testing, in concern of AFM probe geometry change due to wear, the distance between testing points were chosen to be at least 150 nm between each testing locations, though spatial resolution on the order of the tip radius (~20-40nm) was determined. Only one applied load (F_c = ~2.5 μN) was used to perform spatial point testing, and 10 different locations of prisms and sheaths in each of the four interested surfaces were tested. Indium (E_L = 11 GPa) was used as a reference material to calibrate the effective radius curvature using Hertzian contact mechanics theory. Following the same approach detailed for the bicuspids testing, the contact stiffness for all four tested regions are listed in Table 2.3. Determination of the probe radii curvature, throughout the experiments was achieved by conducting 4 additional AFAM single point testings at the interval of switching tested A,B,C,D surfaces, and the probe radius of curvature was found to increase from 28 nm (before region C) to

43 nm (after Region D), due to tip wear.

2.4.3. Sample Etching

In our AFAM testing, we tested our molar sample immediately after polishing. Although it was observed that overnight storage in deionized water altered the sample surface. Here, an enamel specimen had been kept in deionized water for ~10 hours after polishing, and then AFAM scanning performed. Here (Figure 2.17), a rougher surface was observed compared with the as polished samples. The sheath width was found to remain consistent, though the roughness results affected the AFAM scanning.

To better depict the sheath region that exhibits less resistance to polishing media, erosive etching had been performed on a molar enamel outer top surface (region A) by placing it in 0.1 mol lactic acid solution for 4 seconds. After the specimen had been thoroughly rinsed and ultrasonically cleaned in deionized water, AFAM scanning was conducted on the specimen. Corresponding AFAM qualitative results are shown in Figure 2.18. The sheath region containing less mineral are eroded less by the lactic acid. This is quantified by Figure 2.18 (c), which shows sheath region height of ~30 nm. Nevertheless, AFAM scanning, demonstrated a variation in the sheath versus prism region though the absolute phase change was lower. This is evidence of an acid softening of the enamel prisms.

2.4.4. Comparison of Elastic Modulus Measurements

The contact stiffness from the AFAM measurements combined with a Hertzian contact model, allows calculation of elastic modulus for the enamel oclussal surface by equations 2.5-2.7 and are presented in Tables 2.1-2.3. The results show that the average prism has a larger elastic modulus than the enamel sheath, both in bicuspids and molar. For the bicuspids sample, the standard deviation in the measurements shown in Figures 2.15 and 2.16 is observed higher in the prism region, this potentially could be due to surface roughness variation affecting the real contact area during measurement.

The enamel prism was found to have a stiffer contact and hence computed elastic modulus than the sheath region surrounding the prism in both the bicuspids and molar samples. The mechanical properties of the contact were found affected by the applied normal load, though the trend in prism modulus remaining larger than the sheath region was consistent for all loads. The dependence could be due to inaccuracy in the contact geometry assumption of the probe tip.

The larger compliance of the enamel sheath correlates with the knowledge that there exists a higher organic content and less mineral than in the prism. The higher mineral content in the prism over the sheath leads to a stiffer material. This has also been observed by nanoindentaion [2.8, 10] of human enamel with AFM-based diamond indenters. These results reported (all in GPa) E^{prism} = 88 +/- 8.6, 77.5 +/- 6.2; E^{sheath} = 86.4 +/- 11.7, 35.4 +/- 3.6, for ref. 8 and 10, respectively. The results compared for [2.10] are re-computed using Eqn. 6, since the author's only presented the average reduced modulus (E_r) results of the prism and sheath. It is interesting to note that the AFAM quantitative results of the elastic modulus reported here are larger in magnitude, though show the same trend of a stiffer prism region. The discrepancy in results could be due to the differences in spatial resolution of the techniques. Nanoindentation, even for shallow plastic indents, creates an apparent contact region on the order of 8 times the indentation depth, based on the Berkovich indenter geometry that was utilized by [2.10]. For the indentation depth of up to 80 nm used, the apparent contact width would be ~640 nm. Habelitz et al. [2.8] utilized a cube-corner (90º) diamond indenter to an indentation depth of 300 nm. This translates to a contact width of ~600 nm. It is clear that the contact width of both the AFM-based indentation studies were of similar value, even though the indentation depths were largely different. Due to the spatial scale of the sheath region being < ~1 μm in width, nanoindentation may interact with the surrounding material at that scale. Furthermore, the actual structural morphology of the organic-rich sheath region is unknown, and it is likely that some functional gradation in the structure will be present across the width. This in turn would generate a rather narrow region to perform indentation on. During nanoindentation, the plastic zone created by the indenter is estimated to be at least twice the width of contact [2.27], and would interact with the biomaterial interface at the intersection of the sheath and prism materials. If this is the case, then the results in the previous AFM-based indentation studies for the sheath would be affected by the stiffer prism interface or even the change in apatite crystal orientation on either side of the sheath. The results by Ge et al. [2.10] for the sheath are much lower than reported here as well as in other nanoindentation results [2.8]. The AFAM technique is able to provide spatial resolution at the scale of the tip radius (~20 nm), which is within the sheath region and will not be affected by the surrounding prism stiffness. The results here show differences in the prism and sheath on the same order as measured in other studies [2.7-8]. The identification of enamel mechanical properties at multiple length scales is important for not only a fundamental understanding of the microstructure of the material, but also as complimentary results used in modeling of enamel at the microstructural scale [2.34], which can be scaled-up to model bulk response of enamel crowns for material wear [2.35], trauma [2.36], and de- and re-mineralization effects on the enamel near-surface.

2.5. Conclusion

Nanomechanical characterization on the surface of human dental enamel using atomic force acoustic microscopy has been performed. The AFAM technique is shown to provide high resolution quantitative measurements on the prism and sheath regions of the enamel microstructure. The contact resonance frequency of the AFM cantilever is used to calculate the elastic modulus with a vibrational beam model in conjunction with Hertzian contact analysis. Elastic modulus was found to have some relationship with applied normal loads, which may be due to inaccuracies in the probe geometry. Prism modulus was consistently found to be larger than the sheath region, and is related to the mineral and organic material content differences The elastic modulus of the enamel transverse surfaces were found to be smaller than either of the inner or outer enamel surfaces, and this had been consistently observed in both the prism and sheath regions. Within the enamel transverse surface, the regions closer to oclussal surface are consistently found to possess higher elastic modulus than closer to the DEJ region. These conclusions are based on consistent measurements found for both the sheath and prism regions. The AFAM technique has been demonstrated to be a promising quantitative nanomaterial technique with high lateral resolution for enamel microstructure measurements.

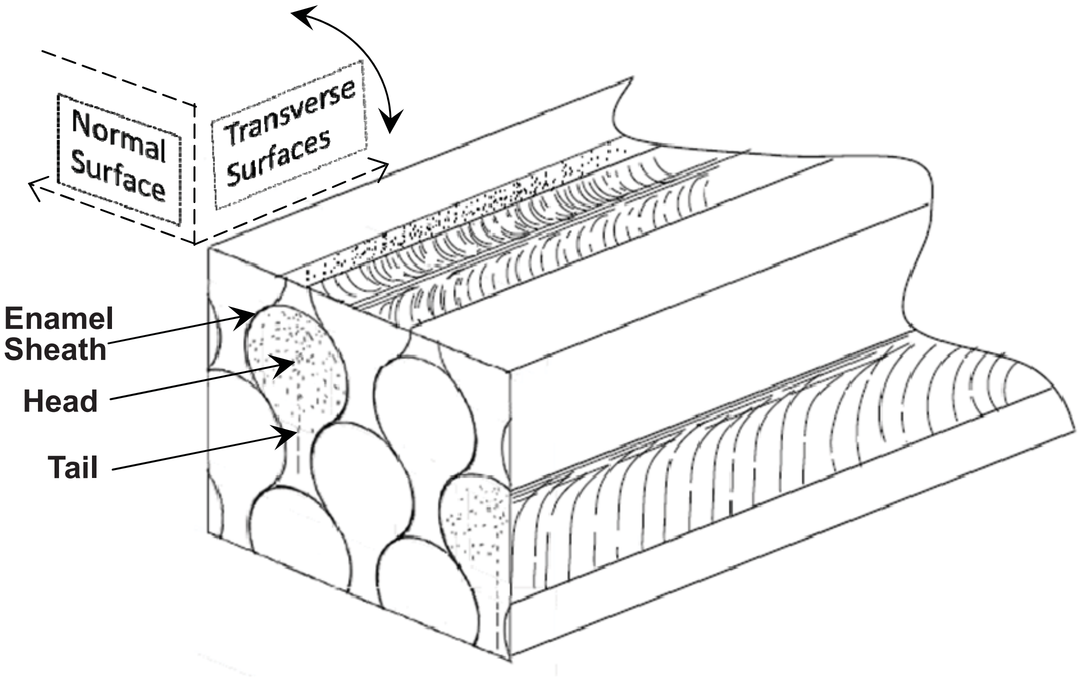

Figure 2.1 Enamel unite cell image.

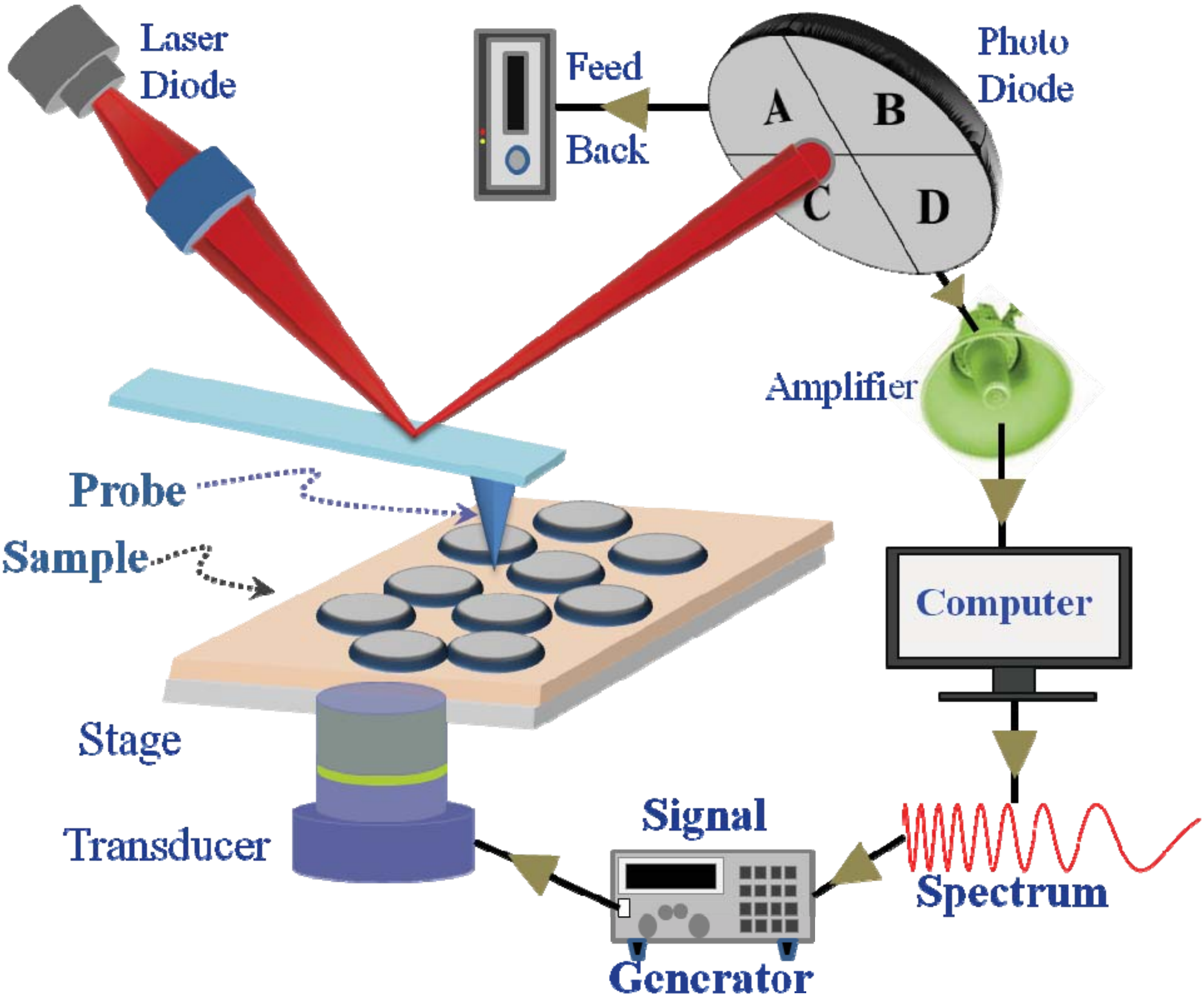

Figure 2.2 Experimental set-up for Atomic force acoustic microscopy (AFAM)

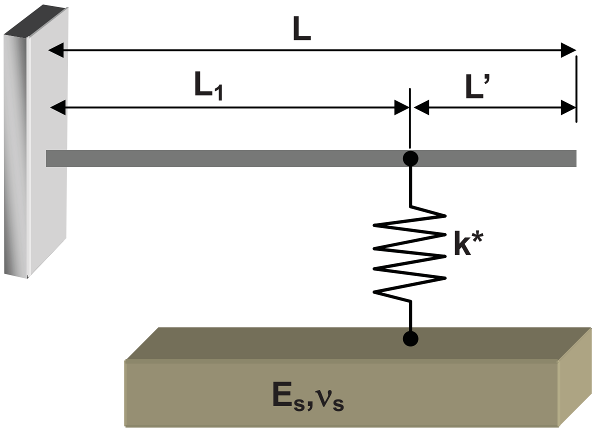

Figure 2.3 Linear flexural model of the AFM cantilever

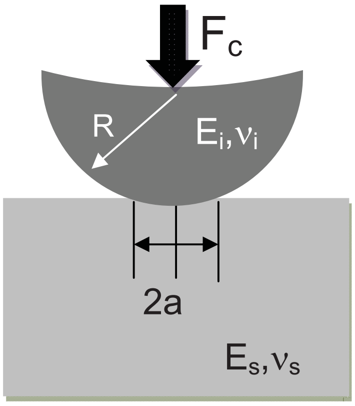

Figure 2.4 Hertzian contact model

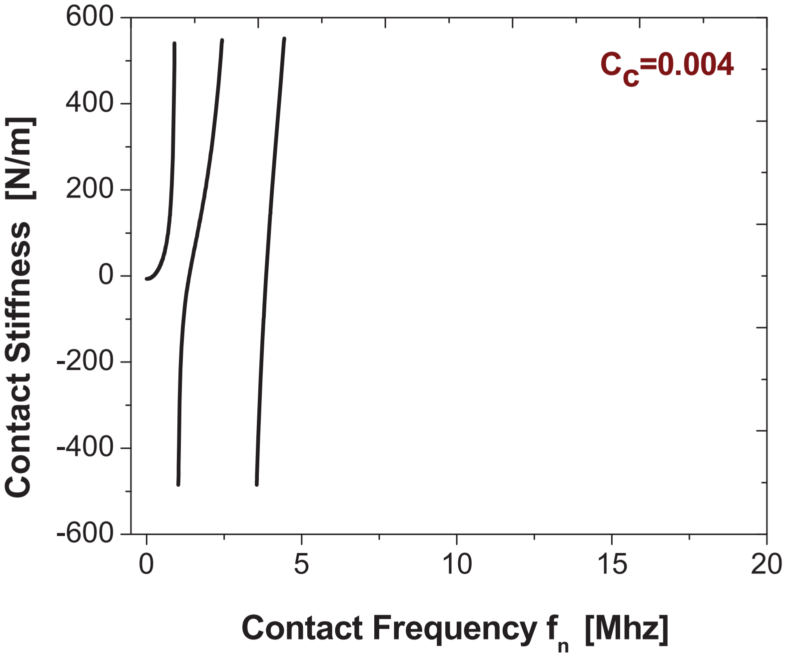
600
400
200
0
-200
-400
-600
Contact Stiffness [N/m]
0
5
10
15
20
Contact Frequency f_n [Mhz]
C_C=0.004

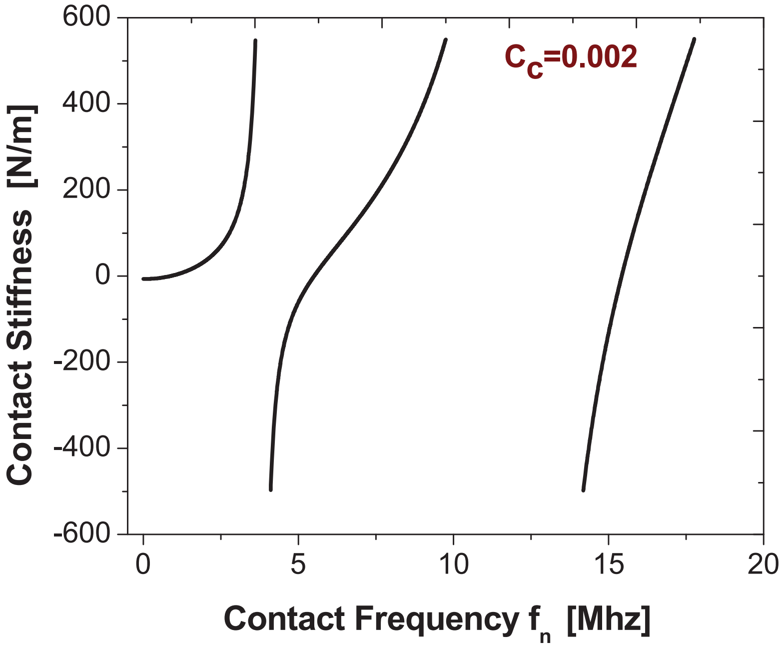
600
400
200
0
-200
-400
-600
Contact Stiffness [N/m]
0
5
10
15
20
Contact Frequency f_n [Mhz]
C_C=0.002

Figure 2.5 Contact stiffness curve for different C_c values

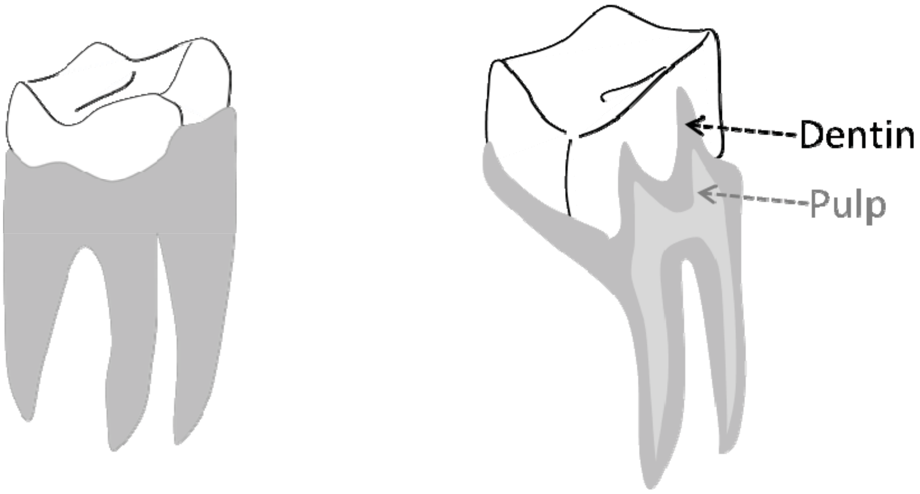

Figure 2.6 Tooth structure a) molar exterior appearance b) molar interior cross-section. Enamel crown is indicated in white, root is grey.

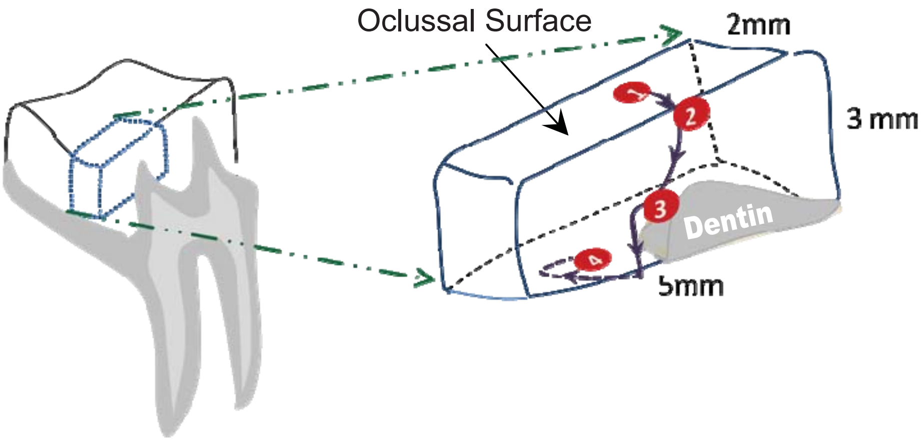

Figure 2.7 Location of sample taken from a molar. The sample contains both the dentin and the enamel crown. Surfaces where measurements are conducted, A) top (oclussal) surface of the enamel crown, B) transverse enamel surface of the outer enamel, C) transverse enamel surface near the DEJ region, and D) inner enamel surface near the DEJ region.

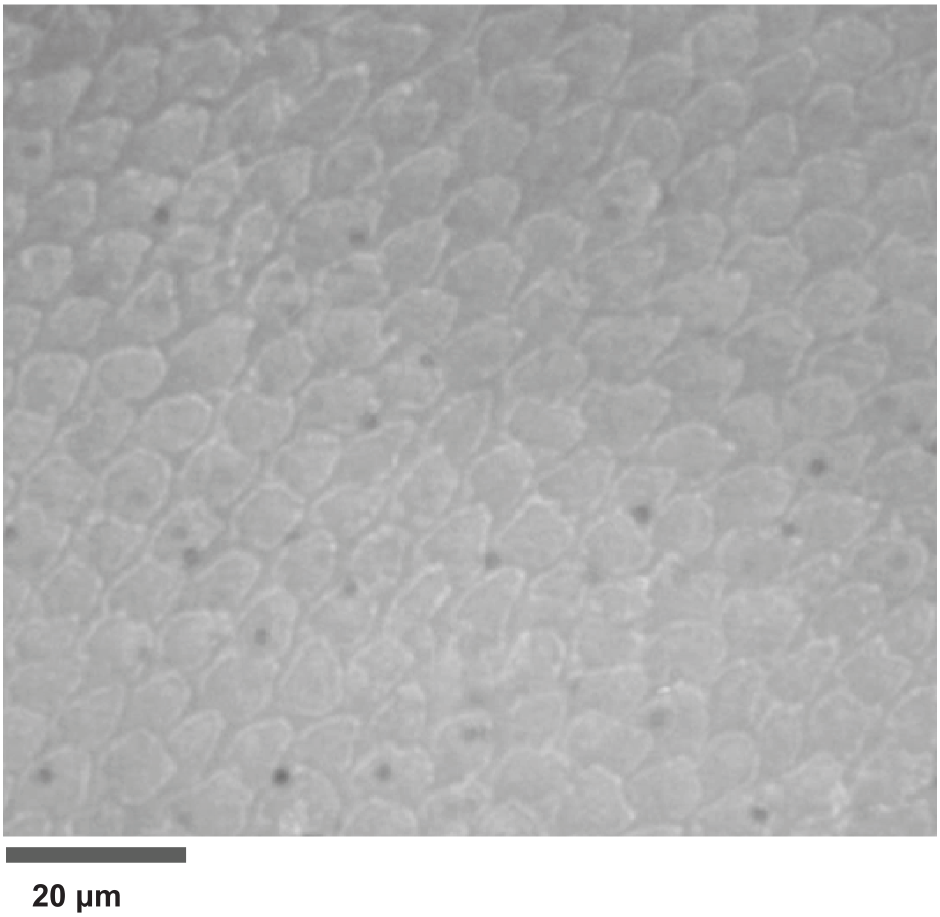

Figure 2.8 Polished outer normal surface of the enamel, where a single prism is ~5 - 7 µm in diameter.

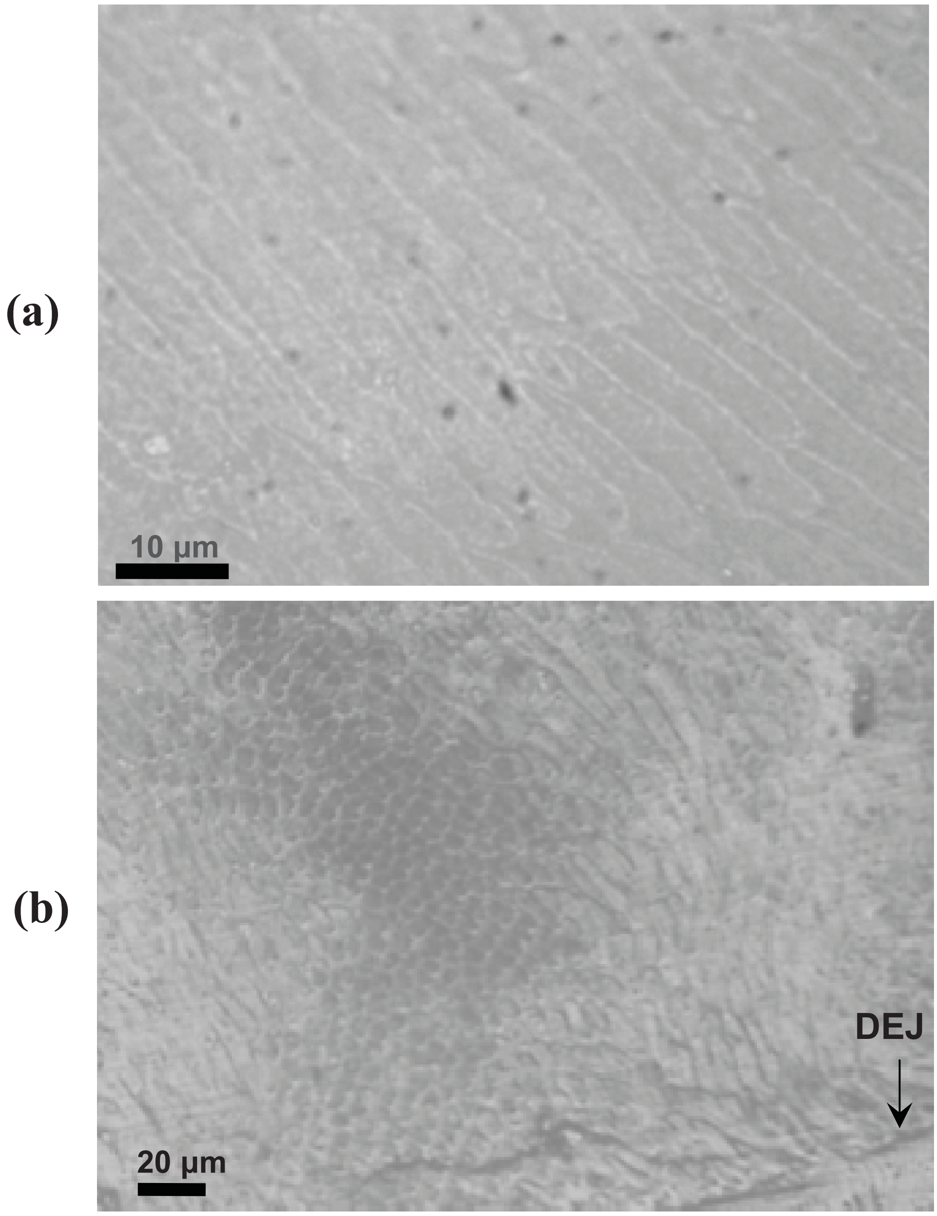

Figure 2.9 Transverse surface of an enamel sample, (a) transverse surface near

the outer enamel, where the prisms are more straight, (b) transverse surface near DEJ, where the rod are more disorganized.

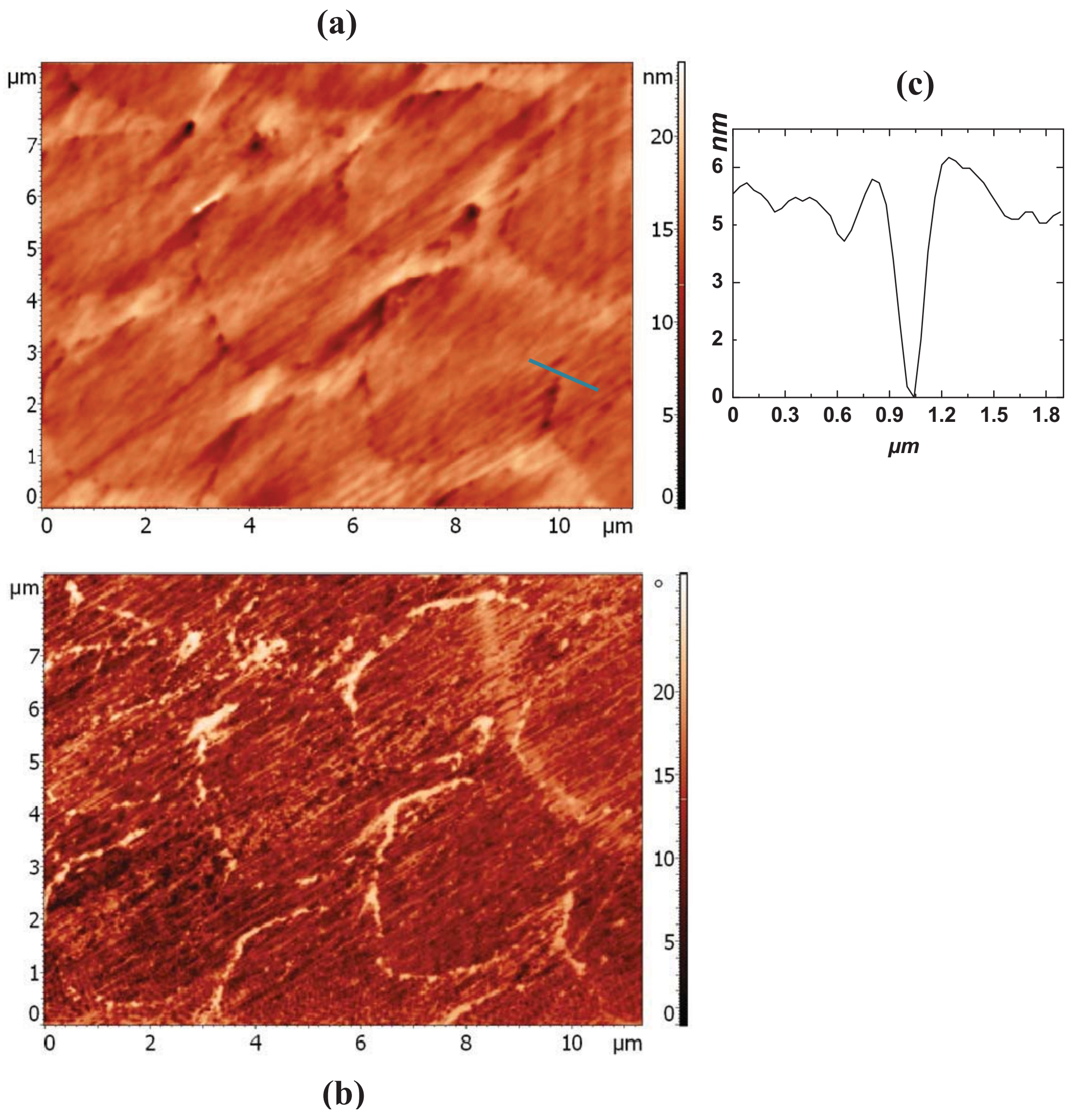

Figure 2.10 Normal surface of outer enamel (region A), a) AFM topography profile of surface, b) AFAM phase image which represents the elastic response, showing a difference between prisms and sheath, c) surface profile change

across the sheath region between prisms corresponding to the line drawn on profile image.

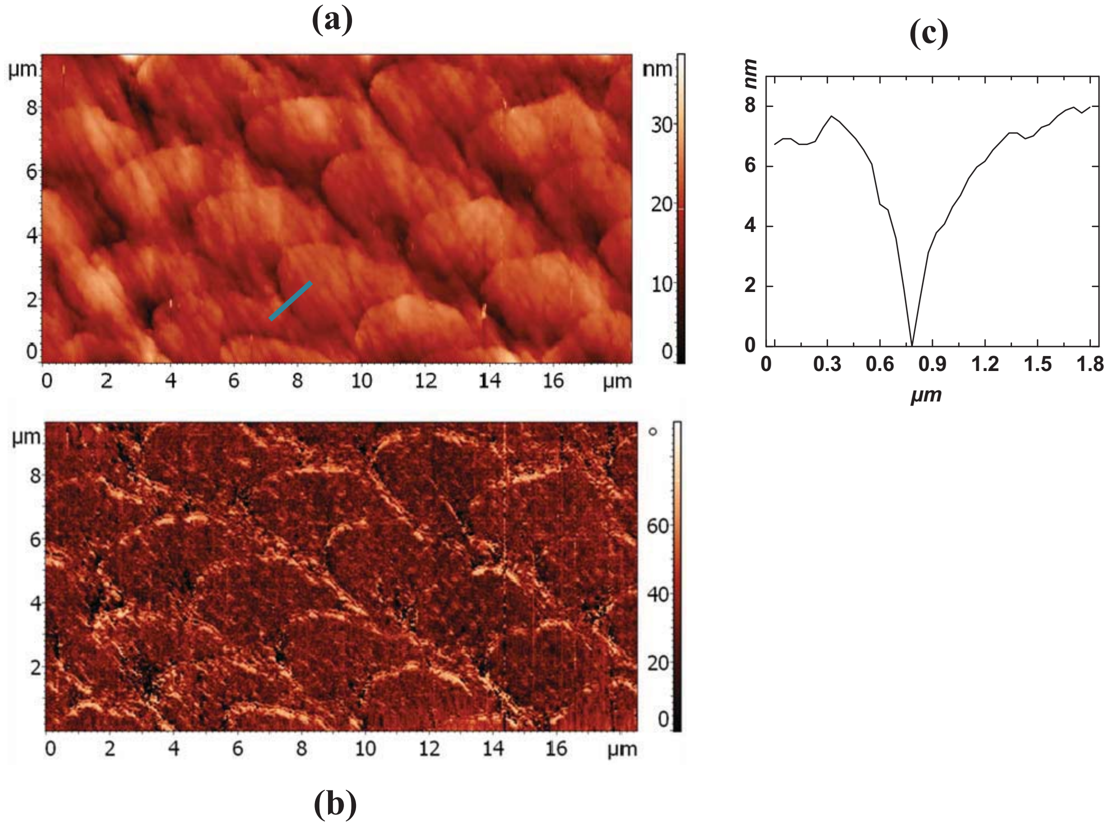

Figure 2.11 Normal surface of the inner enamel region close to the DEJ (region D), a) AFM topography profile of surface, b) AFAM phase image which represents the elastic response, showing a difference between prisms and sheath, c) surface profile change across the sheath region between prisms corresponding to the line drawn on profile image.

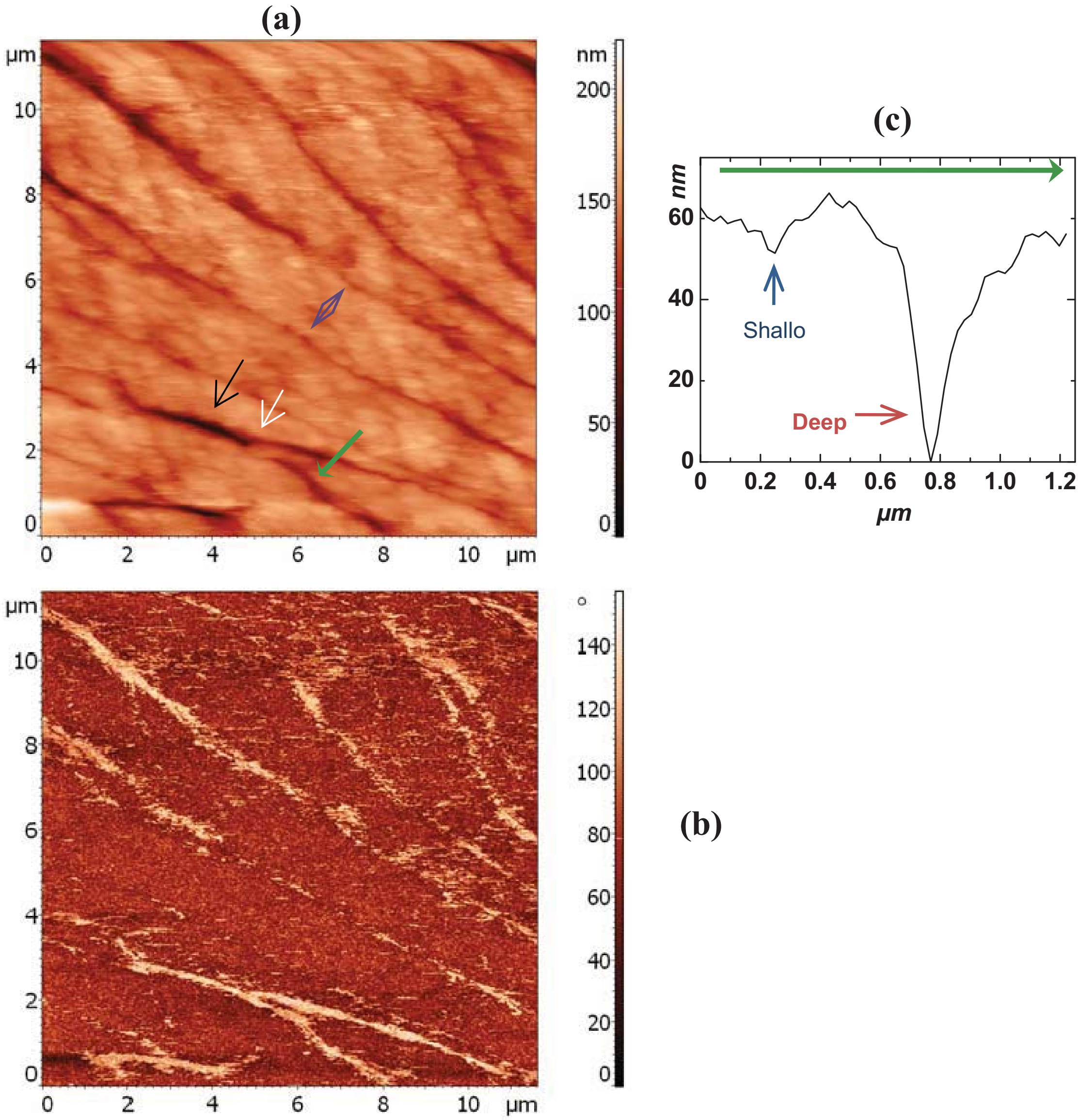

Figure 2.12 Tooth enamel on transverse surfaces (region B, outer, and C, inner enamel), a) AFM topography profile of the surface, b) AFAM phase image which represents the elastic response, showing the difference between prisms and sheath, c) surface profile change across two sheath regions (shallow and deep) between prisms corresponding to the lines drawn on the topography image.

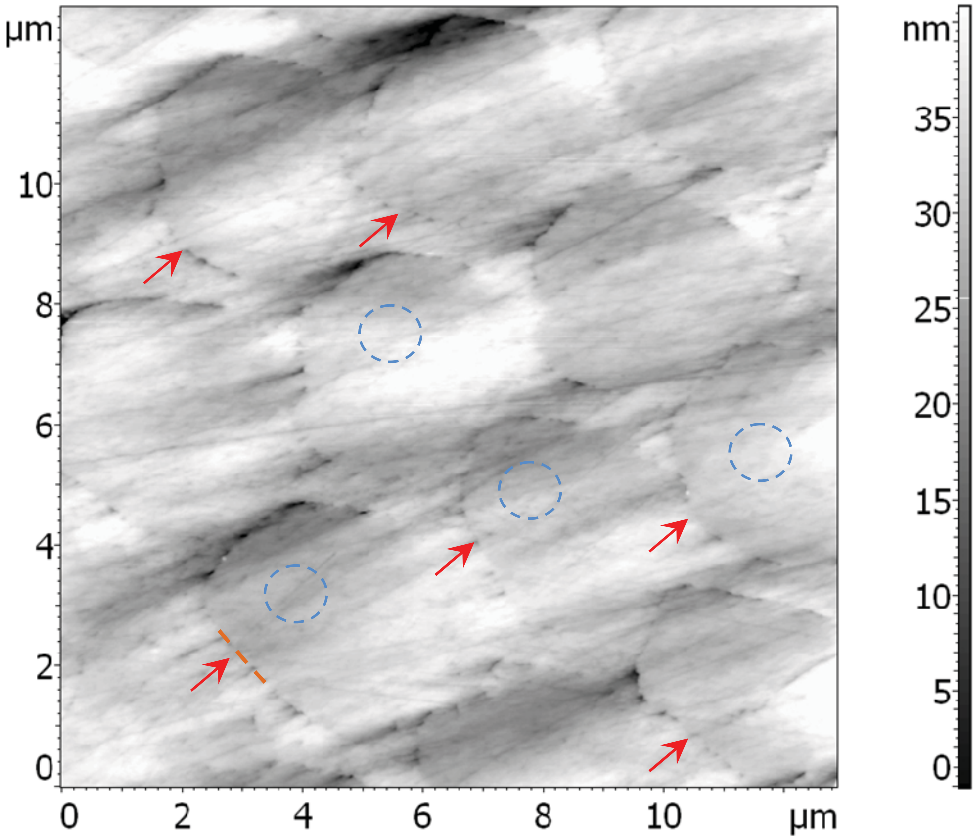

Figure 2.13 Indication of criteria that were applied for selecting AFAM single point measurement locations. The red arrows point for the locations that may be chosen for sheath modulus measurements with a clear profile (orange dash line) and least possible depth variation from prisms. The blue circles map the possible AFAM point measurement locations, in flatter center region of prism.

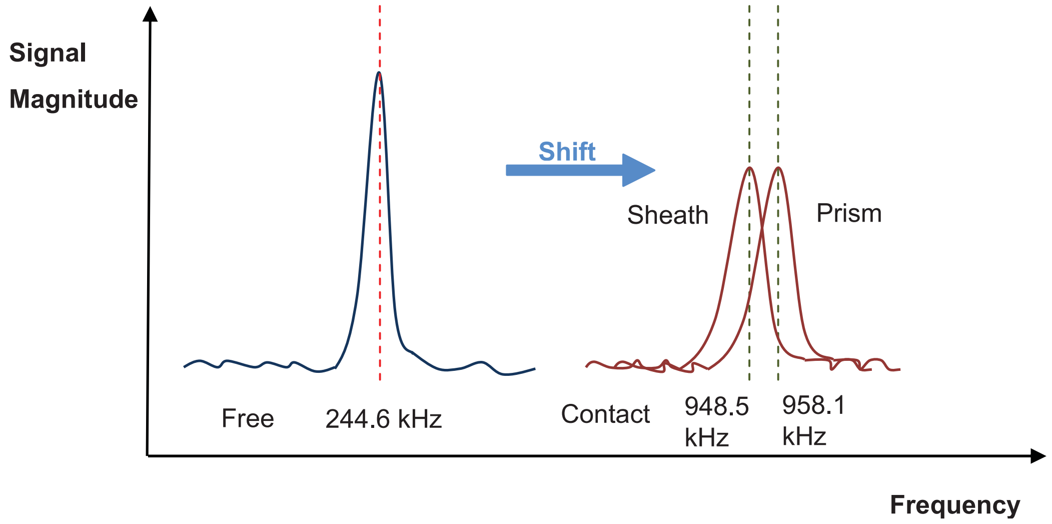

Figure 2.14 Resonance Frequency shift correspondent to boundary condition change from free cantilever vibration to contact resonance frequency. Further shift in frequency occurs when probe is in contact with sheath versus prism enamel (indicated on right). Note the axes are not to scale and are for comparison purposes.

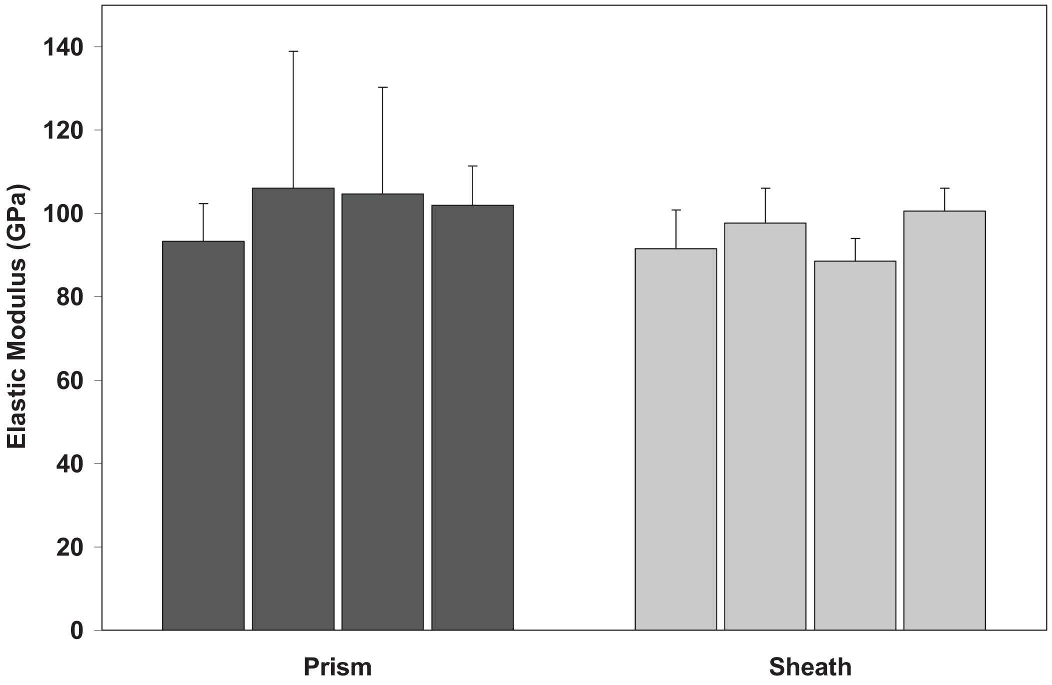

Figure 2.15 Elastic modulus calculated from AFAM measurements on enamel prism and sheath regions of surface on bicuspids. Each column represents a separate measuring position.

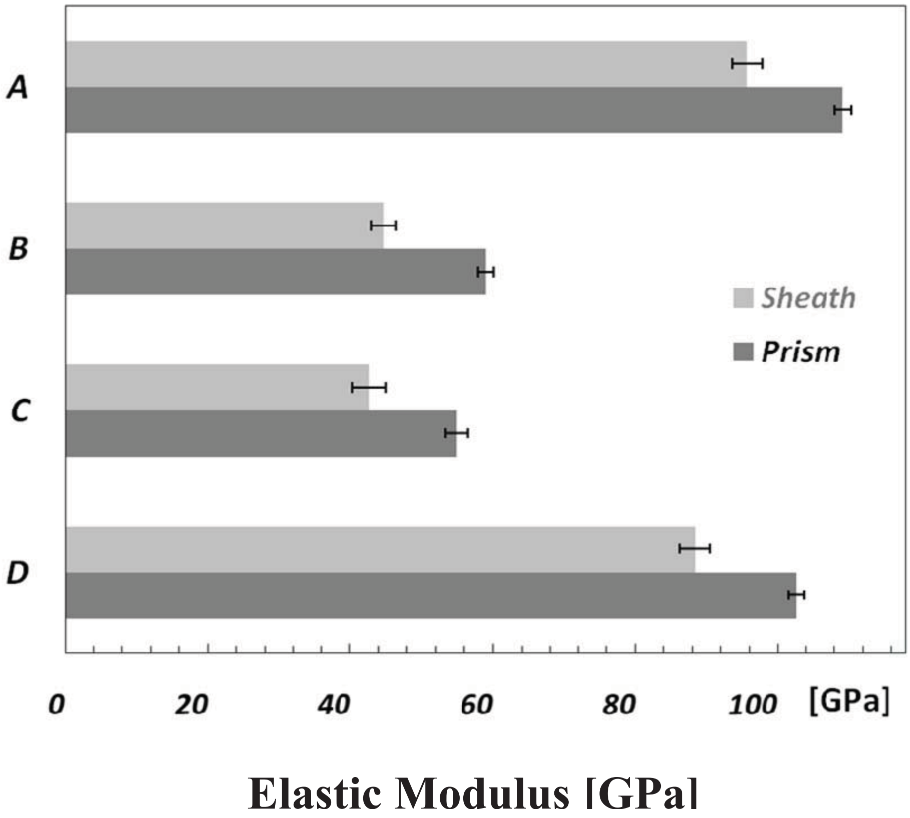

Figure 2.16 Eastic modulus results from contact stiffness showed in a), by Hertzian contact analysis.

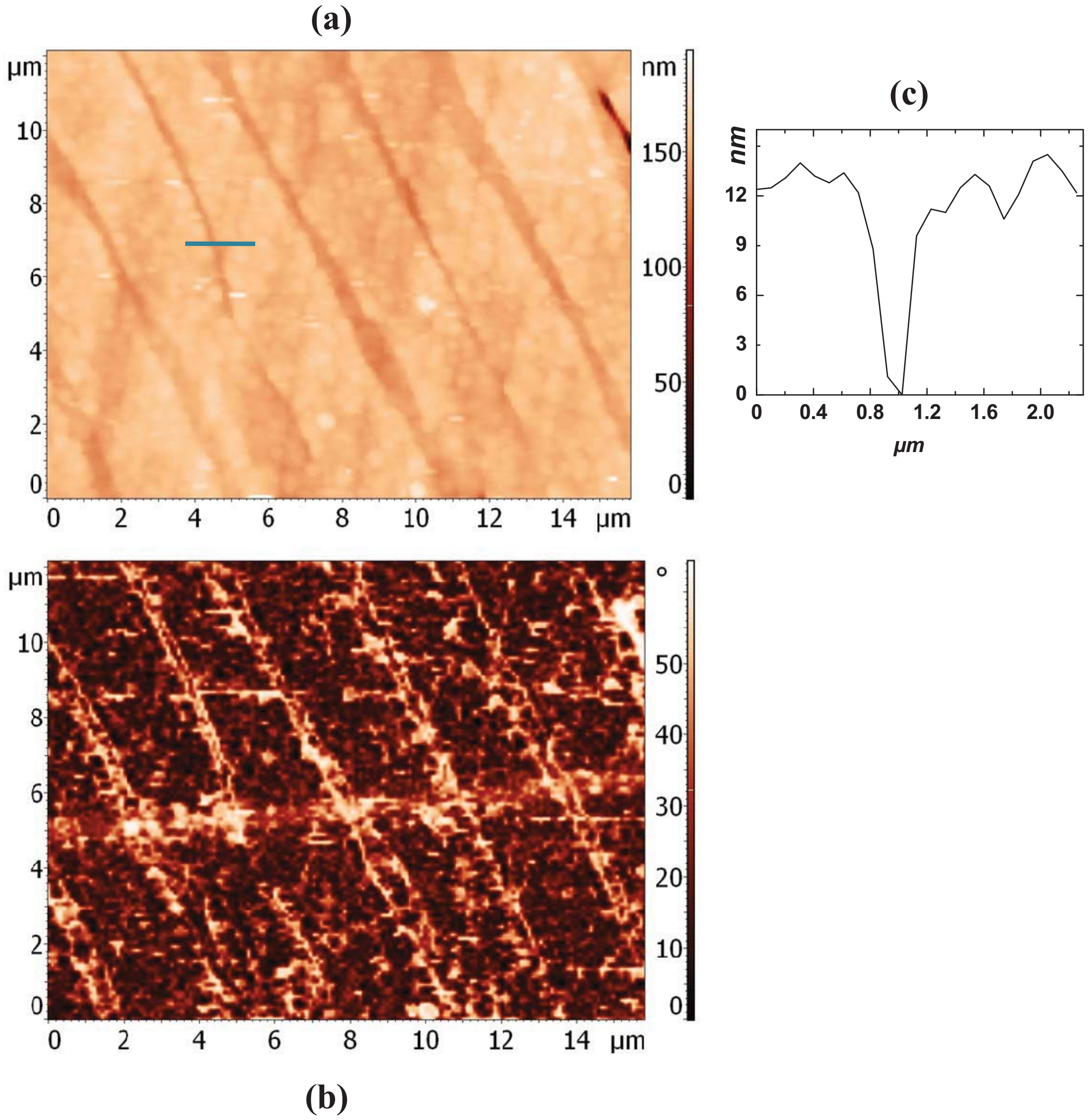

Figure 2.17 AFAM surface profile and phase image, stored in deionized water for 10 hours after polishing.

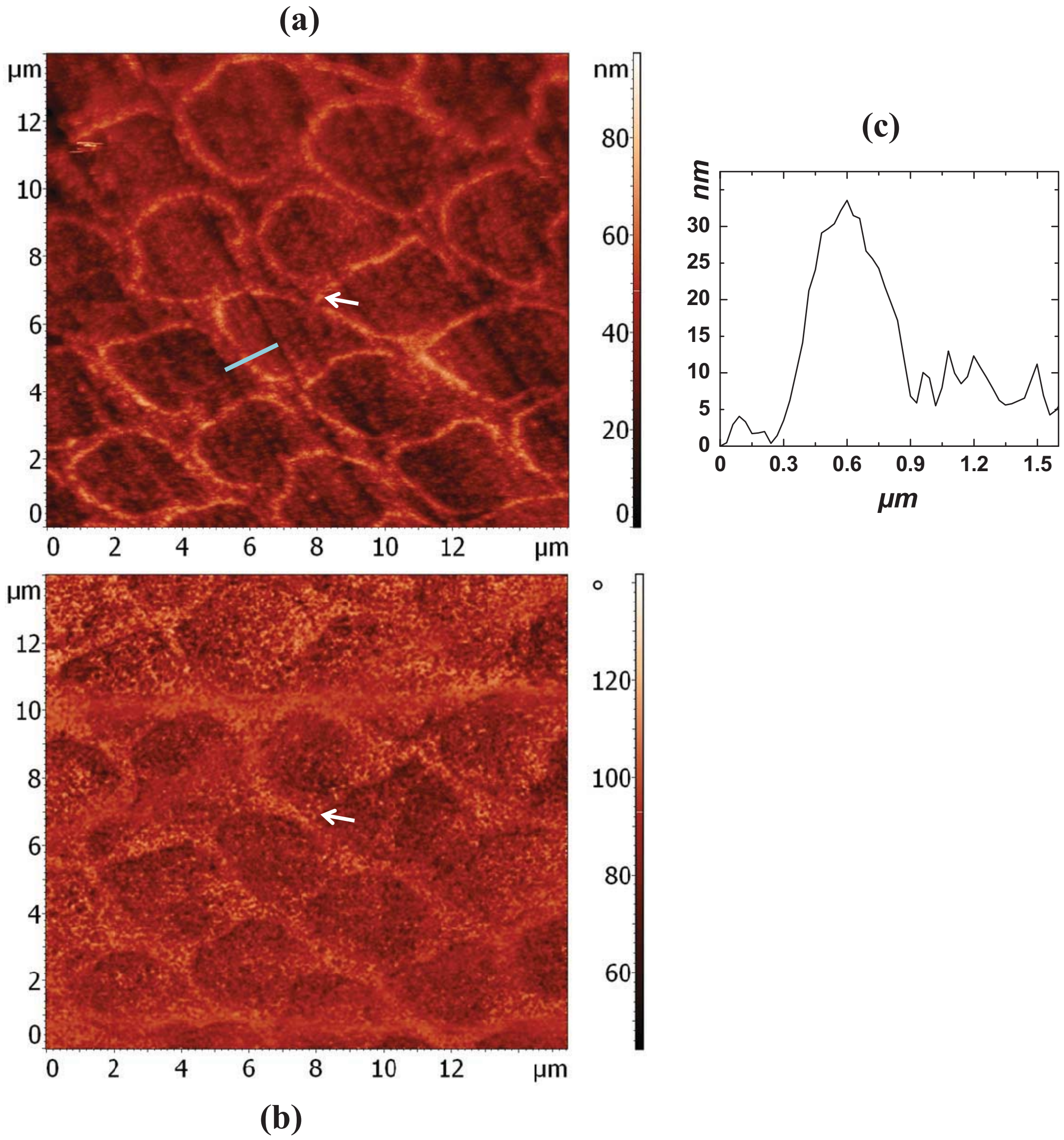

Figure 2.18 AFAM surface profile and phase image, after dropped in 0.1 mol lactic acid solution for 4 seconds with deionized water resin afterwards.

Table 2.1 Contact stiffness (k^*) and elastic modulus (E_s) of prism and sheath regions on the bicuspids enamel surface.

Prism	Measuring Locations								Average	
	Location 1		Location 2		Location 3		Location 4		Es	
Load	k^*	E_s	k^*	E_s	k^*	E_s	k^*	E_s	Ave	s.d.
2.88	1419.5	103.6	1139.0	68.8	1278.6	85.3	1353.8	95.1	88.2	14.9
3.38	1357.1	86.4	1595.7	118.7	1428.6	95.3	1450.9	98.2	99.7	13.7
3.87	1450.9	89.9	1749.4	130.7	1768.6	133.4	1628.1	112.7	116.7	20.1
Ave	1409.0	93.2	1494.7	106.8	1492.0	104.8	1477.6	102.0	101.7	6.0
μN	***N/m***	***GPa***	***N/m***	***GPa***	***N/m***	***GPa***	***N/m***	***GPa***	***GPa***	***GPa***
Ave	1397.5	91.5	1445.8	97.7	1373.4	88.5	1467.2	100.6	94.6	5.6
3.87	1540.9	101.1	1582.2	106.5	1470.1	92.2	1582.2	106.5	101.6	6.7
3.38	1396.4	91.2	1441.6	97.0	1396.4	91.2	1462.3	99.7	94.8	4.3
2.88	1255.3	82.4	1313.6	89.7	1253.9	82.2	1357.1	95.6	87.5	6.4
Load	k^*	E_s	k^*	E_s	k^*	E_s	k^*	E_s	Ave	s.d.
Sheath	Location 1		Location 2		Location 3		Location 4		Es	
	Measuring Locations								Average	

Table 2.2 Tooth molar enamel surface AFAM elastic modulus results based on 10 different locations measurements for each of prism and sheath, under 2.68 μN applied load.

Measurements		**1**	**2**	**3**	**4**	**5**	**6**	**7**	**8**	**9**	**10**	**Average**	**Stv**
Prism	**Contact Stiffness**	1494.67	1499.40	1500.98	1505.74	1500.98	1485.26	1502.57	1505.74	1504.15	1507.33	**1500.68**	**6.56**
	Elastic Modulus	108.06	108.90	109.18	110.03	109.18	106.41	109.46	110.03	109.75	110.32	**109.13**	**1.16**
Sheath	**Elastic Modulus**	92.45	96.12	97.79	96.12	93.12	93.57	97.79	94.72	97.31	98.03	**95.70**	**2.10**
	Contact Stiffness	1428.68	1452.85	1463.56	1452.85	1433.18	1436.19	1463.56	1443.73	1460.49	1465.10	**1450.02**	**13.7**

Table 2.3 Tooth molar enamel AFAM contact stiffness results based on 10 different locations measurements on all measured surfaces for each of prism and sheath, under ~2.5 μN applied load.

	A		**B**		**C**		**D**	
No.	**Prism**	**Sheath**	**Prism**	**Sheath**	**Prism**	**Sheath**	**Prism**	**Sheath**
1	1494.67	1428.68	1047.80	1042.10	949.33	933.34	1496.25	1394.70
2	1499.40	1452.85	1045.52	1038.69	987.30	928.04	1477.47	1399.09
3	1500.98	1463.56	1065.04	1076.65	967.66	926.98	1485.26	1433.18
4	1505.74	1452.85	1042.10	1008.32	953.62	887.34	1491.53	1430.18
5	1500.98	1433.18	1052.38	1056.97	946.12	925.93	1494.67	1399.09
6	1485.26	1436.19	1073.16	1029.62	972.00	879.12	1488.39	1422.71
7	1502.57	1463.56	1050.09	1020.62	962.24	883.22	1475.92	1413.80
8	1505.74	1443.73	1058.12	1015.01	966.57	871.96	1493.10	1399.09
9	1504.15	1460.49	1053.53	1047.80	986.21	883.22	1488.39	1406.42
10	1507.33	1465.10	1047.80	1047.80	965.49	866.87	1488.39	1391.79
Ave	**1500.68**	**1450.02**	**1053.55**	**1038.36**	**965.65**	**898.60**	**1487.94**	**1409.00**
Stv	**6.56**	**13.70**	**9.50**	**20.67**	**13.91**	**26.50**	**6.80**	**15.08**

2.4 References

[2.1]. AR, TENCATE. Oral Histology: Development, Structure, and Function. 4th ed: Mosby; 1994.

[2.2]. AEW, MILES. Structural and Chemical Organization of Teeth, Vol. II: Academic Press 1967.

[2.3]. XU HHK, SMITH DT, JAHANMIR S, ROMBERG E, KELLY JR, THOMPSON VP, REKOW ED. Indentation damage and mechanical properties of human enamel and dentin. J of Dental Res. 1998;77:472-480.

[2.4]. PARK S, WANG DH, ZHANG D, ROMBERG E, AROLA D. Mechanical properties of human enamel as a function of age and location in the tooth. J of Matls Sci: Matls in Med. 2008(19):2317-2324.

[2.5]. MECKEL AH, GRIEBSTEIN WJ, NEAL RJ. Structure of mature human dental enamel as observed by electron microscopy. Arch Oral Biol. 1965;10:775-784.

[2.6]. MECKEL AH, GRIEBSTEIN WJ, NEAL RJ. Ultrastructure of fully calcified human dental enamel. In Tooth enamel, its composition, properties and fundamental structure (eds. Stack MV, Fearnhead RW): John Wright; 1962.

[2.7]. WILLEMS G, CELIS JP, LAMBRECHTS P, BRAEM M, VANHERLE G. Hardness and Young's modulus determined by nanoindentation technique of filler particles of dental restorative materials compared with human enamel. J Biomed Matls Res. 1993(27):747-755.

[2.8]. HABELITZ S, MARSHALL SJ, MARSHALL GW, BALOOCH M. Mechanical properties of human dental enamel on the nanometer scale. Arch Oral Biol. 2001;46:173-183.

[2.9]. CUY JL, MANN AB, LIVI KJ, TEAFORD MF, WEIHS TP. Nanoindentation mapping of the mechanical properties of human molar tooth enamel. Arch Oral Biol. 2002;47:281-291.

[2.10]. GE J, CUI FZ, WANG XM, FENG HL. Property variations in the prism and organic sheath within enamel by nanoindentation. Biomaterials. 2005;26:3333-3339.

[2.11]. BAJAJ D, AROLA DD. On the R-curve behavior of human tooth enamel. Biomaterials. 2009;30:4037-4046.

[2.12]. L. LARGEAU, G.PATRIARCHE, A. RIVIERE, J.P.RIVIERE, E.LE BOURHIS. Indentation punching through thin (011) InP. Journal of Materials Science. 2004(39):943-949.

[2.13]. LIPPERT F, PARKER DM, JANDT KD. In vitro demineralization/remineralization cycles at human tooth enamel surfaces investigated by AFM and nanoindentation. J

Colloid Interf Sci. 2004;280(442-448).

[2.14]. BALOOCH G, MARSHALL GW, MARSHALL SJ, WARREN OL, ASIF SA, BALOOCH M. Evaluation of a new modulus mapping technique to investigate microstructural features of human teeth. J Biomech. 2004;37:1223-1232.

[2.15]. HABELITZ S, MARSHALL SJ, MARSHALL GW, BALOOCH M. The functional width of the dentino-enamel junction determined by AFM-based nanoscratching. J of Struct Biol. 2001;135:294-301.

[2.16]. A. GRUVERMAN, D. WU, B.J. RODRIGUEZ, S.V. KALININ, S. HABELITZ. High-resolution imaging of proteins in human teeth by scanning probe microscopy. Biochemical and Biophysical Research Communications. 2007;352:142-146.

[2.17]. RODRIGUEZ BJ, KALININ SV, SHIN J, JESSE S, GRICHKO V, THUNDAT T, BADDORF AP, GRUVERMAN A. Electromechanical imaging of biomaterials by scanning probe microscopy. J Struct Biol. 2006;153:151-159.

[2.18]. NGWA W, LUO W, KAMANYI A, FOMBA KW, GRILL W. Characterization of polymer thin films by phase-sensitive acoustic microscopy and atomic force microscopy: a comparative review. Journal of Microscopy-Oxford. 2005;218:208-218.

[2.19]. KESTER E, RABE U, PRESMANES L, TAILHADES P, ARNOLD W. Measurement of mechanical properties of nanoscaled ferrites using atomic force microscopy at ultrasonic frequencies. Nanostructured Materials. 1999;12:779-782.

[2.20]. HURLEY DC, GEISS RH, KOPYCINSKA-MULLER M, MULLER J, READ DT, WRIGHT JE, JENNETT NM, MAXWELL AS. Anisotropic elastic properties of nanocrystalline nickel thin films. Journal of Materials Research. 2005;20:1186-1193.

[2.21]. RABE U, AMELIO S, KESTER E, SCHERER V, HIRSEKORN S, ARNOLD W. Quantitative determination of contact stiffness using atomic force acoustic microscopy. Ultrasonics. 2000;38:430-437.

[2.22]. RABE U, JANSER K, ARNOLD W. Vibrations of free and surface-coupled atomic force microscope cantilevers: Theory and experiment. REVIEW OF SCIENTIFIC INSTRUMENTS. 1996;67:3281-3293.

[2.23]. WRIGHT OB, NISHIGUCHI N. Vibrational dynamics of force microscopy: Effect of tip dimensions. Applied Physics Letters. 1997;71:626-628.

[2.24]. YAMANAKA K, NAKANO S. Quantitative elasticity evaluation by contact resonance in an atomic force microscope. Applied Physics Materials a- Science & Processing. 1998;66:313-317.

[2.25]. HIRSEKORN S, RABE U, ARNOLD W. Theoretical description of the transfer of vibrations from a sample to the cantilever of an atomic force microscope. Nanotechnology. 1997;8(2):57-66.

[2.26]. RABE U, KOPYCINSKA M, HIRSEKORN S, SALDANA JM, SCHNEIDER GA, ARNOLD W. High-resolution characterization of piezoelectric ceramics by ultrasonic scanning force microscopy techniques. Journal of Physics D-Applied Physics. 2002;35(20):2621-2635.

[2.27]. KL, JOHNSON. Contact Mechanics: Cambridge University Press; 1985.

[2.28]. MALGORZATA KOPYCINSKA-MULLER, ROY H GEISS, DONNA C. HURLEY. Contact Mechanics and Tip Shape in AFM-based Nanomechanical Measurements. Ultramicroscopy. 2006(106):466-474.

[2.29]. D. C. HURLEY, K. SHEN, N. M. JENNETT, J. A. TURNER. Atomic force acoustic microscopy methods to determine thin-film elastic properties. JOURNAL OF APPLIED PHYSICS. 2003;94(4):2347-2354.

[2.30]. GHEORGHE STAN, WILLIAM PRICE. Quantitative measurements of indentation moduli by atomic force acoustic microscopy using a dual reference method. REVIEW OF SCIENTIFIC INSTRUMENTS. 2006;77(103707):1-6.

[2.31]. LIBOR BRABEC, PETR BOHAC, MARTIN STRANYANEK, RADIM CTVRTLIK, MILAN KOCIRIK. Hardness and elastic modulus of silicalite-1 crystal twins. Microporous and Mesoporous Materials. 2006;94:226-233.

[2.32]. HUTTER JL, BECHHOEFER J. Calibration of atomic-force microscope tips.

REVIEW OF SCIENTIFIC INSTRUMENTS. 1993;64:1868-1873.

[2.33]. ZHAO W, SINGH RP, KORACH CS. Effects of environmental degradation on near-fiber nanomechanical properties of carbon fiber epoxy composites. Composites: Part A 2009;40:675-678.

[2.34]. IR, SPEARS. A three-dimensional finite-element model of prismatic enamel: a re-appraisal of the data on the Young's modulus of enamel. J Dent Res. 1997;76:1690-1697.

[2.35]. SHIMIZU D, MACHO GA, SPEARS IR. Effect of prism orientation and loading direction on contact stresses in prismatic enamel of primates: implications for interpreting wear patterns. Am J Phys Anthop. 2005;126:427-434.

[2.36]. MIURA J, MAEDA Y, NAKAI H, ZAKO M. Multiscale analysis of stress distribution in teeth under applied forces. Dent Matls. 2009;25:67-73.

Chapter Three

Effects of Environmental Degradation on Nanomechanical Properties of Epoxy

The fiber and matrix interphase is believed to control the fundamental load-transfer process and thereby bulk mechanical properties of composites. Carbon fiber reinforced composite properties have been qualitatively shown to be affected by moisture based degradation; however, quantitative characterization of the nanomechanical properties as a function of exposure time is still unknown. Here, quantitative elastic properties measurement has been performed on the epoxy matrix and fiber-matrix interphase taking advantage of the high scanning resolution of atomic force acoustic microscopy (AFAM). Composites were exposed to accelerated degradation and characterized using AFAM, showing elastic modulus variations in the matrix and interphase as a function of exposure. Chemical analysis was also performed by Raman and Fourier Transform Infrared (FTIR) spectroscopy to investigate the mechanisms of epoxy degradation after water immersion.

3.1. Introduction

Fiber reinforced polymer composites have gradually gained popularity by superior mechanical properties over most ubiquitous engineering materials in engineering infrastructure applications. However, before such advanced materials can be widely utilized in long-term engineering applications, it is critical to investigate the mechanical characteristics in terms of long-term durability when used in demanding environments, especially moisture and elevated temperature exposure. Moisture is readily absorbed by most polymer matrices and leads to changes in mechanical characteristics [3.1-3]. Moisture diffusion can be exacerbated by application of elevated temperatures. The region between fiber and matrix in composites, commonly referred to as the matrix interphase, is key to governing bulk mechanical response of a composite [3.4]. Understanding the effects of environmental exposure on the matrix interphase is critical to determine the micromechanical changes on the bulk composite strength. Research on moisture based degradation has been qualitatively shown to affect the properties of the interphase [3.5-6]. Typically, when the polymer composite is exposed to moisture, the uptake of water will occur as a diffusion-controlled process [3.7]. Absorbed water tends to act as a plasticizer, and swells the polymer through stretching resin matrix entanglements. Hydrogen bonds of water within the resin matrix may also break and bound to polymer hydroxyl groups [3.8]. It has been widely found that interactions of water with the resin matrix could result in a decreased modulus in polymer materials [3.9-10]. In addition, the interface bond between matrix and fiber is found to weaken and sometimes break after water uptake; such failure could significantly reduce the composite's load capability [3.6, 11].

The interphase region, which is on the order of hundreds of nanometers, exits between a fiber and matrix in composites, and controls the fundamental load-transfer (Fig 3.1). Hence, quantitative measurement of the mechanical properties at or near the fiber-matrix interphase is of critical importance. Measurement of the interphase region properties, which is on the scale of tens to hundreds of nanometers, requires a technique capable of providing high spatial resolution. Atomic Force Microscopy (AFM) provides spatial resolution necessary for interphase measurements, though AFM techniques can only provide topographic imaging and qualitative determination of surface stiffness by phase imaging or force modulation techniques [3.12-14]. The nanoscratch friction test could be achieved at nano scale to determine surface coefficient of friction using a Nano indentation instrument, which lacks the ability to provide quantitative elastic modulus results [3.15]. AFM phase imaging is shown to be able to detect qualitative modulus changes over the surface on a submicron resolution [3.12]. Even though AFM based indentation measurement could provide quantitative elastic results, the large radius curvature tips are not sufficient small to provide desired resolution for composite interphase measurement [3.16].

Atomic Force Acoustic Microscopy (AFAM) is a recently developed tool that retains the same excellent lateral resolution of AFM scanning probe microscopes, but is combined with an the ultrasonic excitation to achieve quantitative mechanical property measurements [3.1-3, 17-18]. The ability to measure mechanical characteristics on the order of nanometer resolution can be applied to measuring mechanical property variations in the sub-micrometer thick interphase region. AFAM has not been utilized for interphase characterization (nor characterization of the interphase as a function of degradation), but has been used to study layered and thin film polymers [3.19-20], patterned wafers [3.21], thin-film magnetic ferrite grains [3.22], and nanocrystalline Ni [3.23]. These examples have been able to measure features on the order of tens of nanometers resolution, and hence can be applied to measuring mechanical property variations of epoxy between fiber reinforcements. In this study, AFAM is used to characterize the epoxy interphase as a function of degradation time. This is achieved in part due to tip radius of curvature on the order of 10 nm and the ability of the piezo-stack scanner to achieve sub-nanometer lateral resolution.

In this chapter, AFAM testing on the near fiber epoxy matrix regions has been performed, which will establish the quantitative characterization methodology used in interphase measurements. The epoxy samples had been tested with similar degradation environmental conditions in order to guide accurate measurement of the interphase region. The laboratory created sea water (5% by mass of sodium chloride dissolved in deionized water [3.24]), as another degradation environment, was compared with deionized water. The measured mechanical response from the accelerated degradation samples are compared with to long-term exposure conditions based on published correlations [3.25].

3.2. Accelerated Degradation

To study composite degradation by moisture, the time necessary is prohibitive to test the samples in real environments and determine durability. Accelerated environmental degradation chambers and moisture immersion techniques have been employed to decrease the amount of exposure time [3.25-26]. To simulate long-term degradation effects and reduce degradation periods in laboratory tests, Holliday (1966) proposed a boiling water degradation technique, which suggests that 2 hours boiling relates to 3 months room temperature water immersion [3.25]. As shown in Figure 3.2, boiling water degradation of composite samples took place in a deionized water filled boiling flask. A silicone oil bath was used to provide indirect heat input and to generate an average heat distribution for the deionized water. Cold water was continuously running through a condenser to retain evaporate. During degradation, the temperature of the silicone oil was controlled within the range of 130 to 135 °C. Samples for testing were placed into the degradation system all together, and each of two pieces were taken out after desired intervals, while letting the remaining degrade until all of them were removed. According to our study, the composite materials exposed to deionized water immersion in the accelerated boiling degradation system for 48 and 72 hours have a significant decrease in mechanical performance compared to undegraded samples (see figure 3.3). The majority of the mechanical performance decrease in composite materials is due to the epoxy matrix [3.27].

In our study, the epoxy matrix had been degraded under conditions with DI water, for 0, 24, 48, 72, 96 and 120 hours, before testing with the AFAM. AFAM comparison between lab made salt water and deionized water was performed with 48 hours degradation only, in conjunction with corresponding chemical reaction measurements. To avoid probe wear, the AFAM interphase measurements were only performed for accelerated DI water degradation with 48 and 144 hours exposure. These results are used to determine the mechanical property variation as a function of degradation time.

3.3. Epoxy Matrix Degradation Study

3.3.1. Composite Specimens

In this study, coupons of carbon fiber reinforced epoxy specimens are prepared from in-house materials fabricated using a vacuum bagging procedure using IM7 carbon fiber reinforced with Epon862 epoxy. (Samples were provided by Prof. Raman Singh at Oklahoma State University) The fiber-matrix interphase properties can be modified by the use of different silane coupling agents, such as the Z-6040 epoxy silane and the Z-6032 vinylbenzylamino silane from Dow Corning. It is known that the use of silanes improves the hot-wet performance of composites, but the mechanisms have not yet been established. In this work, the surface conditions and sizing of the fibers was unknown. Figure 3.1 provides the overall microstructure of a fiber-reinforced composite.

Specimens were machined from vacuum bag fabricated $[0]_8$ laminates of IM7/Epon862 carbon-fiber/epoxy composite. IM7 is a 5 μm diameter, Polyacrylonitrile (PAN) based carbon fiber, while Epon862 is a low viscosity epoxy resin manufactured from epichlorohydrin and Bisphenol-F with superior mechanical, adhesive, electrical and chemical resistance properties if cross-linked with appropriate curing agents. All specimens were preconditioned in a desiccator at ambient temperature and 10% relative humidity for one to two weeks, and a diamond saw was used to cut samples in order to mount them onto the AFAM stage for testing. Due to the low roughness requirement to obtain results with AFAM, samples underwent metallographic polishing steps with 3 m, 1 m, and 0.05 m particles. Degraded specimens were tested by AFAM immediately after removal from the accelerated degradation system.

3.3.2. Quantitative Mechanical Measurements

AFAM measurements were performed in the epoxy matrix region near the fibers for the undegraded and degraded composites (Figure 3.4). The measurement is performed on AFAM by NSG11 semi-contact long tip with radius curvature of 35nm. For each exposure case two samples were used and five independent locations were measured and the data averaged. Locations were sought out that avoided fiber-debonding which was observed for degraded samples. Phase changes in the cantilever resonance frequency while in contact with the ultrasonically perturbed composite specimen were recorded. Specimen perturbation ranged between frequencies of 1100 – 2300 kHz. Frequency results are used in Eqns. (2.1) – (2.3) to determine the contact stiffness, *k**, which is used in Eqns. (2.6) and (2.7) to determine the sample modulus. Measurements were made for samples exposed to the boiling water degradation at intervals of 1 day. The samples were allowed to sit at room temperature for 2 hours prior to measurement, thus any moisture on the surface in contact with the probe would have evaporated at the scale of the experiment. Quantitative decrease in the epoxy matrix stiffness near the carbon fibers was found as a function of degradation exposure. As seen in figure 3.5, stiffness values leveled off at ~72 hours exposure. The observed decrease in stiffness is believed to be a contribution of moisture absorption into the polymer matrix as well as degradation of the polymer cross-links due to the temperature and humidity exposure. In addition, the sensitivity of the results was evaluated as a function of the applied tip load (F_c). Figure 3.6 shows a consistent value of E_s versus the applied normal load for undegraded and degraded samples indicating the stability of the reported measurements. These results are expected over a certain range, as long as the load is sufficient for coherent contact, since the contact force is proportional to the load bearing contact area. It can be concluded that the majority of the degradation is ocurring during the first 3 days, and that epoxy is less affected after 3 days degradation. After 5 days in boiling DI water, the Young's modulus of epoxy dramatically reduced to 10% of the undegraded value.

Spatial imaging of the matrix stiffness as a function of distance from a fiber can be obtained utilizing AFAM due to the high spatial resolution of the technique. A measurement of the contact resonance frequencies of a degraded specimen (see figure 3.7) between the fiber and matrix demonstrates the increase in frequency phase angle in the matrix approaching the fiber-matrix interface. The AFAM phase signal is related to the change in stiffness of the matrix, thus the region close to the fiber-matrix interface is stiffer than the matrix further from the fiber-matrix interface. This is believed to be affected by a surface sizing that is present on the carbon fibers from the manufacturer to prevent fiber damage durin g handling in filament winding, prepregging and weaving operations [3.28]. Based on the AFAM phase mapping, the interphase spatial span was measured at three different directions from the fiber (see figure 3.7). From the spatial measurement results, the interphase is estimated to be ~200 – 300 nm in width, which corresponds to measurements by others using AFM phase imaging [3.12]. The contact stiffness of the interphase region is found to be consistent from measurements in different directions. However, the phase angle changes in AFAM phase mapping may not be a very precise method in interphase spatial length determination for two reasons. One is that the radius of curvature variation during scanning makes the probe geometry inconsistent for quantitative measurements, especially at high resolution scanning where a significant number of contacts occurs. Second, and most importantly, is that the large difference between the fiber and matrix elastic modulus can result in difficulties in indentify the edge of the matrix and interphase, particularly at low resolution. These restrictions lead the interphase spatial length to be better measured from AFAM single point testing, where a limited number of contacts will be performed by precisely controlled measurement steps. The results of the measurements will be discussed in the following sections.

In summary, AFAM has been shown to observe quantitative stiffness variations in the epoxy matrix between carbon fibers for degraded carbon fiber reinforced epoxy composites. The elastic modulus of the degraded epoxy decreased from 4.8 GPa until reaching a constant after 72 hours of hyper-accelerated degradation. Spatial measurements showed an interphase region with thickness of 200 to 300 nm. The contact stiffness is sensitive to the cantilever selection and a cantilever stiffness of 6.04 N/m was used for epoxy matrix measurements. Finally, the elastic modulus remained constant over varying applied loads. The results demonstrate that localized degradation of the epoxy matrix can be quantified using AFAM, and has direct implications on long-term performance of polymer matrix reinforced composites exposed to environmental conditions.

3.3.3. Salt Water Environmental Degradation Comparison

The study of the composite degradation in salt water condition is essential, as the composite materials are often desired to serve in sea water environments. Although it has been shown chemically that sodium chloride is unlikely to react with the components of the composite materials, it is still of interest to compare effects of salt water environments to deionized water degradation.

The AFAM measurement had been performed on the pure epoxy that had been cured without fibers by the exact same protocols described in Section 2.2. The samples had undergone for 3 days accelerated degradation, under deionized water and lab made sea water, respectively. The AFAM measurement was conducted on deionzied and sea water degraded and undegraded samples consequently, by fpN11S probe with spring constant of 6.5 N/m. To note, it is intended to choose a high-radius spherical AFM probe in order to acquire accurate quantitative measurement with minimum effects from the probe contact condition. Twelve measurements were conducted on each specimen, and only ten of them are selected to present without the largest and smallest values from the sets. The elastic modulus was calculated right after the contact stiffness derived from the contact resonance frequency, by following the determination equation listed in section 2.2. AFAM quantitative results are achieved applying the techniques that had been utilized in the former part of this chapter and shown in Figure 3.8. The obtained elastic modulus of the salt water and deionized water degraded materials had been shown to be greatly degraded after 3 days exposure, as compared to the undegraded specimens. It has been consistently found that the elastic modulus of the specimens degraded in salt water is less affected than those in the deionized water. This mechanism requires the corresponding chemical measurements and understanding of the degradation behind the mechanical response differences.

3.3.4. Chemical Analysis

Raman spectroscopy (named after C. V. Raman) is a spectroscopic technique used to study vibrational, rotational, and other low-frequency modes in desired sample materials[3.29]. It relies on inelastic or Raman scattering, of monochromatic light, from a laser in the visible, near infrared or ultraviolet range. The laser light interacts with phonons in the system, resulting in the energy of the laser photons being shifted up or down. The shift in energy gives information about the phonon modes in the system, and thus could help to identify the bonding conditions in the measured materials.

The Fourier transform infrared spectroscopy(FTIR) is a molecular vibration absorption spectroscopy, which can be used to identify compounds or investigate sample composition. Due to the sensitivity difference of the coupling between the photons and the vibrational transitions in Raman and FTIR, materials will not often exhibit all of the features on both the FTIR absorption and Raman scattering spectrums. Thus, in this study, both the Raman and FTIR have been employed to analyze the composite specimens degraded by the salt water and deionized water to acquire a wider range of features.

Epoxy is often based on diglycidyl ether of bisphenol A, which contains ether groups. Esters and ethers are susceptible to attack from polymer hydrolysis, wherein backbone polymer chains are “cut” by bonding with water[3.30-31]. Polymer hydrolysis involves the scission of susceptible molecular groups by reaction with H_2O. This may be caused by acid, base or enzyme catalysts. This is not a surface-limited reaction if water penetrates into the sample bulk. Succeptible linkages at bonds where resonance stabilized intermediates are possible, may result in potential reactions indicated in Figure 3.9. Both Raman and FTIR spectroscopy have been used successfully to achieve a chemical understanding of the reactions in coatings[3.32-34] polymers[3.35-36] and EPON862 epoxy [3.37].

After the degradation was carried out, the epoxy was characterized using both Raman and FTIR spectroscopy. Figure 3.10 shows the FTIR spectra for the EPON 862 epoxy samples that had undergone salt and deionized water degradation in comparison with undegraded samples. Peaks at 950, 856 and 762 cm^{-1} coinciding with epoxide bonding [3.38-41] are significantly recorded for the degraded samples, indicating epoxide hydrolysis has occurred. Eventhough at these three wavenumbers no significant difference was observed between the two degradation environments, the deionzed water degraded samples did show some additional peak changes, indicating more damage than the salt water degraded samples. This observance matches what we had found from AFAM quantitative mechanical testing. At the wavenumbers of 1127, 1057 cm^{-1} [3.42-43], spectrum from the deionized water degraded samples indicated a greater degree of C-O-C scissioning than in the case of salt water degraded samples. However, in these peaks, none of the degraded samples exhibit large amounts of degradation compared to the epoxide group. The chemical reactions associated with both of the two groups of wavenumbers are summarized in Figure 3.9.

Similar conclusions were approached from the Raman measurements confirming the FTIR results. Decrease of peaks at 750~900 cm^{-1} with epoxide [3.44-45] and 1045 cm^{-1} with C-O-C bonding for degraded samples, is a sign of hydrolysis (see figure 3.11), while samples exposed to deionized water is shown to be less affected than the case of salt water. However, Raman spectrum contain more information on fluorescence associated with the degree of damage [3.46]. Reactions during epoxy-resin curing produce inter-molecular cross-linking and intra-molecular ring formation. A broad range of wavelengths (from ultraviolet to near infrared optical wavelength) will be evident in the fluorescence from the samples and in the optical absorbance by the sample signifying the complex macro-molecular structures produced. However, if the material is degraded over certain limits and by undergoing some form of chemical reactions, e.g. hydrolysis, oxidation and dehydration, the fluorescence spectrum of degraded material will present a superposition of fluorescence that is different from the one which exists in initial undegraded condition, besides other features [3.46-48]. These changes in the polymer composites are often regarded to be due to a degree of irreversible degradation, which will be observed in the fluorescence by variations of both the total emission and the wavelength of maximum intensities. Throughout our experiments, the intensity increase is observed for samples degraded in both salt and deionized water, where the later condition undergoes more gains of intensity in background fluorescence. This unique feature represents that hydrothermal damage occurred during the accelerated degradation, and correspondingly can be related to chemical reactions during the degradation. The fluorescence increase, in fundamental, can be another explanation for the correspondent mechanical decrease, besides the peak decrease for C-O-C and Epoxide bonds.

In summary, consistent peak changes for both salt and boiling water immersion were observed from Raman and FTIR measurements. It also has been shown that there was less severe peak changes in salt than deionized water immersed samples, thus, the existence of salt in the solution prevents/slows epoxy degradation mechanisms.

3.4. Fiber-matrix Interphase Degradation Determination

In this section, carbon fiber reinforced composite samples are exposed to deionized boiling water under similar accelerated moisture environmental degradation as in section 2 of this chapter. AFAM is used to measure the matrix interphase region surrounding the fibers. Changes in contact stiffness for the dimensions of the interphase as a function of exposure time observed the effects of environmental degradation on the fiber-matrix interphase region.

3.4.1. Sample Preparation

In this study, carbon fiber reinforced epoxy samples are machined from in-house materials fabricated using a vacuum bagging procedure from IM7 carbon-fiber. The epoxy matrix consists of EPON 862 resin cured using Epikure 3234 Hardener, with the 100:11.5 resin to hardener ratio by weight. Specimens are cut using a water-cooled, high-speed diamond saw into 8 x 2 x 2 mm samples for AFAM characterization. When utilizing scanning probe techniques, a low surface roughness will result in better imaging. Polishing of specimen testing surfaces by a standard metallographic polisher (EcoMet® 3000 grinder-polisher, Buehler) was performed in 3 steps with slurries of 3, 1, and 0.05 ìm sizes.

Ultrasonic cleaning is performed on samples after polishing to remove adhered particles on the sample surfaces. Due to the large stiffness difference between carbon fiber and epoxy, a sample surface with less than 100 nm roughness is considered to be well polished. All machined specimens were placed in a desiccator at ambient temperature to avoid further moisture after preparation; the weight was recorded just prior to the start of the environmental degradation. All AFAM measurements followed the same procedure, where samples rested in lab air for two hours prior to AFAM measurement after removal from the boiling water degradation system.

3.4.2. SEM Imaging of Degraded Composites

In order to characterize the physical degradation of the composite during boiling water exposure prior to performing quantitative measurements, SEM images are taken before and after exposure for composite samples, as in Figure 3.12. The composites are seen to have cracks in the interfacial region between the fiber and matrix after boiling degradation. This is an example of the concerns regarding interfacial regions during CFRP degradation, and a goal of this research. In general, the cracks were found to occur in regions facing the open matrix regions, as shown in Figure 3.13. The primary reason for this may be the much stronger shrinkage of the epoxy matrix as compared to the fibers. Where large open matrix regions are located, the epoxy will have a larger magnitude of contraction compared with dense fiber locations. The local deformation caused by the matrix shrinkage will not be uniform throughout the bulk composite, and cracks would occur. Figure 3.14 shows the percentage mass change of composite samples over the exposure time. The moisture absorption of the samples reaches saturation after approximately two days of boiling water degradation. Mass variation after two days of exposure was within the experimental error of measurement.

3.4.3. Effects of Degradation on the Matrix-Interphase

Near-fiber AFAM testing was performed using AFM semi-contact cantilevers (fNp11s, AIST), with tip radius of curvature of 40nm. Measurements follow the spatial point testing method described in the previous sections, strating from the epoxy matrix through the interphase region to carbon fibers (figure 3.15 (a)). Due to the large elastic modulus difference between the fiber and matrix, the probe geometry in the interphase measurement is measured based on SEM images rather than the more common calibration from reference materials. The contact stiffness variation across these measured locations clearly identifies the interphase region between the fiber and matrix, as observed in figure 3.15. Using the contact stiffness transition from the fiber to matrix, the interphase region width can be measured, resulting in an average value of ~600 nm. Due to different polishing rates between the fiber and matrix, a height change is present as measured by AFM to be ~100~200nm. The heigth change will result in ~9-18 degrees of slope along the interphase surface profile, and is negligible for the small radius of curvature AFM probes used for AFAM measurements and due to the sufficient applied normal load that allows the probe to be in contact with the interphase region. The AFAM technique often relies on high applied load to achieve a good quantitative determination, and, due to the necessities of high spatial resolution measurements, a probe radius below 50 nm is often used. Both the applied loads and small radius probe provide sufficient conditions for a nominally flat contact to be considered.

Utilizing the same AFM probes, single point AFAM measurements were also conducted on degraded CFRP samples. The contact stiffness of two and six days degraded composite specimens were measured in comparison with the undegraded case. The interphase width for the 2 and 6 days degraded samples were measured from the contact stiffness variations found from the fiber to matrix. Since the AFAM phase mapping demonstrated that the interphase region has similar properties and span in different radial directions from a fiber, only one direction is measured at AFAM spatial point testing to introduce less probe geometry change from contact wear. During the AFAM measurements for both undegraded and degraded samples, it has been consistently observed that the measured contact stiffness will be higher within a ~100nm region in the vicinity of the fiber-interphase interface. This increase in contact stiffness may due to two facts, one is the fiber sizing, the other is that the probe becomes partially in contact with the fiber edge. Contact between the fiber and matrix simultaneously may cause erroneous results in the AFAM mesurements due to inhomogeneous material response. Though, the increase can be used to dinstinguish the fiber interface in the composite. Spatially moving the measurement location further from the fiber-matrix interface continued a decrease in the contact stiffness. The decreased contact stiffness is associated with the interphase region around the fiber.. After ~500-600 nm spatial movement from the fiber interface, the contact stiffness is found to become nearly constant, indicating a bulk epoxy matrix region. . The interphase width was found to remain consistent over the the degradation time (Figure 3.16).

Due to the fact that carbon fibers absorb very little moisture and have strong resistance to high temperature [3.49-50], the bulk composite water intake in the accelerated degradation system is primarily achieved by water diffusion into the epoxy matrix. The diffusion, as discussed in a previous section in this chapter, results in the mechanical performance decrease, either by mechanical swelling or chemical scission of the polymer crosslinks. The mechanical performance decrease for the epoxy matrix as a function of degradation time can be alternatively addressed by comparing AFAM contact stiffness of the bulk matrix and the carbon fiber. The contact stiffness difference between the matrix and fiber is observed to be significantly greater for degraded specimens than undegraded cases, as shown in Figure 3.17. In addition, the specimens that underwent 6 days immersion were shown to have only a limited amount of matrix-fiber contact stiffness change when compared with the 2 day immersion case. In combination with the water absorption saturating at approximately 2 days, shown in figure 3.13, it clearly indicates that most of the degradation for the composite epoxy occurred in the first two days.

Based on the contact mechanics model (Hertzian), the elastic modulus variation of the epoxy throughout the degradation period can be calculated from the obtained contact stiffness. However, following the Hertzian analysis, the calculated elastic modulus results are found to be off from the bulk modulus values, for both epoxy matrix and fiber. This potentially could be occurring due to improper assumptions made using the AFAM model or for the Hertzian calculations. In our study, the geometry of the probe is measured by a single side view from the SEM. In reality, this may not be the true geometry if the tip is not an ideal body of revolution shape, making an erroneous assumption in the contact area. In addition, for most cases the center of the probe end would become flat after a couple of surface scans due to tip wear, which implies the contact may be better described by other models rather than the ideal spherical Hertzian case. The contact mechanics for non-Hertzian AFAM quantitative determination is discussed in the following chapter. Another potential issue that would affect the quantitative results is the visco-elastic nature of the epoxy, which will also be addressed in the following chapter. Nevertheless, the contact stiffness results utilizing the same set of probe tips has demonstrated variations in the contact stiffness which are utilized to quantitatively compare changes in the mechanical response of the epoxy matrix, and hence degradation, as well as spatial measurements of the interphase region.

In conclusion, carbon fiber composite specimens are fabricated by vacuum bagging and cut into small pieces could be tested on AFAM. The accelerated boiling degradation technique is performed on specimens after the surfaces are highly polished. SEM has been conducted to observe the composites and interphase region after boiling degradation. The AFAM technique is used to observe stiffness variation between carbon fibers and epoxy matrix. Quantitative changes of epoxy properties over boiling degradation exposure time have been shown to decrease. The slope of the fiber-matrix interface was shown to have no major effect on the contact stiffness results from AFAM. The interphase region has been demonstrated to posess similar width and mechanical properties from measurement in different radial directions. The near-fiber epoxy matrix elastic modulus measured by AFAM shows significant decrease over a 6 day degradation period, indicating a weakening of the matrix. Specimens reached their moisture saturation point after a 2 day period, which compares with the contact stiffness difference results between the fiber and matrix. The fiber-matrix interphase region is measured with AFAM to have a length of ~500-600nm, and was found consistent over degradation time.

3.4.4. Salt Water and Deionized Water Degradation Comparison for Interphase Regions in Composites

The salt and deionzed water degradation have been compared to observe the effects of each on the CFRP interphase region. SEM was used to scan the surface of undegraded, salt and deionzied water degraded composites. This study, in addition to the Raman spectroscopy and FTIR, is motivated by that the measurement of the fracture toughness of the composites had shown a more severe degradation occurring in composite samples exposed to salt water environments. From the chemical analysis, the deionized water immersion samples were observed to incur more damage than the salt water exposed samples.

Figures 3.19-3.21 indicate that both of the degraded samples have shown some degree of fiber detachments. However, there is more evidence of fiber detachment in the salt water boiling immersion samples than the boiling water immersion. One conculsion may be that the decrease in salt water boiling immersion fracture strength was due to an increased fiber-matrix interface failure. We can conclude from the results that the salt water exposure has more effect on the strength of the composites fiber-matrix interface, while the deionzied water will weaken the epoxy matrix more than salt water.

3.5. Conclusion

AFAM is shown to be an effective quantitative tool to understand the nanomechanical properties of carbon fiber reinforced polymer composites. The changes in the epoxy elastic modulus were able to be studied as the function of degradation under different environments and time of exposure. The mechanical property loss could be explained by chemical analysis employing FTIR and Raman spectroscopy, both of which found the hydrolysis of the C-O-C and Epoxide bonding as the potential reasons. The fiber-matrix interphase region has been quantitatively studied by AFAM and the elastic modulus variations have been measured as a function of spatial position and degradation time. The fiber-matrix interface is shown to be more affected by the salt water immersion than the deionized water exposure, which explains macro-scale experimental results that found fracture toughness measurements decrease with a similar trend. The deionized water condition will result in a slightly larger amount of modulus decrease than the salt water for epon 862 epoxy in the accelerated degradation system. However, the fiber-matrix interfaces are found to be more severely debonded by the salt water condition.

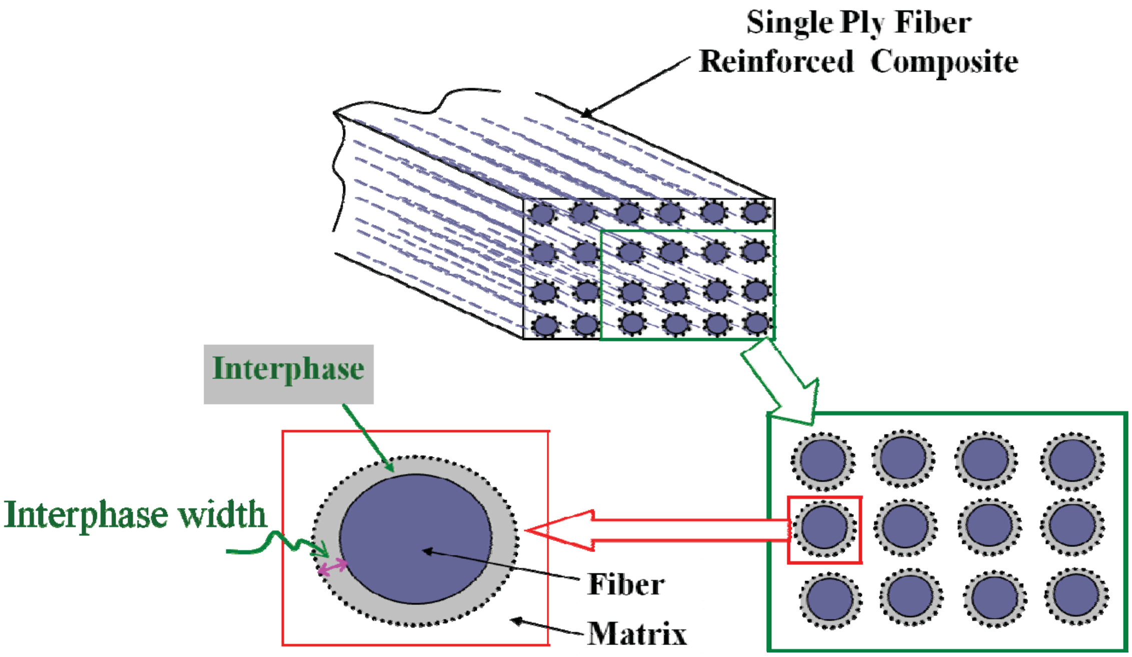

Figure 3.1. Microstructure of single ply fiber reinforced composite.

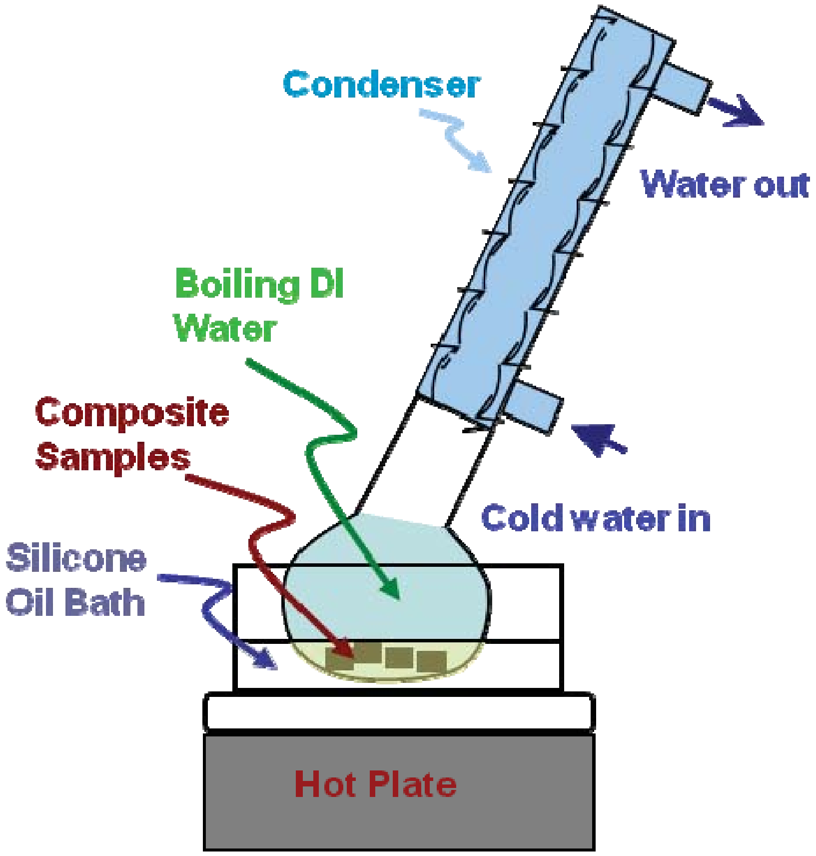

Figure 3.2. Boiling water degradation set up. Silicone oil bath is used to generate an even heat on the flask and to reduce direct heating of composite samples. Cold water condenser is used to retain evaporate.

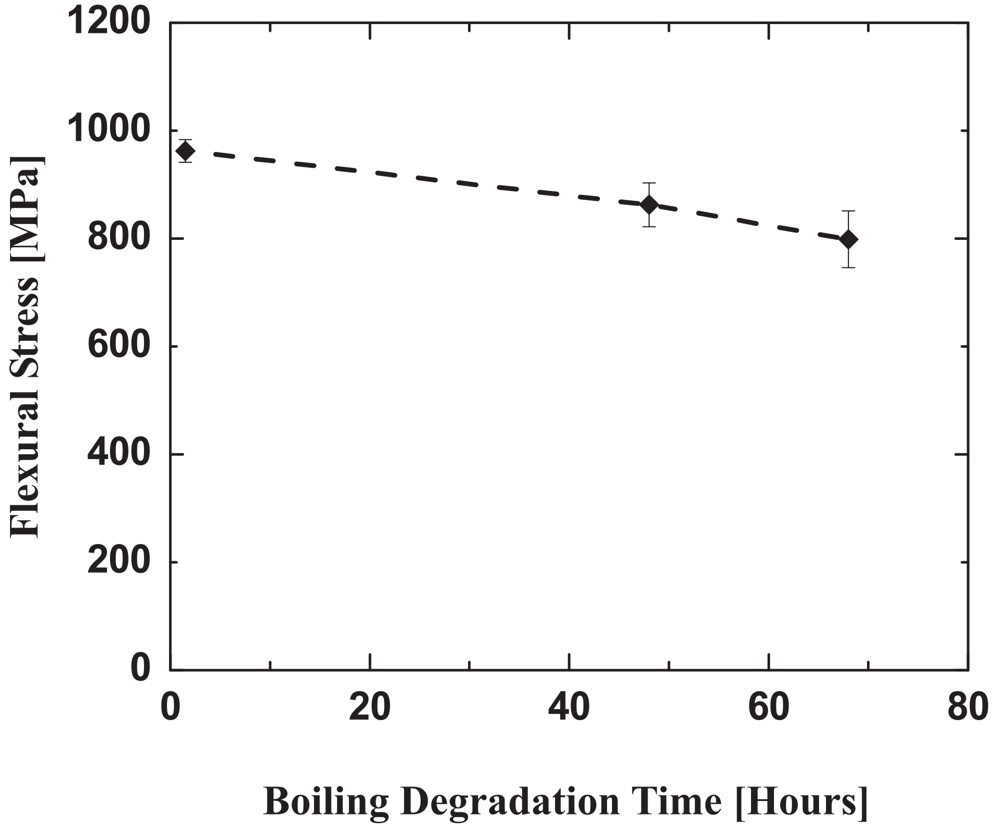

Figure 3.3. Flexural stress measurements for composite specimens as the function of exposure time to boiling deionized water environment.

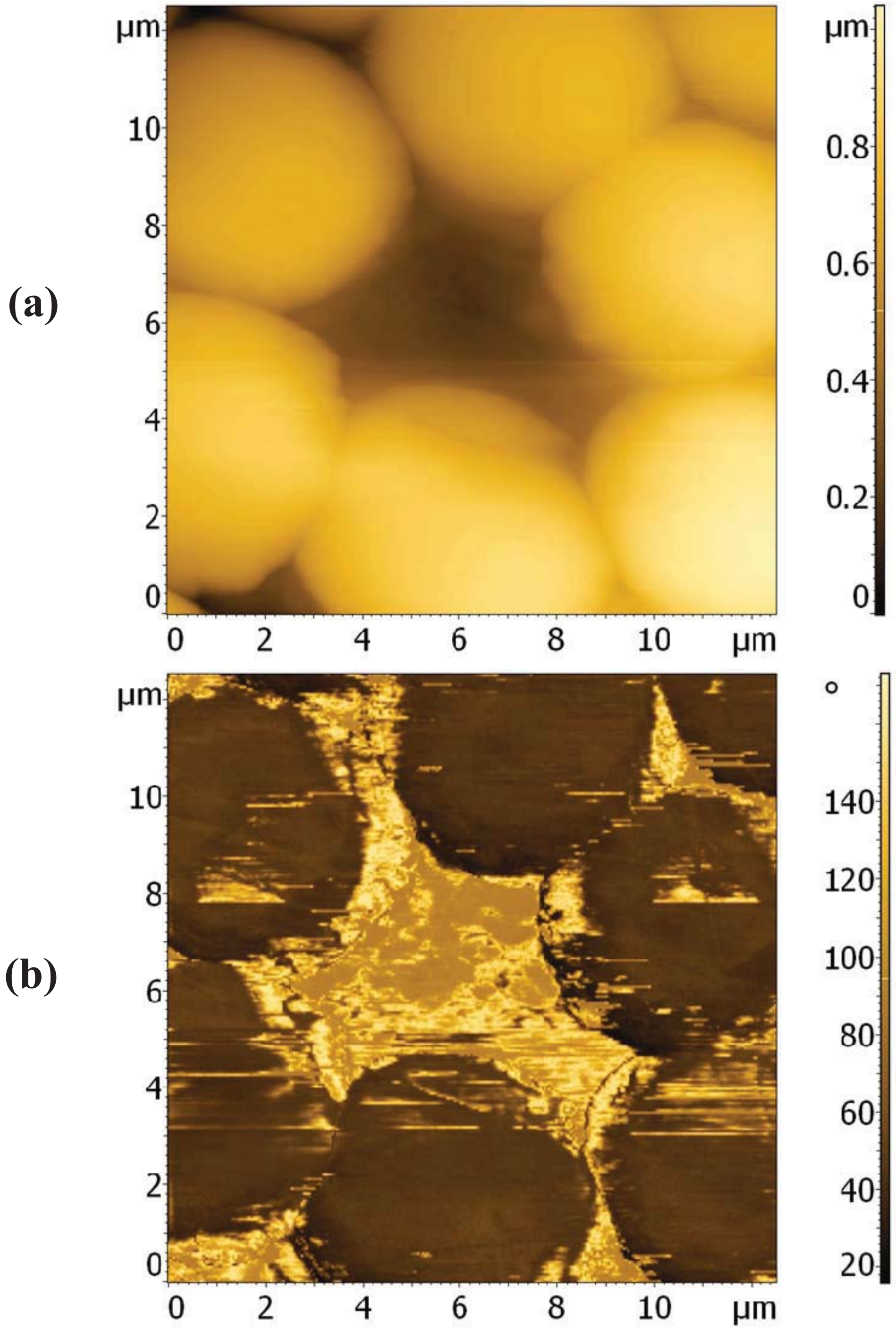

Figure 3.4. AFAM scan of a fiber reinforced composite surface at 1123.509 KHz, (a) surface topography image, (b) AFAM phase image.

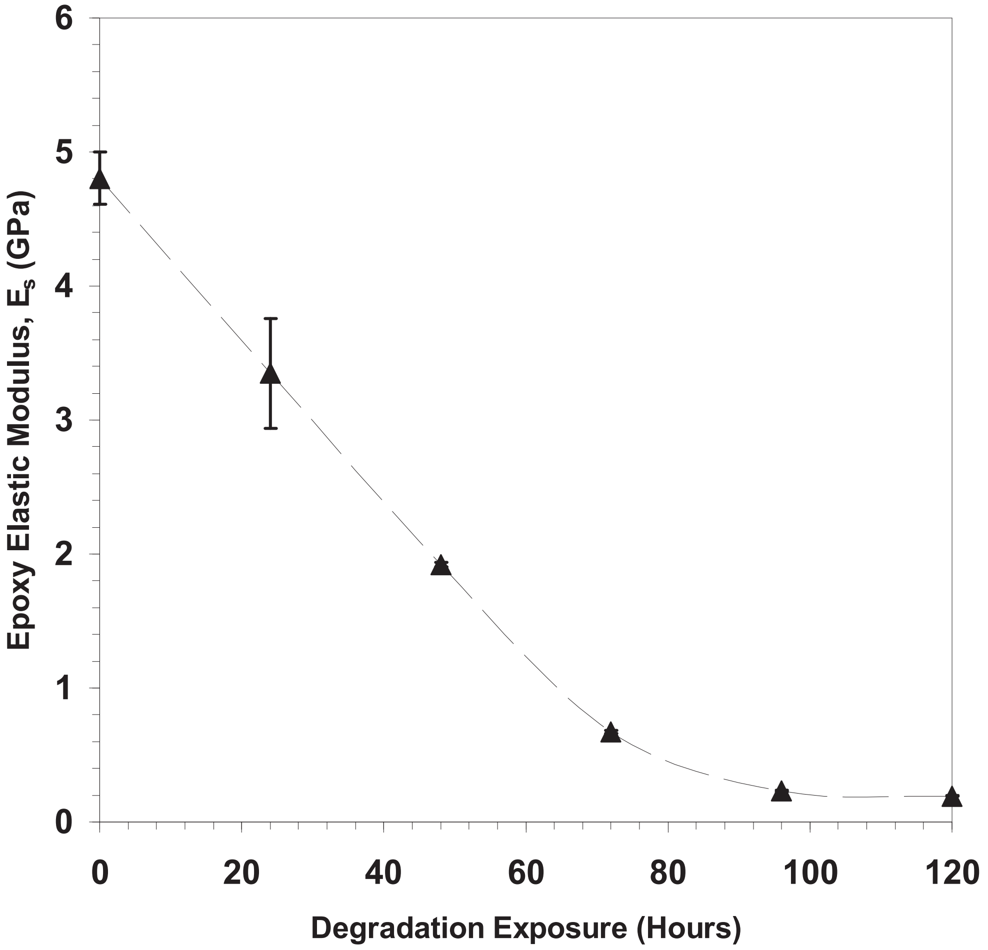

Figure 3.5. Near-fiber epoxy matrix elastic modulus (GPa) versus boiling degradation period (hours).

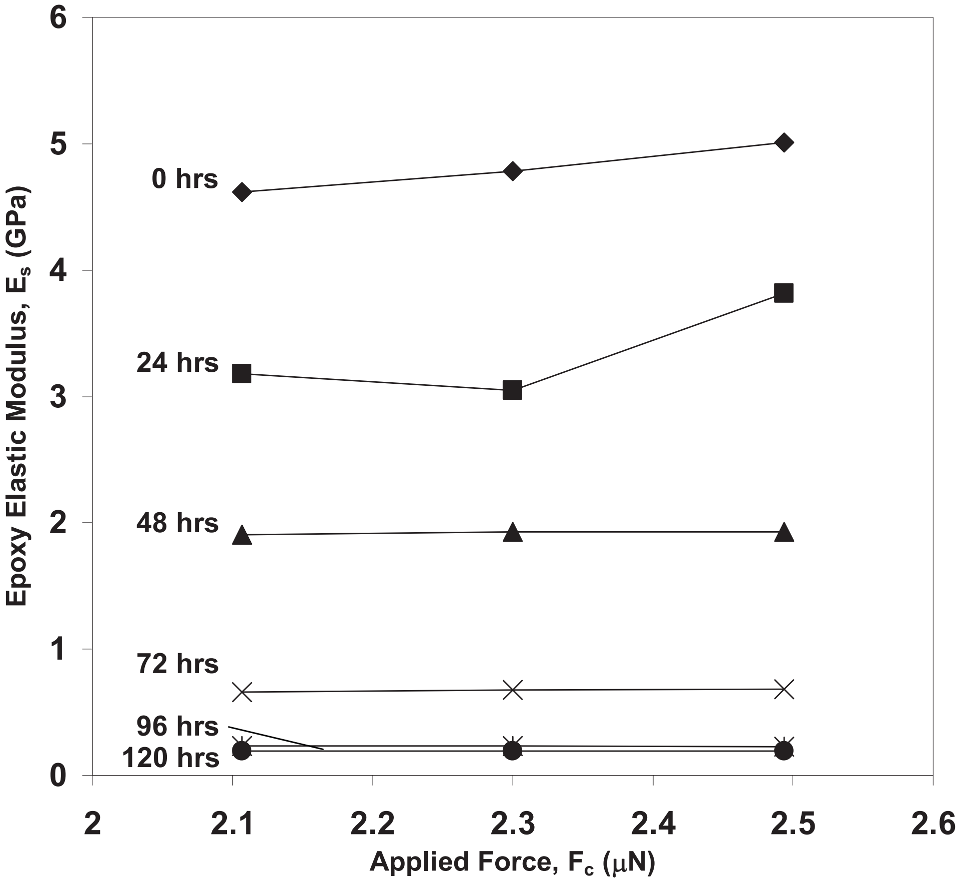

Figure 3.6. Epoxy elastic modulus versus applied normal force for 0 hours to 120 hours boiling degradation exposure.

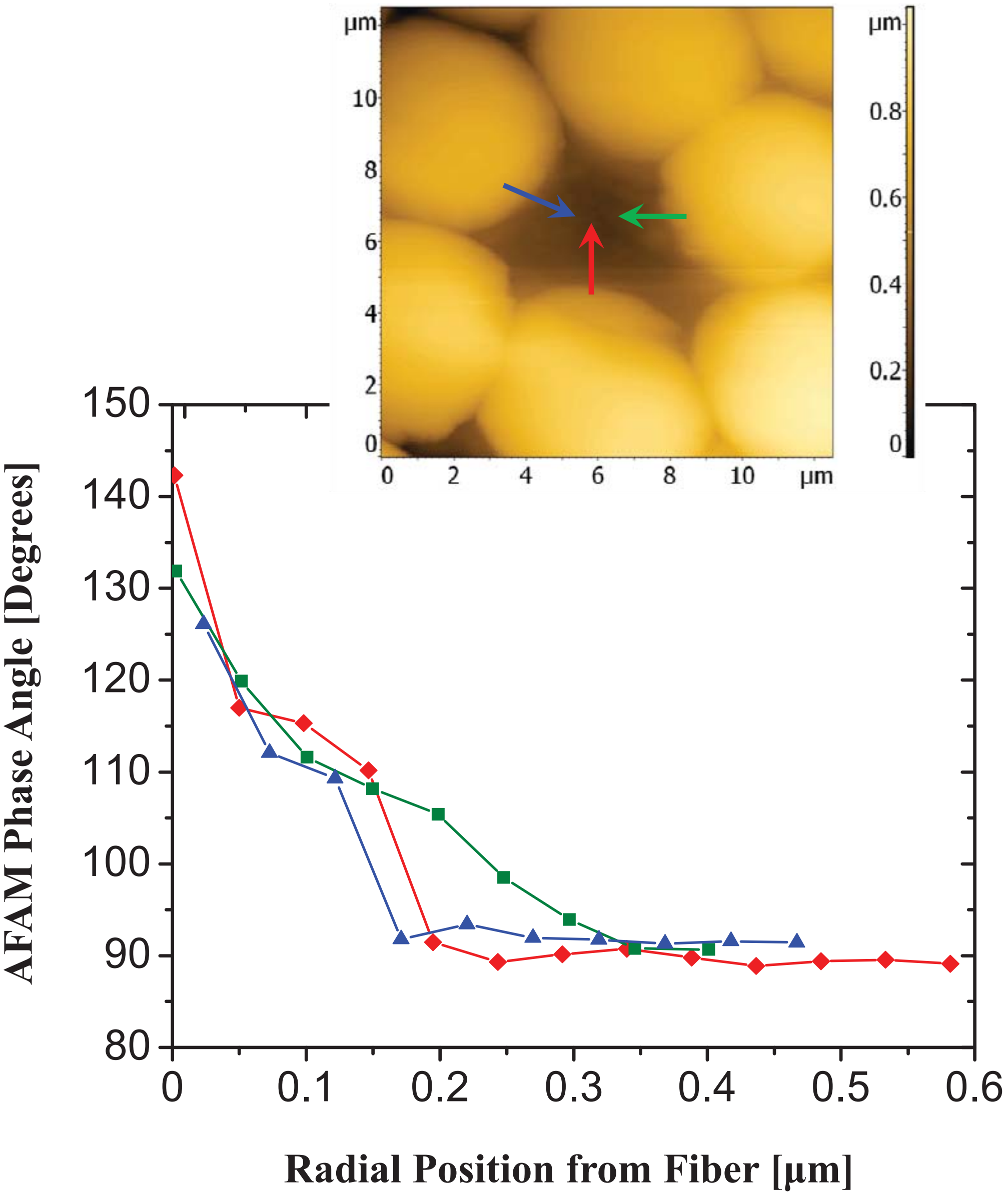

Figure 3.7. Spatial variation from the fiber-matrix interface in the AFAM phase angle signal, which represents a stiffer material for higher phase angle changes. Three discrete locations are plotted from around a fiber. Interphase is estimated from the results to be 200 – 300 nm in width.

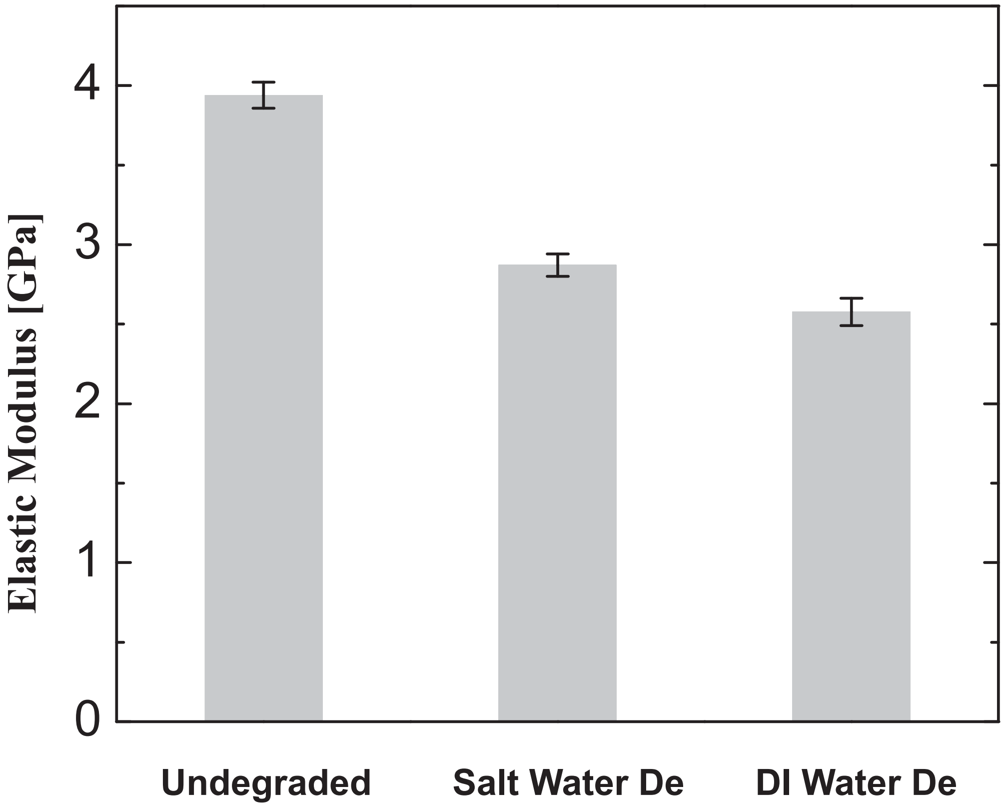

Figure 3.8. The comparison of AFAM quantitative elastic modulus measurement of undegraded, sea and deionized water degraded epon862 epoxy.

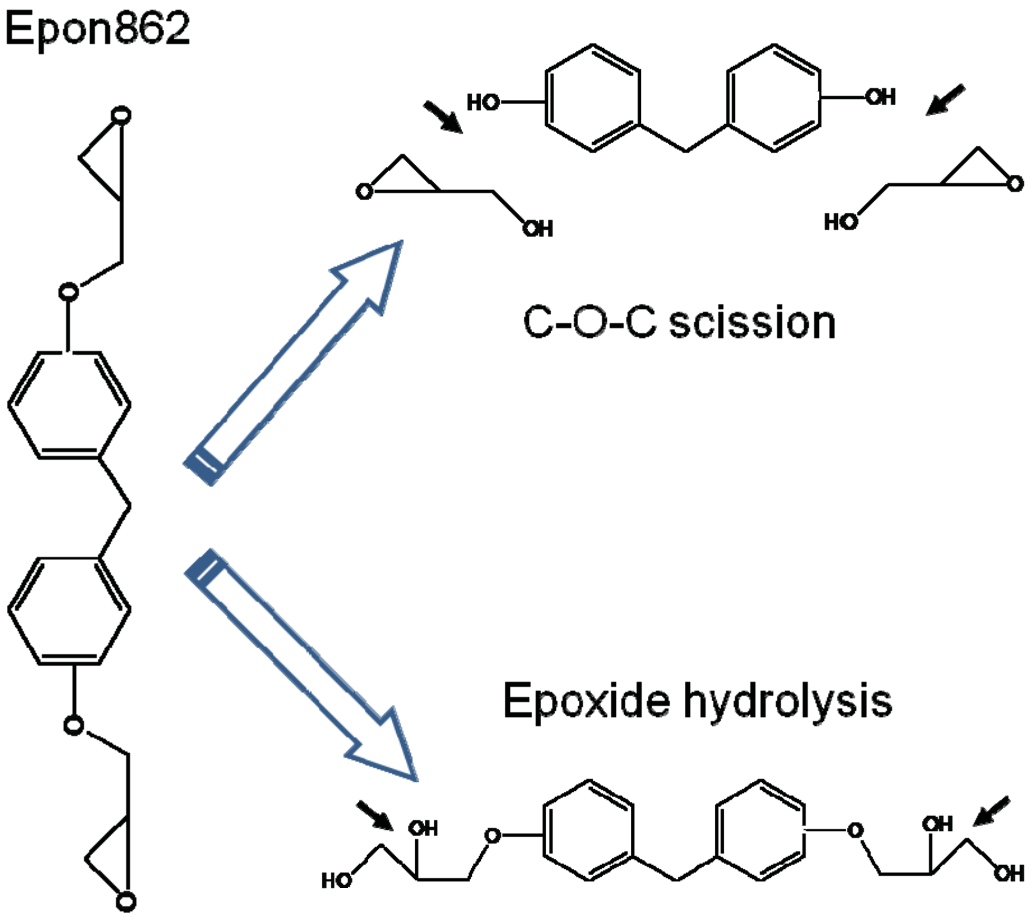

Figure 3.9. C-O-C and Epoxide hydrolysis reactions

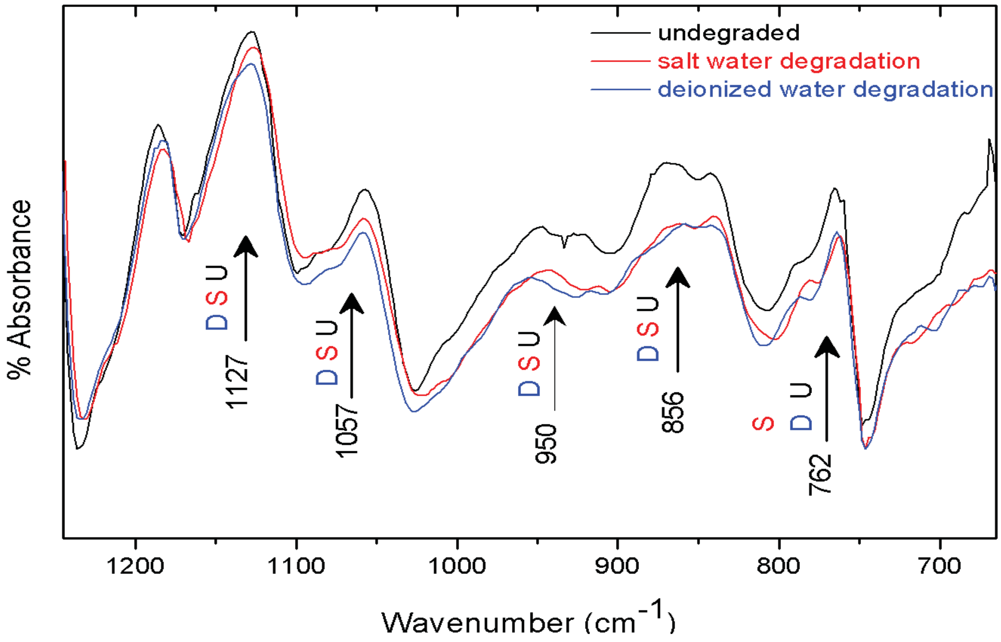

Figure 3.10. FITR measurements on undegraded, salt and deionized water degraded samples. Where the “D” in blue represents deionized water degraded sample, “S” in red indicates salt water degraded specimen, and the “U” in black is used for undegraded sample.

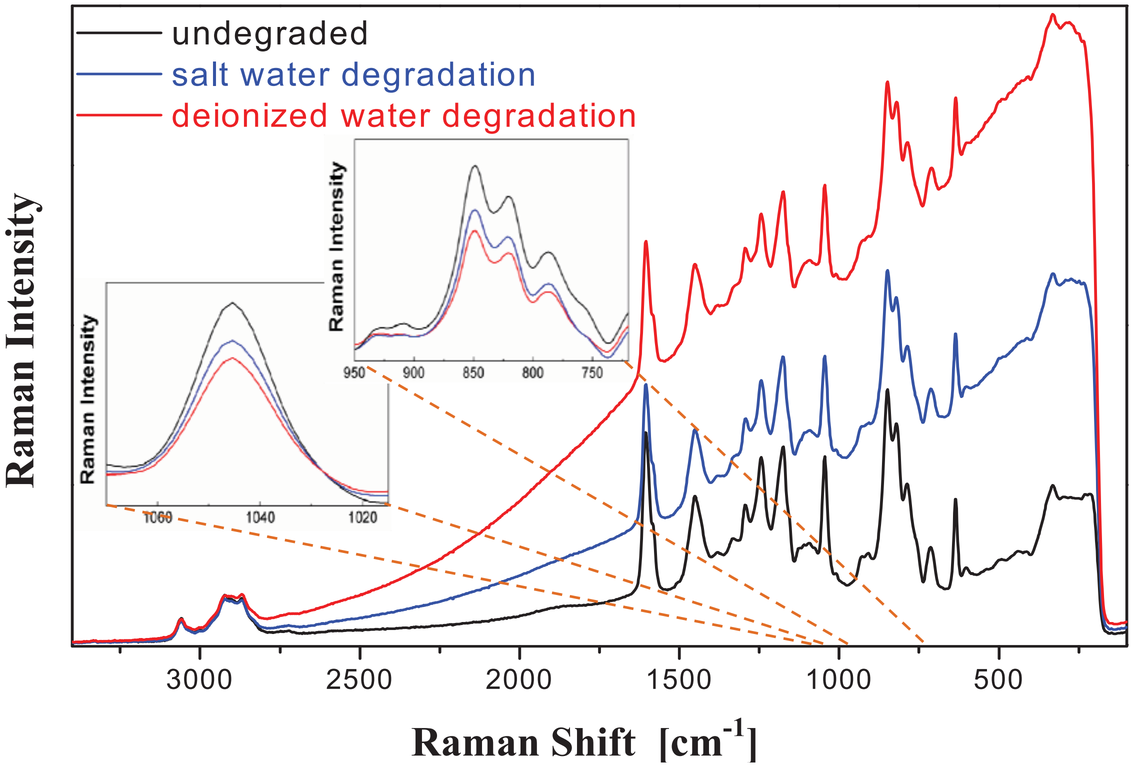

Figure 3.11. Raman measurements on undegraded, sea and deionized water degraded samples. Where the two C-O-C and Epoxide bonding were both compared for all the three condition measured.

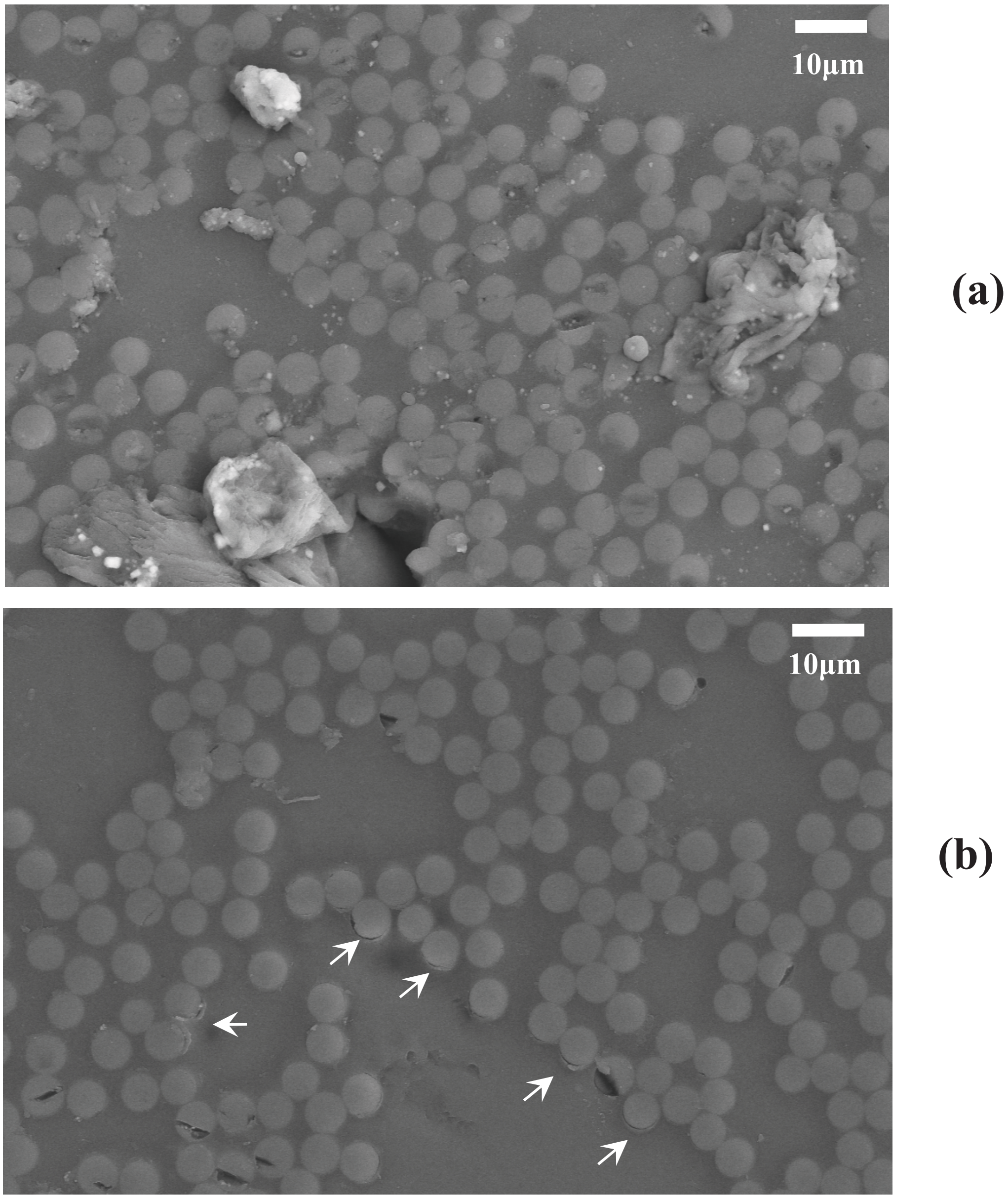

Figure 3.12. SEM images of carbon fiber reinforced epoxy composites, (a) undegraded composite sample, (b) boiling water degraded composite sample, white arrows indicate locations of observed interfacial cracks

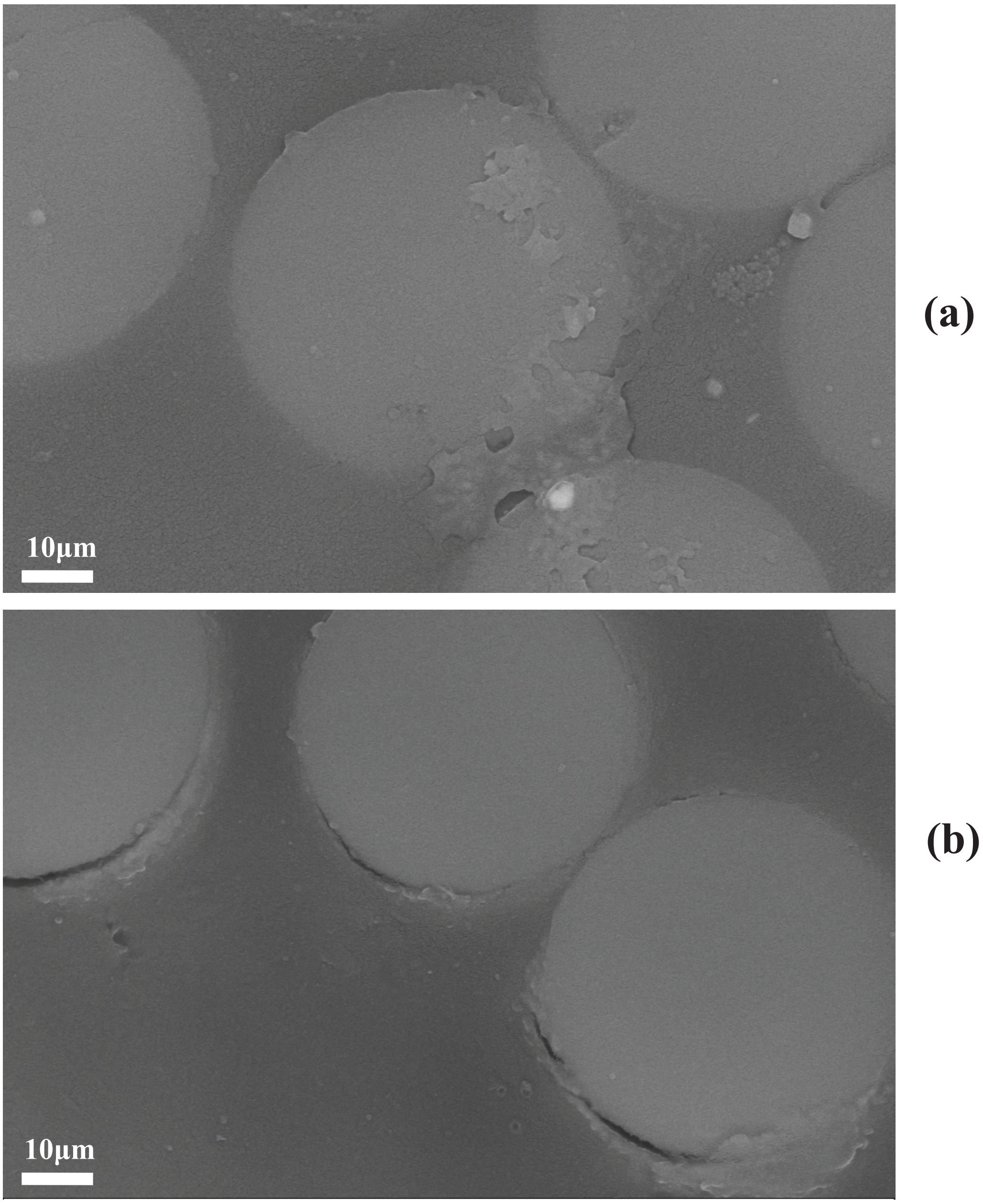

Figure 3.13. High resolution SEM images of carbon fiber reinforced epoxy composites, (a) undegraded composite sample, (b) boiling water degraded composite sample; fiber-matrix interface cracks are clearly visible in (b).

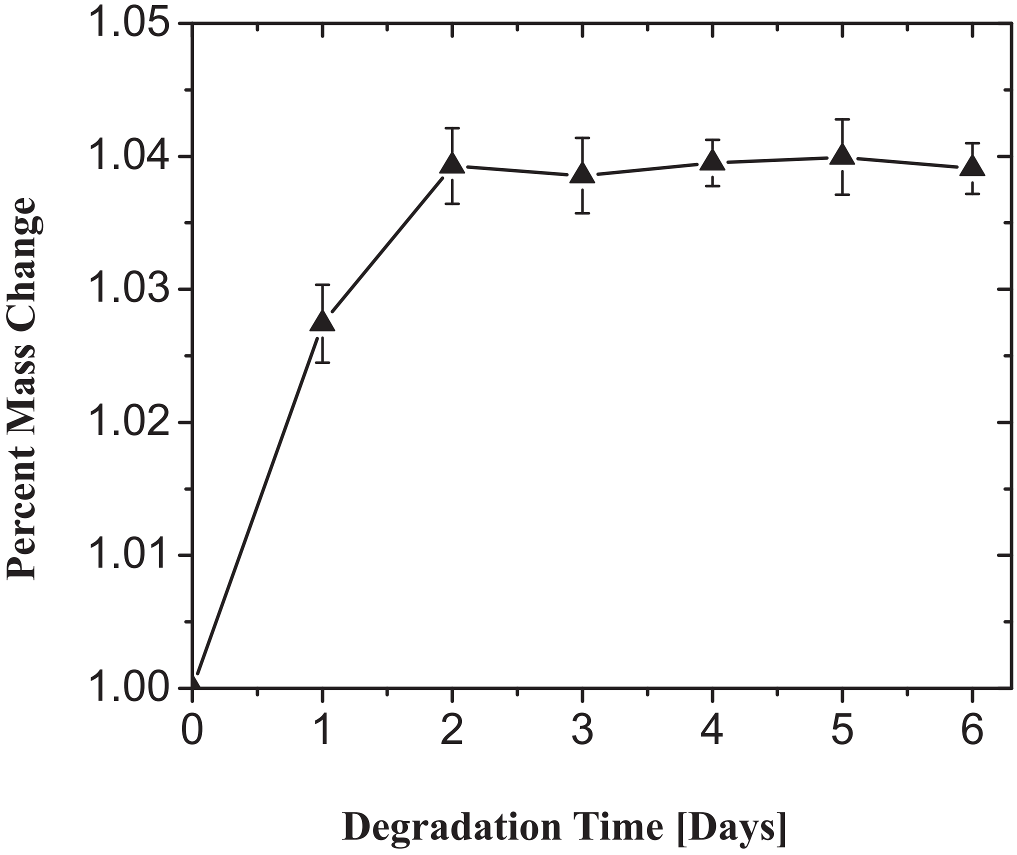

Figure 3.14. Percentage of sample mass changes over time in boiling DI water

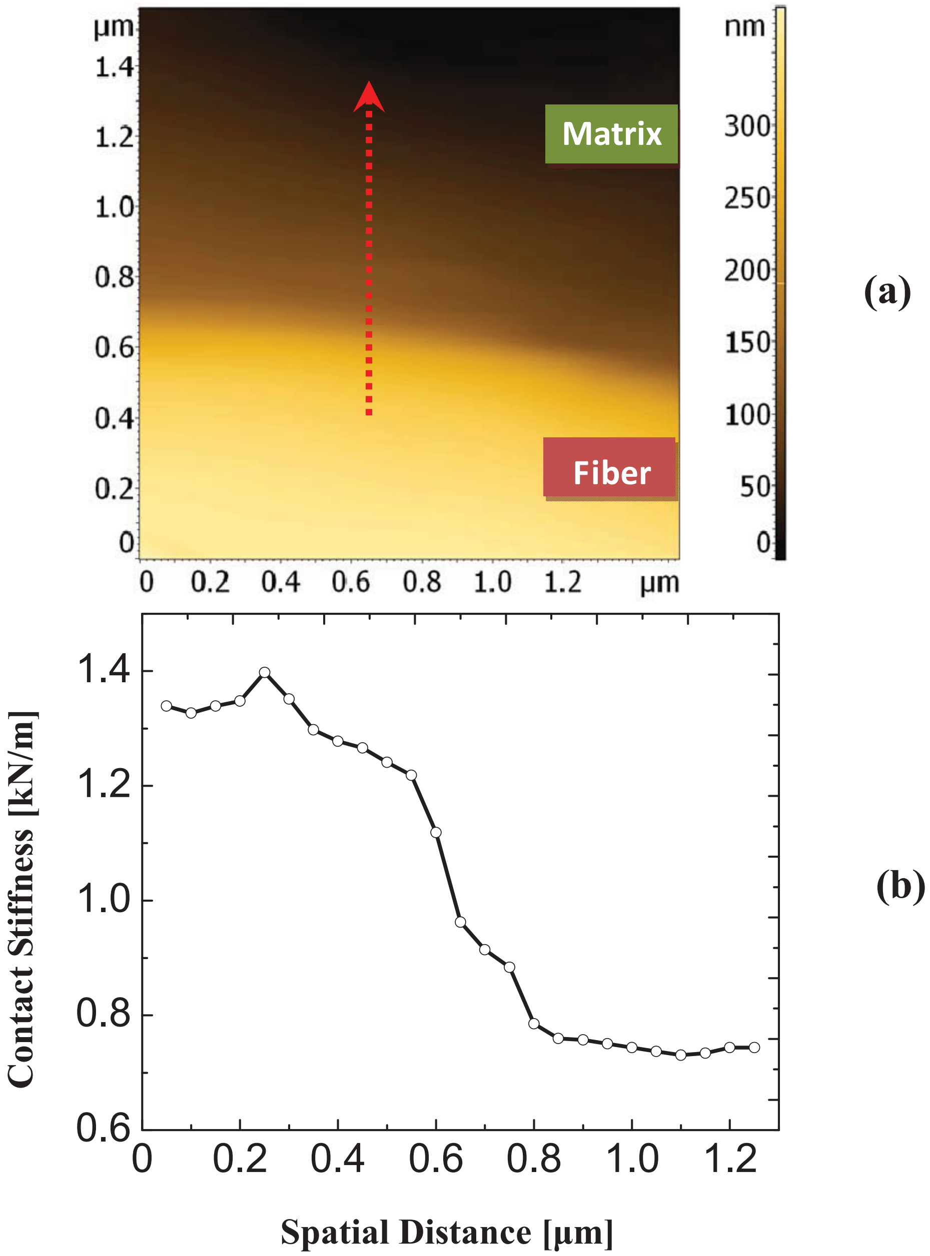

Figure 3.15. (a) Profile height and contact stiffness of interphase region

(b) Spatial Point AFAM measurement

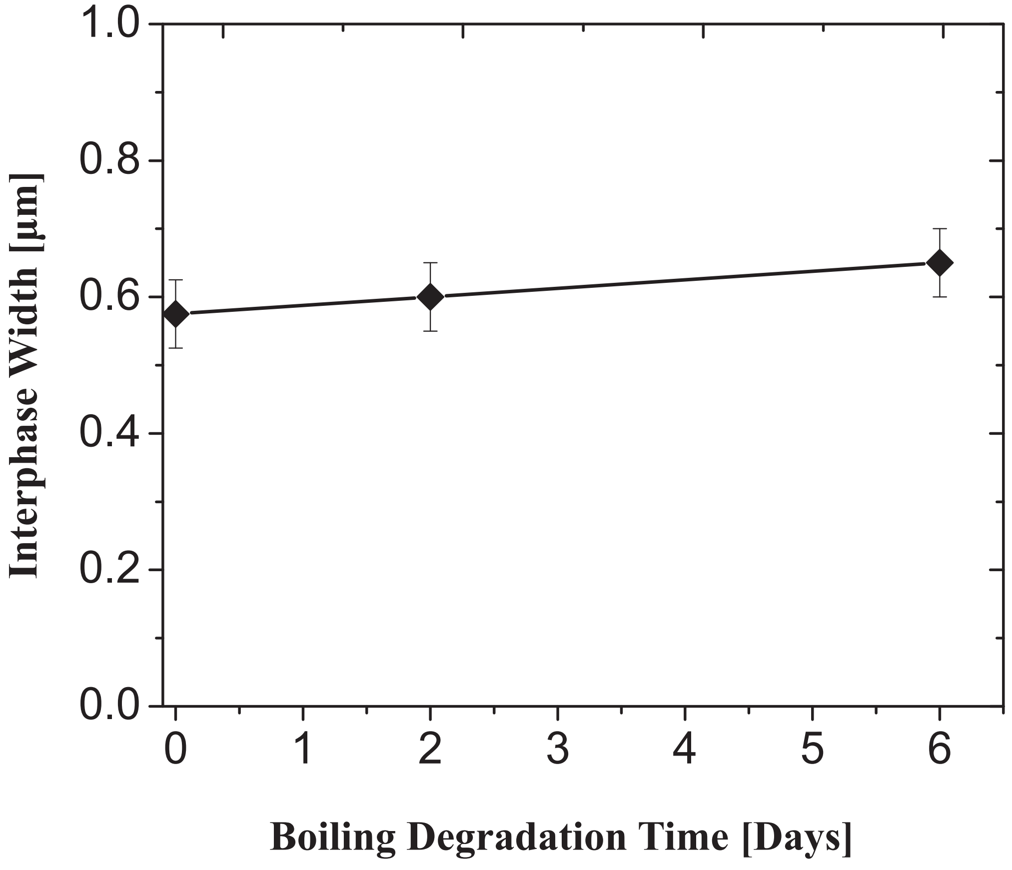

Fig.ure 3.16. Size of interphase region over degradation time.

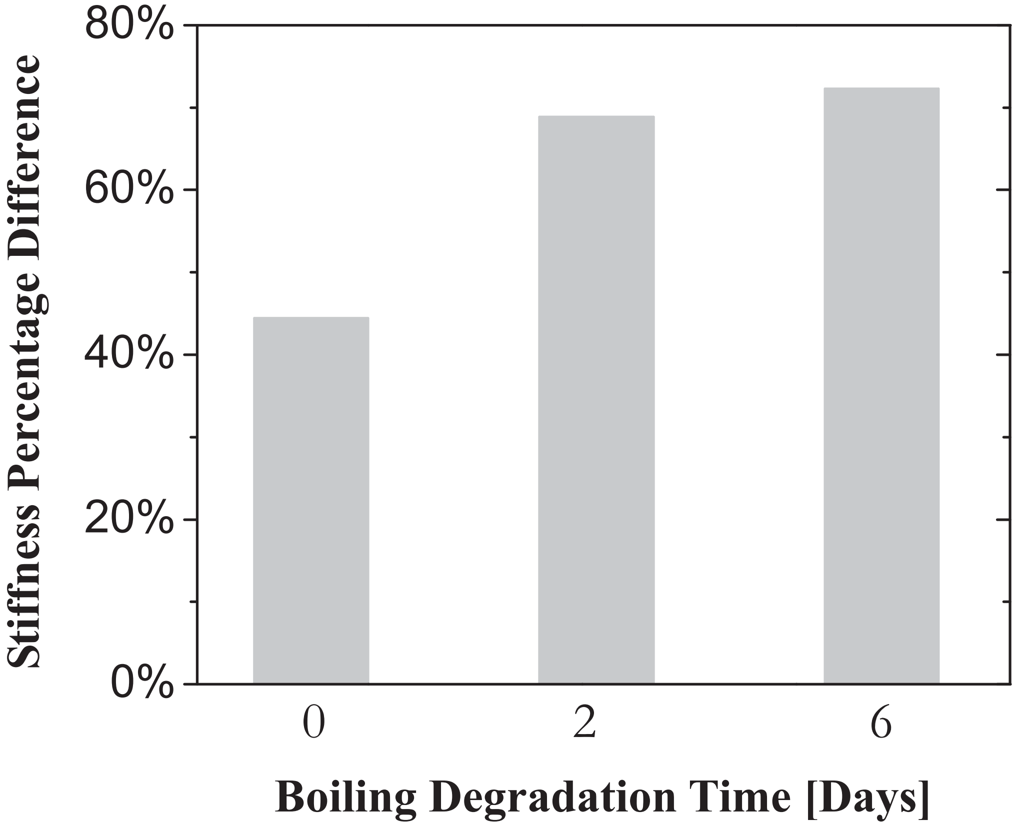

Figure 3.17. Contact stiffness difference between fiber and epoxy.

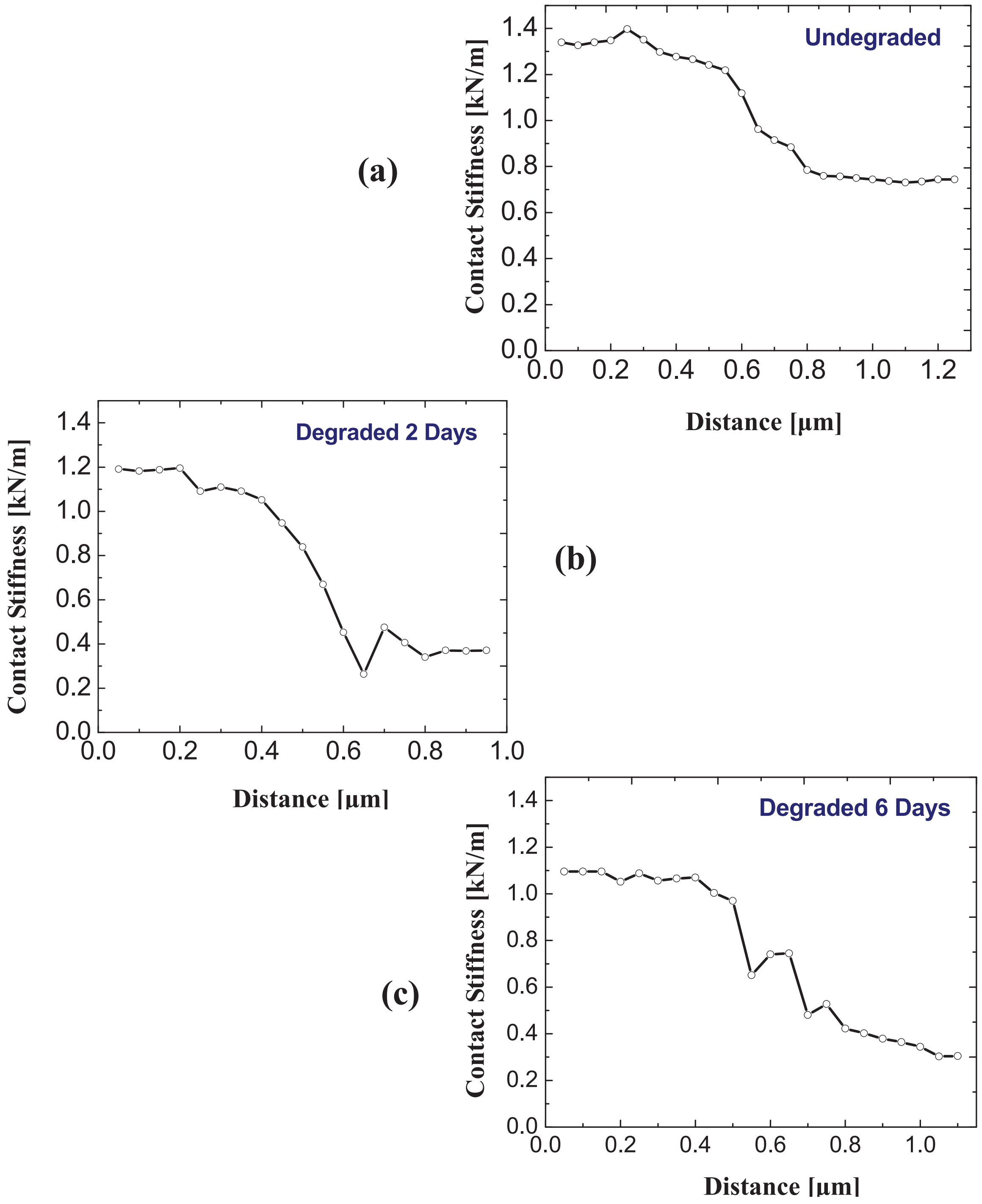

Figure 3.18. (a) Undegraded sample Interphase; (b) Interphase of sample with 2 days degradation; (c) Interphase of sample with 6 days degradation.

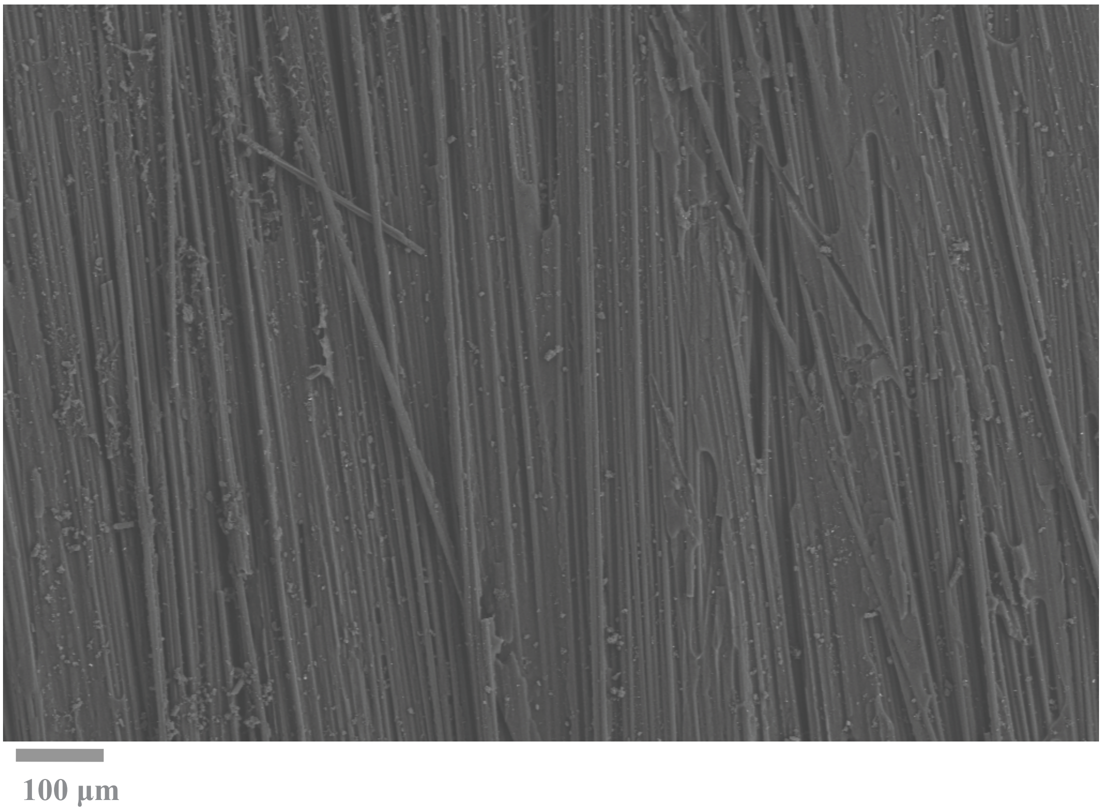

Figure 3.19. Undegraded composites surface.

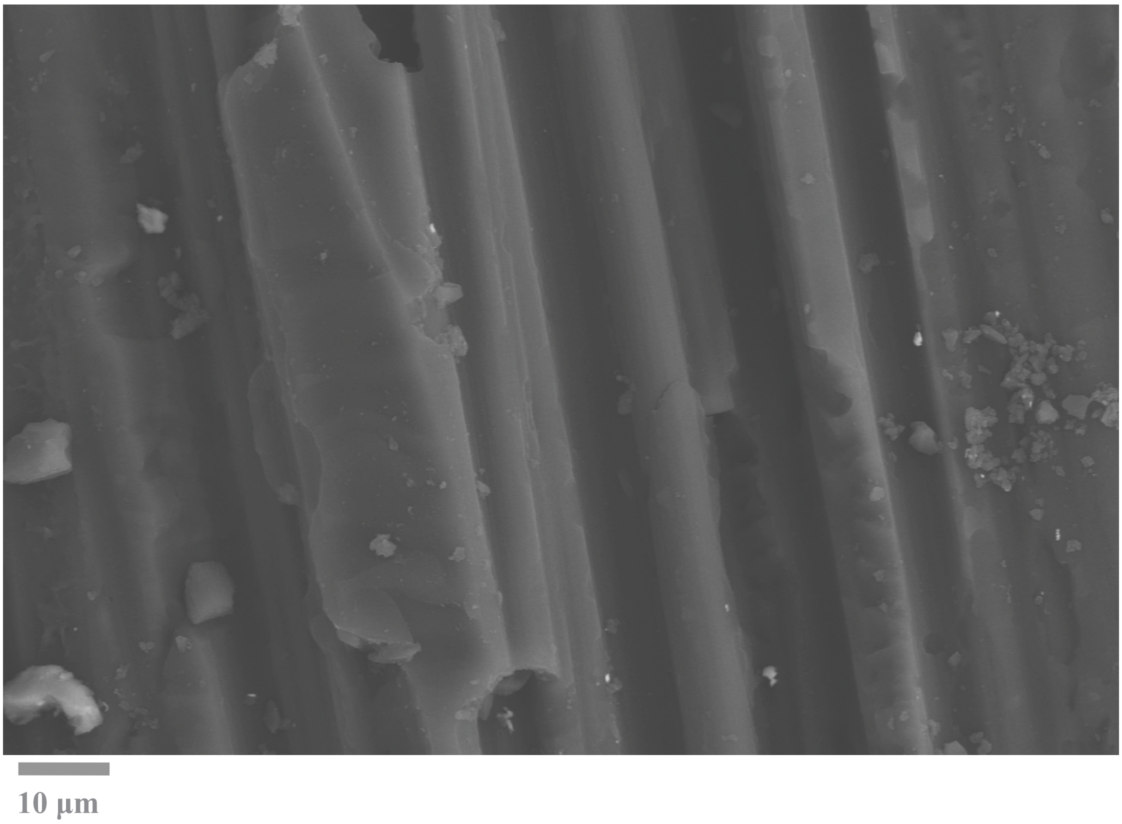

Figure 3.20. 3 days deionized water immersion.

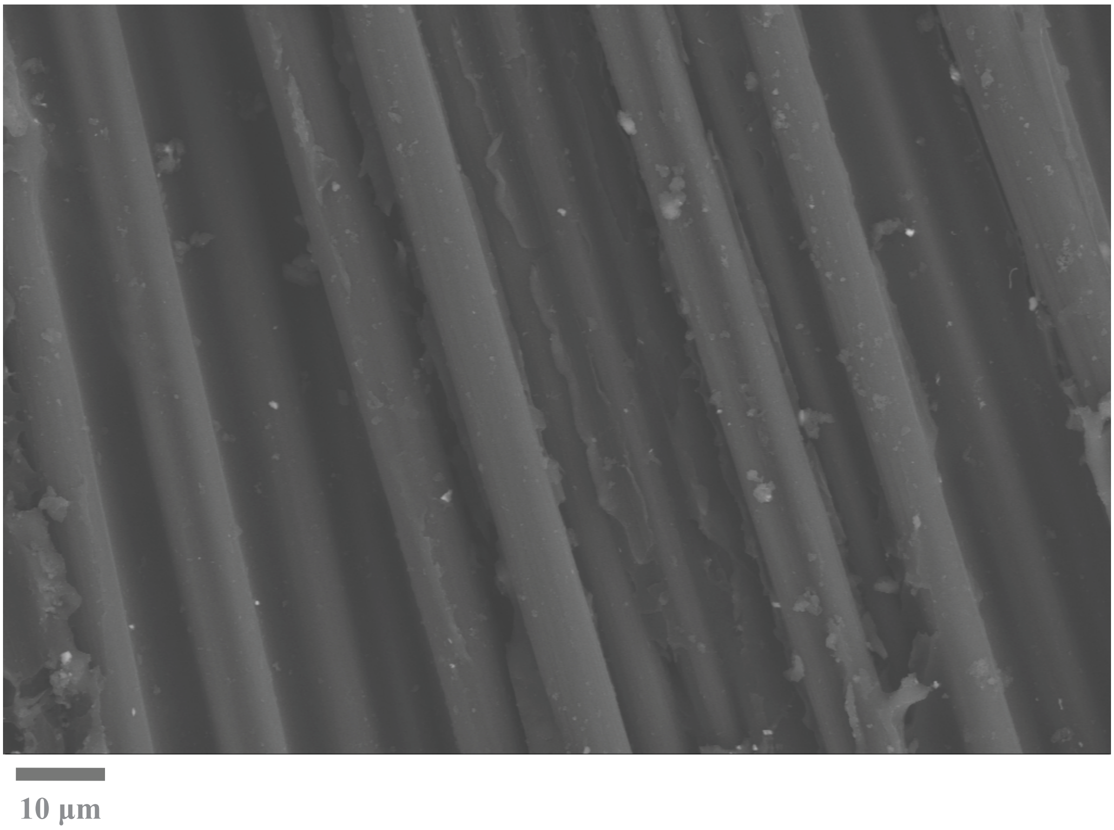

Figure 3.21. 3 days salt water immersion.

Table 3.1. Properties of IM7 carbon fiber and EPON 862 epoxy [3.51-59].

Property	IM7 Fiber	EPON 862
Longitudinal Modulus (GPa)	276	3~6
Poisson's Ratio	0.33	0.3~0.33

3.6. References

[3.1] Liao K, Shultheisz CR, Hunston DL, Brinson LK. Long-term Durability of Fiber-Reinforced Polymer-Matrix Composite Materials for Infrastructure Applications: A Review. SAMPE Journal of Advanced Materials 1998;30(4):3-40.

[3.2] Jones FR. Durability of Reinforced Plastics in Liquid Environments. In: Pritchard G, editor. Reinforced Plastics Durability: Woodhead Publishing Company; 1999. p. 70-110.

[3.3] Springer GS. Environmental Effects on Composite Materials: Technomic; 1984.

[3.4] Mader E, Grundke K, Jacobasch Hj, Wachinger G, . Surface Interphase And Composite Property Relations In Fiber-Reinforced Polymers. Composites Science and Technology. 1994;25(7):739-44.

[3.5] Hodzic A, Stachurski ZH, Kim JK. Nano-indentation of polymer-glass interfaces Part I. Experimental and mechanical analysis. Polymer. 2000;41(18):6895-905.

[3.6] Hodzic A, Kim JK, Lowe AE, Stachurski, ZH. The effects of water aging on the interphase region and interlaminar fracture toughness in polymer-glass composites. Composites Science and Technology. 2004;64(13-14):2185-95.

[3.7] Black J. Biological performance of materials. 3rd ed. New York: Marcel Dekker; 1999.

[3.8] Nakamura K, Hatakeyama T, Hatakeyama H. Relationship between hydrogen bonding and bound water in polyhydroxystyrene derivatives. Polymer. 1983;24:871-6.

[3.9] Darvell BW. Materials science for dentistry. 5th ed. Hong Kong: BW Darvell; 1998.

[3.10] Mary P. Walker, Paulette Spencer, J. David Eick. Mechanical property characterization of resin cement after aqueous aging with and without cyclic loading. Dental Materials. 2003;19:645-52.

[3.11] Kazuto Tanaka, Kohji Minoshima, Witold Grela, Kenjiro Komai. Characterization of the aramid/epoxy interfacial properties by means of pull-out test and influence of water absorption. Composites Science and Technology. 2002;62:2169-77.

[3.12] Gao S-L, Mäder E. Characterisation of interphase nanoscale property variations in glass fiber reinforced polypropylene and epoxy resin composites. Composites: Part A. 2002;33:559-76.

[3.13] Wright OB, Nishiguchi N. Vibrational dynamics of force microscopy: Effect of tip dimensions. Applied Physics Letters. 1997;71(5):626-8.

[3.14] Ying Wang, Thomas H. Hahn. AFM characterization of the interfacial properties of carbon fiber reinforced polymer composites subjected to hygrothermal treatments. Composites Science and Technology. 2007;67:92–101.

[3.15] Kim JK, Hodzic A. Nanoscale characterisation of thickness and properties of interphase in polymer matrix composites. Journal Of Adhesion. 2003;79(4):383-414.

[3.16] VanLandingham, M. R., Dagastine, R. R., Eduljee, R. F., McCullough, R. L., Gillespie, J. W. Characterization of nanoscale property variations in polymer composite systems: 1. Experimental results. CompositesPart A. 1999;30:75-83.

[3.17] Hurley DC, Shen K, Jennett NM, Turner JA. Atomic force acoustic microscopy methods to determine thin-film elastic properties. Journal of Applied Physics. 2003;94(4):2347-54.

[3.18] Rabe U, Amelio S, Kester E, Scherer V, Hirsekorn S, Arnold W. Quantitative determination of contact stiffness using atomic force acoustic microscopy. Ultrasonics. 2000;38(1-8):430-7.

[3.19] Hirsekorn S, Arnold W. High-resolution materials characterization by conventional and near-field acoustic microscopy. Ultrasonics. 1998;36(1-5):491-8.

[3.20] Ngwa W, Luo W, Kamanyi A, Fomba KW, Grill W. Characterization of polymer thin films by phase-sensitive acoustic microscopy and atomic force microscopy: a comparative review. Journal of Microscopy-Oxford. 2005;218:208-18.

[3.21] Rabe U, Arnold W. Acoustic Microscopy by Atomic-Force Microscopy. Applied Physics Letters. 1994;64(12):1493-5.

[3.22] Kester E, Rabe U, Presmanes L, Tailhades P, Arnold W. Measurement of mechanical properties of nanoscaled ferrites using atomic force microscopy at ultrasonic frequencies. Nanostructured Materials. 1999;12(5-8):779-82.

[3.23] Hurley DC, Geiss RH, Kopycinska-Muller M, Muller J, Read DT, Wright JE, Jennett NM, Maxwell AS. Anisotropic elastic properties of nanocrystalline nickel thin films. Journal of Materials Research. 2005;20(5):1186-93.

[3.24] ASTM B117-03. Standard Practice for Operating Salt Spray (Fog) Apparatus. 2003.

[3.25] Holliday L. Composite Materials. Amsterdam: Elsevier; 1966.

[3.26] Jozef Stabik. Ageing of laminates in boiling NaCl water solution. Polymer Testing 2005;24:101–3

[3.27] MR Piggott. Water Absorption of Resins and Composites: II. Diffusion in Carbon and Glass Reinforced Epoxies. Journal of Composites Technology and Research. 1987;9(4).

[3.28] A. Brent Strong. Practical Aspects Of Carbon Fiber Surface Treatment And Sizing. Composites Manufacturing,2003.

[3.29] Gardiner, D.J. Practical Raman spectroscopy: Springer-Verlag; 1989.

[3.30] G. Z. XIAO, M. E. R. SHANAHAN. Water Absorption and Desorption in an Epoxy

Resin with Degradation

Journal of Polymer Science: Part B: Polymer Physics. 1997;35:2659-70.

[3.31] Li-Rong Bao, Albert F.Yee. Effect of temperature on moisture absorption in a bismaleimide resin and its carbon fiber composites. Polymer 2002;43:3987-97.

[3.32] Lionel T. Keene, Gary P. Halada, Clive R. Clayton. Failure of navy coating systems 1: chemical depth profiling ofartificially and naturally weathered high-solids aliphatic poly(ester-urethane) military coating systems. Progress in Organic Coatings. 2005;52:173–86.

[3.33] Lionel T. Keene, M. Jaime Vasquez, Clive R. Clayton, Gary P. Halada. Failure of navy coating systems 2: failure pathways of artificially weathered navy coating systems applied to chromate conversion coated AA2024-T3 substrates. Progress in Organic Coatings. 2005; 52:187–95.

[3.34] Lionel T. Keene, Thomas Fiero, Clive R. Clayton, Gary P. Halada, David Cardoza, Tom Weinacht. On the use of femtosecond laser ablation to facilitate spectroscopic depth profiling of heterogeneous polymeric coatings. Polymer Degradation and Stability. 2005; 89:393-409.

[3.35] Hilmar Koerner, Devesh Misra, Ashley Tan, Lawrence Drummy, Peter Mirau, Richard Vaia Montmorillonite-thermoset nanocomposites via cryo-compounding. Polymer

2006;47:3426–35.

[3.36] Maria Partini, Roberto Pantani. FTIR analysis of hydrolysis in aliphatic polyesters. Polymer Degradation and Stability. 2007;92:1491-7.

[3.37] Saeed Ziaee Erik T. Thostenson , Tsu-Wei Chou. Processing and electrical properties of carbon nanotube/vinyl ester nanocomposites. Composites Science and Technology. 2009;69:801–4.

[3.38] Infrared and Raman Characteristic Group Frequencies: Tables and Charts 3rd ed. New York: John Wiley & Sons.

[3.39] Trong-ming Don, J. P. Bell. Fourier Transform Infrared Analysis of Polycarbonate/Epoxy Mixtures Cured with an Aromatic Amine. Journal of Applied Polymer Science. 1998;69:2395–407.

[3.40] Naomi Eidelman, Dharmaraj Raghavan, Aaron M. Forster, Eric J. Amis, Alamgir Karim. Combinatorial Approach to Characterizing Epoxy Curing. Macromol Rapid Commun. 2004;25:259-63.

[3.41] Xuerong Zhang, James K. Pugh, Philip N. Ross, Jr. Evidence for Epoxide Formation from the Electrochemical Reduction of Ethylene Carbonate. Electrochemical and Solid-State Letters. 2001;4(6):A82-A4.

[3.42] Bernadette Ann Higgins. CARBON NANOFIBER-POLYMER COMPOSITES FOR

ELECTRONIC APPLICATIONS: University of Akron; 2006.

[3.43] Eorgakopoulos Andreas, Iordanidis Andreas, Kapina Victoria. Study of low rank greek coals using FTIR spectroscopy. Energy sources. 2003;25:995-1005.

[3.44] E. van Overbeke, V. Carliera, J. Devaux, J.T. Carter, P.T. McGrail, R. Legras. The use of Raman spectroscopy to study the reaction between an amine-terminated thermoplastic and epoxy resins. Polymer 2000;41:8241-5.

[3.45] Jacky Mallégol, , Gardette, Jean-Luc, Lemaire, Jacques. Long-term behavior of oil-based varnishes and paints I. Spectroscopic analysis of curing drying oils. Journal of the American Oil Chemists' Society. 1999;10:967-76.

[3.46] Christopher N. Young, William R Scott, Guy M Connelly, Clive R. Clayton, Richard Granata. Relating Matrix Chemistry and Laser Fluorescence in Thermally Damaged Polymer Composites. ASME (IMECE). Lake Buena Vista, Florida, US2009.

[3.47] Wachter E. A., Fisher, W. G., Meyer, K. E. Laser Induced Fluorescence Imaging of Thermal Damage in Polymer Matrix Composites. Oak Ridge,TN: Oak Ridge National Laboratory; 1996.

[3.48] Kulowitch P., Scott, W. R. Detection of Thermal Damage in Epoxy-Based Composites Using Laser Pumped Fluorescence. Nondestr Charact Mater XI, Proc Int Symp, 11th. 2003:545-53.

[3.49] Lirong Bao, Albert F. Yee. Moisture diffusion and hygrothermal aging in bismaleimide matrix carbon fiber composites—part I: uni-weave composites. Composites Science and Technology. 2002;62:2099-110.

[3.50] P.K. Aditya, P.K. Sinha. Moisture Diffusion in Variously Shaped Fiber Reinforced Composites. Computers & Structures. 1996;59(1):157-66.

[3.51] JEREMY LEE TACK. THERMODYNAMIC AND MECHANICAL PROPERTIES OF EPON 862 WITH CURING AGENT DETDA BY MOLECULAR SIMULATION: Texas A&M University; 2006.

[3.52] Pavankiran Vaddadi, Toshio Nakamura, Raman P. Singh. Transient hygrothermal stresses in fiber reinforced composites: a heterogeneous characterization approach. composite, Part A. 2003;34:719-30.

[3.53] Suraj C. Zunjarrao, Raman P. Singh. Characterization of the fracture behavior of epoxy reinforced with nanometer and micrometer sized aluminum particles
Composites Science and Technology. 2006;66:2296–305.

[3.54] Vaddadi P, Nakamura T, Singh RP. Inverse analysis for transient moisture diffusion through fiber reinforced composites. Acta Mater 2003;51(1):177-93.

[3.55] Bhavesh GK, Singh RP, Nakamura T. Degradation of carbon fiber reinforced epoxy composites by ultraviolet radiation and condensation. J Compos Mater.

2001;2001(24):2713-33.

[3.56] Tsotsis TK, Weitsman Y. Energy release rates for cracks caused by moisture absorption in graphite/epoxy composites. J Compos Mater 1990;24:483-96.

[3.57] Raman P. Singh Suraj C. Zunjarrao. Characterization of the fracture behavior of epoxy reinforced with nanometer and micrometer sized aluminum particles
Composites Science and Technology. 2006;66:2296–305.

[3.58] Zhouhua Li, Xiaopeng Bi, John Lambros, Philippe H. Geubelle. Dynamic Fiber Debonding and Frictional Push-out in Model Composite Systems: Experimental Observations. Experimental Mechanics. 2002;42(3):417-25.

[3.59] Toren Watson. Flexural properties of Epon 862. Prairie View A&M University; 2007.

Chapter Four

Contact Mechanics Effects on AFAM Quantitative Measurements

Though there are many factors that would affect the accuracy in quantitative measurements by AFAM, the determination of probe geometry is believed to be one of the key ones. By taking the geometric wear during contact into account for quantitative determination, better mechanical properties were shown to be achieved. After a few measurements, the shape of AFM probes are often found not to follow the description by Hertzian and flat punch models, but closer to a body of revolution model geometry. The body of revolution models proposed in this study is shown to be less affected by the applied load than traditional Hertzian and flat punch models. Taking advantages of the reference materials with known bulk elastic modulus, the measurement of quantitative elastic modulus for epoxy can be better understood. Lead and Indium are chosen due to their closer modulus to epoxy than other candidates. An elastic-plastic contact study using Hertzian and body of revolution models is important for AFAM quantitative measurements that often requires high contact stresses. Due to the nature of epoxy inelastic properties, a visco-elastic model associated with time dependence is also investigated.

4.1. Introduction

Quantitative elastic modulus measurements on carbon fiber reinforced composite interphases is critical to understand the entire composites performance, and it needs the success of performing similar measurements on the epoxy matrix itself. Atomic force acoustic microscopy, that retains the same excellent lateral resolution of a scanning probe microscope, is a promising tool to achieve quantitative mechanical property measurements on less than a few microns interphase region [4.1-2]. The same high resolution AFAM nanomechanical measurements can be made on the epoxy bulk matrix region [4.2]. To achieve this, the contact mechanics of the probe-epoxy contact are essential for accurate quantitative determination, and important for further development of the AFAM technique.

The most common contact mechanics models that have been used in quantitative AFAM measurements are the Hertzian and flat punch models [4.3], which assume hemispherical and flat tip shapes, respectively. However, the two most common used models lack the flexibility of defining a realistic tip end shape, which may change over scanning and measuring cycles, and quantitative results based on them often varies over applied load[4.4-5]. Moreover, quantitative elastic modulus determination is primarily dependent on precise probe size and shape that are often characterized by the scanning electron microscope (SEM) and separate tip-reconstruction imaging experiments [4.6-7]. According to SEM images in this study, the body of revolution model in power law form is shown to have more flexibility in defining actual probe tip shape properly than when using Hertzian or flat punch models (see figure 4.1). The robustness of a chosen contact mechanics model over a range of applied loads is also essential for the application of a model to quantitative AFAM calculations. Addressed here are three different probe tip shapes (Sharp, Flat, and Rounded tips) which are used to study the effects of geometry and the choice of appropriate contact mechanics models used in AFAM analysis.

To achieve repeatable quantitative AFAM measurements, often higher static loads are applied [4.8] when compared to AFM topography modes of operation, and will result in a more severe tip variation upon usage. The SEM tip imaging prior and after any single measurement is critical to guarantee accurate quantitative outcome. The methodology of geometry shape and size determination is shown to be important whenever significant tip wear occurs. Consideration of real-time probe wear during contact measurements would be difficult to achieve, thus minimizing probe wear is critical to ensure the highest resolution in measurements. Therefore, a geometry model which more correctly captures the tip shape will be capable of measurements at low applied loads, and will result in less tip shape variations. Such improvements will push the resolution of quantitative AFAM measurement technique into finer regions.

Reference materials with already known elastic modulus can be used in AFAM quantitative elastic modulus determination to improve reliablilty and validate measurements [4.3]. Good reference candidates are expected to possess similar elastic modulus to the materials in need of being measured [4.9-10]. Lead and Indium with similar bulk elastic modulus to epoxy were tested for their qualification as reference materials. It has been shown that the Indium is a better reference material than Lead for surface testing exposure in ambient air conditions due to surface oxidation.

Due to the low yield stress of epoxy used in fiber reinforced composites, the high contact stresses found in AFAM quantitative testing can lead to plastic deformation at the tip-sample contact, which makes an elastic-plastic contact model necessary for accurate analysis of the mechanical response. Elastic-Plastic contact mechanics have been studied to understand the material response and pressure distribution [4.3, 11-13]. An extended elastic-plastic contact condition is introduced for each of the different probe profile models (Hertzian, body of revolution, and flat punch). Quantitative analysis using elastic-plastic contact is compared with results obtained from the probe geometry effect investigation.

Due to the visco-elastic nature of polymer materials, a visco-elastic model has been introduced into the AFAM quantitative calculations [4.14-16]. However, in the often required high applied load for quantitative AFAM implementation, the modeling of the visco-elastic contact should reflect the surface material response rather than taking it into account in vibration models. Numerous investigation on visco-elastic contact have achieved a good understanding of the material viscous, time-dependent response [4.17-18]. In this study, several visco-elastic models have been introduced. Due to the inability of capturing the contact resonance frequency in a precise time manner, the damping effects in the visco-elastic models can only be obtained based on approximations and can not be accurately obtained. Though, the characterized elastic response indicates that under the higher applied load, the visco-elasticity of the Epon 862 epoxy is not important for the quantitative elastic modulus measurements.

4.2. Elastic Contact Mechanics Principles and Models

4.2.1. AFAM Quantitative Elastic Analysis

The current contact mechanics development enables us to achieve quantitative elastic modulus analysis from contact stiffness measured from AFAM, and mostly based on probe geometry[4.19]. Among many others, Flat Punch and Hertzian Models are mostly employed in the contact mechanics studies (figure 4.2). A flat punch model represents the contact with a constant circular area throughout the indenter depth, and assumes the stiffness of the indenter is much greater than the tested sample surface. Such assumption holds when the silicon

AFAM probe is used to test soft metals and polymers. The flat punch model is a basic model form that had been and could be used to extend to other models. It is valid for both Hertzian and body of revolution models [4.20], and the relationship between contact stiffness, *k**, and elastic modulus, *E**, is proportional to the contact radius, by,

$$E^{*} = \frac{K^{*}}{(2a)} \tag{4.1}$$

Where, *a* represents the radius of the flat contact surface. The effective Young's Modulus of the tip-sample contact, *E**, is written as,

$$\frac{1}{E^{*}} = \frac{1-\nu_t}{E_t} + \frac{1-\nu_s}{E_s} \tag{4.2}$$

with E_t, ν_t representing the elastic modulus and Possion ratio for the AFM tip material, and for tested materials, the subscript *s* is used.

In the three dimensional Hertzian analysis [4.3] the contact is assumed to be a parabolic indenter in contact with a flat surface. From such assumption, the radius of contact area, a, as function of applied load and sample surface elastic modulus is,

$$a_H = \sqrt[3]{\frac{3F_c R}{4E^{*}}} \tag{4.3}$$

where *R* is the radius of curvature of the indenter tip, and *E** is the effective elastic modulus.

However, from the previous study[4.5], neither the Hertzian or Flat punch model is found to be a good contact mechanics model to execute accurate quantitative calculation from contact stiffness. Most importantly, both of the models exhibit a high sensitivity over applied load in quantitative measuring, and often requires high loads to reach the results that retain consistency over the applied loads. Therefore, a good contact mechanics model that can lead to accurate quantitative analysis, with an exhibited ability of being less affected by applied load is in need to achieve reliable quantitative modulus determination. In this study that involves single point contact without scanning over surfaces. The AFAM probe profile is neither found to follow a round or flat geometry, which indicates that the Hertzian and flat punch models may lack the ability of physically describing the precise contact condition.

The body of revolution model physically represents a conformal type of indenter in contact with a tested sample. It can potentially describe any contact surface profile if the symmetric revolution along the indenter depth is satisfied. This model is derived from the classical non-Hertizian conformal surface contact relationship [4.3]. As observed from SEM images, the profile of the probe end can be approximated by a type of power law,

$$h = \frac{1}{(2R)^{2n-1}} \cdot x^{2n} \quad , \quad \text{where} \quad \mathrm{n} \in (1,2 \cdots \mathrm{n}) \tag{4.4}$$

Where, the *h* and *x* indicate the depth and positions in horizontal axis of tip end surface. Here, *R* is a parameter introduced as nominal curvature to define tip surface profile in this study.

In the axi-symmetric case Steuermann found the relation between applied normal load and reduced Young's Modulus as [4.21]

$$F_n = \frac{4A_n E^* n \cdot a^{(2n+1)}}{(2n+1)} \cdot \frac{2 \cdot 4 \cdots 2n}{1 \cdot 3 \cdots (2n-1)} \tag{4.5}$$

Where, F_n represents a reduced applied normal load, and in assumed body revolution model condition,

$$A_n = \frac{1}{(2R)^{2n-1}} \tag{4.6}$$

Substituting the radius of the contact area into Eqn (4.5), it yields,

$$F_n = \frac{4E^* n \cdot a^{(2n+1)}}{(2n+1) \cdot (2R)^{2n-1}} \cdot \frac{2 \cdot 4 \cdots 2n}{1 \cdot 3 \cdots (2n-1)} \tag{4.7}$$

In Figure 4.3, the body revolution model with n=1,2,3,4 cases are shown to comparison with Hertzian and flat punch model profile curves. Since the n=1 case for a body of revolution model lies outside of the range between Hertzian and flat punch models, the two extreme cases, it indicates n=1 might not be the one to improve the modeling. Taking into account the decrease of variations between curves from two adjacent order numbers as the order increases, this study will use n=2 and 3 particular cases to compare with Hertzian and flat punch models, in an effort of developing a robust geometric model for AFAM contact mechanics analysis. If one applies n=2, 3 to Eqn (4.5)

$$F_n = \frac{8}{15} \cdot \frac{E^* a^5}{R^3} \quad , \quad for\ \mathrm{n} = 2 \tag{4.8}$$

$$F_n = \frac{6}{35} \cdot \frac{E^* a^7}{R^5} \quad , \quad for\ \mathrm{n} = 3 \tag{4.9}$$

Combining (4.7) and (4.8~9), the E^* can be related to the applied load as,

$$E^* = \sqrt[4]{\frac{1}{60} \cdot \frac{k^{*5}}{R^3 F_n}} \quad , \quad for\ \mathrm{n} = 2 \tag{4.10}$$

$$E^* = \frac{1}{2} \cdot \sqrt[6]{\frac{3}{35} \cdot \frac{k^{*7}}{R^5 F_n}} \quad , \quad for\ \mathrm{n} = 3 \tag{4.11}$$

This analytical solution derived from the proposed body of revolution model extends the contact mechanics ability rather than simply assuming the indenter to be either perfect round or flat. To note, its profile parameters determination shall also rely on the probe end SEM images. It is critical to point out here the imaging ability of the probe end profile is critical to the improvements or selection of applied contact mechanics theories. Another very important advantage by selecting the body of revolution model, among many others, is for its single parameter controlled function, which is expected to retain the simplicity of the Hertzian and flat punch models and allow extension to the study of elastic-plastic contact analysis. It is often recommended to image the probe with different views to construct the precise 3D probe, though in this study, most of the observations are based on a single SEM measurement.

4.2.2 Probe Geometry Effects on Quantitative Results

An efficient way to ascertain the applicability of these contact mechanics models, is to perform AFAM tests with different probe shapes on the same materials and compare these models by quantitative results. Lead and Indium as references materials will be applied with the same conditions as to epoxy. The AFM polysilicon (E_{Si} = 169 GPa, v = 0.33) cantilevers with similar spring constant (k_c = 18 – 28 N/m, determined by the thermal tuning method), but with distinctly different probe end geometries were used to perform quantitative measurements on Lead, Indium and Epon 862 epoxy. The probe set included 2 sharp probes (Radius, R ~ 20 nm), one small flat probe (a ~ 30 nm), one large flat probe (a ~ 200 nm), and one round probe with a large radius curvature (R ~ 100 nm). The probe geometry was measured before and after the testing quantitatively by SEM. The known material properties of Lead (E_{Pb} = 14 GPa, v = 0.42), Indium (E_{In} = 11 GPa, v = 0.45), and the epoxy (E = 3 - 5 GPa, v= 0.3) are used to compare with the contact models. In the experiment, each probe measures all three materials, in the sequence of Indium, Lead, and then epoxy, to a maximum load of 5 µN. The probe micrographs are analyzed by digital imaging software, and *4th* and *6th* order power law curves are fit through a MATLAB curve fitting tool box to determine the radii of curvature.

It has been shown in chapter 2 that contact stiffness is the key to achieve quantitative elastic modulus measurement, and needs to be carried out first. In this section, the contact stiffness calculation method was kept unchanged, and is calculated based on Eqn 2.1. By doing so, the contact stiffness with respect to spring constants of each cantilever were depicted in Figure 4.4 (a-e) under applied load variations. It is observed that the contact stiffness increases as the applied load increased, and the trend of the increase is less aggressive for higher load conditions. Physically, no matter the tip geometry, the larger the contact area, the higher the contact stiffness. Significant probe geometry changes during measurement can be obtained from the jumps in the contact stiffness curves over a load range. Since the change in probe profile very often relates to tip wear, this corresponds to an increase in contact area.

The probe fracture wear is consistently observed in all of the AFAM testing with only a few N of applied load (Figure 4.4). The sharp corners of the probe end tend to become blunted (or at least with one corner round if it has more than one) when used during AFAM measurement. It has been found that after several measurements, the profile towards the center of the probe tends to be more flat. These two features of the AFAM probes during contact measurements makes the body of revolution model, which can represent a blunted curved tip, a good fit compared to the other models. In other words, the large round geometry probe has less variation in geometry and would be likely to keep the round shape throughout the measurements, which may benefit and minimize the post analysis work. However, the flat tip end is easier to wear out at the sharp corner(s), thus, rounding the probe profile and making the quantitative measurement difficult due to the varying geometry and hence contact area. This is especially an issue on the tests that were performed prior to significant geometry change, thus giving erroneous results when the contact mecahanics are analyzed. Moreover, if the profile is round before performing measurements, less tip wear is often observed in those measurements as the stress concentration is naturally lower due to a distributed stress within the contact area. Among the round type tips, fresh tips are observed to have larger variation in geometry during measurement, as the same applied load will result in a larger contact stress that can initiate fractures of the probe tip. By considering the limitation of the SEM characterization employed in this study (~10 nm), geometry determinations for sharp probes are difficult to be realized accurate, implying the usage of fresh tips will potentially provide larger measurement errors in quantitative measurements.

Although the proposed body of revolution model would define a tip geometry profile closer to the actual geometry, the real probe geometry will never be exact using this methodology. Therefore, an approximation of the geometry for the body of revolution model with acceptable errors is desirable, The probe end was approximated to find the best nominal radius of curvature for the body of revolution model by using a curve fitting tool box in Matlab. The tool box was found to provide a good approximation for the more blunted probes, but not the fresh (sharp) probes. The AFM probes with a larger radius of curvature were preferable for determining probe geometry accurately using this method. In addition, the high susceptibility of sharp probes to fracture and blunt when applying similar levels of load introduces large potential error in the measurements. Depending on the microscopy resolution (e.g. SEM, TEM), the accuracy of probe measurements may vary. To avoid severe fracture, probes with radius of curvature larger than 30 nm result in a greater resistance to wear for applied loads up to several microNewtons.

The elastic modulus of Lead, Indium and epoxy are derived based on contact stiffness results by Hertzian, flat punch and body of revolution contact mechanics models, as shown in Figure 4.4 (a-c). The power law body of revolution model exhibits less variation over applied load compared to the Hertzian and flat punch models. Figures 4.6-4.8 show that the body of revolution model lies between the Hertzian and flat punch models. The fact that the models present good agreement for higher loads is due to the the Hertzian and flat punch models capturing the actual large scale probe geometry accurately. The body of revolution model shows consistent modulus even at small loads, indicating the model’s ability to accurately represent the probe geometry at multiple scales. This unique ability of the body of revolution model allows the quantitative modulus measurement to be acquired for smaller loads, and hence smaller material volumes. The improvement will allow the AFAM technique to be used at lower loads leading to a decrese in tip geometry variation and wear and correspondingly less error in the quantitative analysis. It is also worth noting that the flat punch model shows a more consistent quantitative measurement than the Hertzian model for the applied load range. Most importantly, as the round probe geometry is found to be the trend for all types of probes after one or few contact measurements, the flat punch model that is not able to be parameterized for rounded shape probes, proves to be insurfficent for quantitative analysis.

If the large round probe is considered, the effect of the tip geometry change for the measured sample is shown in Figure 4.9. This analysis characterizes the quantitative elastic modulus with a geometry condition before and after AFAM measurement, instead of using one single geometry throughout the measurement analysis. As the load increased, the tip geometry change during the AFAM measurement is identified by the abrupt change in the elastic modulus. Quantitative results before the probe geometry change in epoxy (curve jump in contact stiffness) is characterized by the initial probe geometry before measurement. The quantitative analysis for epoxy after the significant geometry variation occurred using the post-fracture geometry is found more reasonable for quantitative purposes. There is a good agreement before and after the tip geometry transition in the quantitative measurement. The quantitative elastic modulus difference between Indium and epoxy is also closer to true values while the Indium analysis is based on the pre-fracture geometry. The geometry change is compared and presented by the body of revolution model through the curve fitting in Figure 4.10. This captured fracture results in a probe geometry variation of about 5% after a series of AFAM measurements had been performed: one series of measurements on each Indium, Lead and epoxy with applied loads smaller than 3μN.

The quantitative elastic modulus computed from AFAM by the contact stiffness analysis are within the same order of the measured bulk modulus, however, most are not within 10% of agreement. Another nominal curvature $R^{'}$ is proposed to describe the geometry expected from the AFAM measurement to achieve the desired bulk elastic modulus. Here, by assuming the epoxy has elastic modulus of 5 GPa, a parameter *N* is used to define the difference between the SEM measured R and $R^{'}$

$R^{'} = N \cdot R$ (13)

$R^{'}$ and $a^{'}$ are introduced to implement the body of revolution and flat punch models, respectively. Utilizing the new radius of curvature, Lead and Indium results are compared with their already known bulk modulus values. In addition, the results show a good agreement between the three different contact mechanics models [Figure 4.11-12]. Quantitative Indium elastic modulus obtained by this method (~9-10 GPa), compares with the bulk value (11 GPa). This implies that the Indium is obeying similar contact mechanics response, and may be a good reference material for the epoxy.

The Lead sample should exhibit a larger bulk modulus than Indium, however, the surface elastic modulus of the Indium sample is consistently found larger than Lead. EDX was used in conjunction with SEM to examine the elemental composition of the Lead and Indium surfaces. From Figure 4.13, the surface of Indium is shown to be relatively pure, while the Lead surface was been found to contain oxygen and carbon that may identify the existence of Plumbate [4.22] on the surface, which usually forms as lead is exposed to air and moisture. The impure and chemically altered lead surface affects the contact mechanical response; and thus affects the quantitative AFAM measurement analysis. Therefore Lead, with an unknown surface elastic modulus, is not qualified for this quantitative study, leaving the Indium as the reference used for epoxy AFAM quantitative measurements.

The three contact mechanics models studied in this work followed the general trend depicted in Figure 4.14, which represents the effect of probe tip geometry on computed elastic modulus for the same contact stiffness. Results validated that the body of revolution model was suitable for AFAM quantitative contact mechanics analysis.

4.2.3 Summary of the Elastic Contact Models

The power law shaped body of revolution model is shown to have a good approximation of the real probe end geometry, and is best described as a rounded punch or severely blunted spherical tip. Experiments showed that the probes which began with a large, flat end tended to become rounded after measurements. Likewise, new AFM tips were found to blunt after usage. The geometry variation from before and after AFAM measurements affects the quantitative results. Elastic modulus values are calculated for the measured contact stiffness using Eqns. (4.11) and (4.12). The location of the probe geometry change can be determined from the contact stiffness and calculated elastic modulus values. The moment when significant probe geometry change occurs can be observed in Figure 4.9 (indicated by arrow) and is believed to be caused by tip fracture. Since the measured contact stiffness increases for an increase in contact area, the elastic modulus is overestimated since the model utilizes a smaller radius of curvature. Calculation of the elastic modulus with the before and after geometries leads to a shift in the result curves shown in Figure 4.9. Since the Indium was measured prior to the fracture event, it is best represented by the before geometry, where modulus values are found to be larger and consistent with expected values (~10 GPa). The epoxy is best represented by the post measurement geometry for values after the fracture event, leading to an elastic modulus value of ~5 GPa at higher loads, which is consistent with measured bulk values. Prior to the fracture event, epoxy modulus values when analyzed with the pre-fracture geometry are more appropriate, where it is interesting to note that values before and after the fracture event are nearly continuous when analyzed with the pre- and post-fracture geometries, respectively. The geometry change is captured and taken into account into analyzing the quantitative elastic modulus, and its results are shown to be much more acceptable. For the entire load range, the elastic modulus is expected to remain constant, and the body of revolution model provides a more consistent quantitative elastic modulus result than the Hertzian and flat punch models. Lead results are not presented since EDX analysis observed chemical contamination to the surface observed in the SEM.

Contact stiffness increases as the applied load increased, and the trend of the increase is less aggressive for higher loads. Probe tip wear were found always to round-off the probe profiles. A power law body of revolution model exhibits less variation over applied load compared to Hertzian and Flat punch models. The fresh tip is more difficult to be measured accurately due to its sharpness, and for the same load, if the probe profile is initially round, the larger the radius of curvature is, the less of the percentage of variation will be for the probe.. Indium may be a good reference material for AFAM measurements of polymers and epoxy.

4.3. Elastic-Plastic Contact Effects on AFAM Analysis

In contact mechanics, the high applied load often needed in determination of quantitative mechanical properties, will introduce the plastic deformation into the contact surfaces [4.11], but the elasticity of materials still plays an important role in the plastic indentation. When the yield point is first exceeded, the plastic zone is limited and fully contained by materials that retain elastic characteristics, making the plastic strains within the same order of magnitude as the surrounding elastic strain [4.3, 23-25]. In such a situation there is a need for an elastic-plastic response mechanism. Though some efforts have been made on numerical elastic-plastic simulation[4.13], the analytical solution in the form of elastic-plastic contact condition is more effective to quantitative analysis, and would potentially explain the contact stiffness found from AFAM.

The simplest model for elastic-plastic contact is the cone indenter in contact with an impressible infinite half space [Figure 4.15]. K.L.Johnson had concluded hydrostatic component expression followed the relation as, [4.3],

$$\frac{\bar{p}}{Y} = \frac{2}{3}\left\{1 + \ln\left(\frac{1}{3}\frac{E^*}{Y}\tan\beta\right)\right\} - 0.19 \tag{4.12}$$

Where E^* is the effective modulus of the contact, Y is the strength of the indented material, $\bar{p}$ denotes the hydrostatic component of stress in the core contact region and has a relation to the mean pressure as,

$$p_m = \bar{p} + \frac{2}{3}Y$$

Where, the mean pressure can be expressed in terms of applied load by

$$p_m = \frac{P}{\pi a^2}$$

Therefore, the elastic-plastic contact can be rewritten as,

$$P = Y\pi a^2 \left\{ 1.143 + \frac{2}{3}\ln\left(\frac{1}{3}\frac{E^*}{Y}\tan\beta\right) \right\} \tag{4.13}$$

In this relation, β is the key parameter that will vary with different indenter shapes in contact and will be affected by the contact theories. In the following sections, based on the elastic modulus conclusion that had been achieved previously in section 4.3, the sphere and power law body of revolution shapes will be considered for elastic-plastic contact.

4.3.1. Elastic-plastic model for spherical contact

Consistent with the Hertzian contact model that describes the spherical contact relation for elastic deformation, the same contact type is needed to be analyzed to achieve understanding of the quantitative determination by a spherical AFM probe. Efforts have been made to understand such contact condition [4.26], and here development of a quantitative relation is presented that will benefit the AFAM quantitative elastic modulus measurement.

Assuming, $a^2 = 2R\delta$

(4.14)

For the elastic-plastic contact, the β follows,

$$\tan\beta = \frac{\delta}{a} = \frac{a}{2R}$$

Replacing the β in the Eqn 4.13, we have

$$P = Y\pi a^2 \left\{ 1.143 + \frac{2}{3}\ln(\frac{1}{6}\frac{E^* a}{YR}) \right\} \tag{4.15}$$

It can be rewritten as,

$$P = 2Y\pi R\delta \left\{ 1.143 + \frac{2}{3}\ln(\frac{E^* \cdot 2^{1/2} \cdot \delta^{1/2}}{6Y \cdot R^{1/2}}) \right\} \tag{4.16}$$

Then, the contact stiffness yields

$$k* = \frac{dP}{d\delta} = 2Y\pi R \left\{ 1.476 + \frac{2}{3}\ln(\frac{1}{6}\frac{E^* a}{YR}) \right\} \tag{4.17}$$

Thus,

$$a = \frac{6YR}{E^*} \cdot \exp\left\{ \frac{3}{4}(\frac{k*}{Y\pi R} - 2.9527) \right\} \tag{4.18}$$

Substituting the a into Eqn 4.15 yields,

$$E^* = 6YR\sqrt{\frac{(\frac{k^*}{2R} - \frac{Y\pi}{3})}{P}} \cdot \exp\left\{ \frac{3}{4}(\frac{k*}{Y\pi R} - 2.9527) \right\} \tag{4.19}$$

Conducting quantitative analysis by this relation, E^* is found to be a unreasonable value larger than the purely elastic contact. The reason for this, as former motioned, is due to a more blunt probe geometry is in used, and the measurement based on it to obtain sphere parameter for the contact model. This reality implies the real contact radius correspondent to spherical contact model shall be larger than the real measured probe dimension, which is the arc length only occupied a small portion of the large sphere profile. By giving the probe radii a larger value, 1 μm, the elastic modulus calculated from the measured contact stiffness shows a better agreement with the bulk modulus of epoxy, for both the elastic and elastic-plastic spherical analysis (figure 4.19). Therefore, with a different probe geometry shape than the sphere, for accurate quantitative determination purpose, one should always be careful for the radii implemented in spherical contact analysis, e.g. the true radii can be determined from reference materials.

4.3.2. Elastic-plastic model for power law body of revolution contact

The power law body of revolution model has been successfully introduced to quantitative determine for the elastic modulus in the earlyier part of this chapter. Here, a power law geometry is extended to the elastic-plastic core model, and the relationship between contact stiffness and the reduced elastic modulus is derived.

Recall the definition of the power law body of revolution model profile definition,

$$h = \frac{1}{(2R)^{(2n-1)}} x^{2n} \tag{4.21}$$

Here R is the nominal radius curvature that needs to fit the profile curve measured from the probe.

Following the same assumption, $a^2 = 2R\delta$, yields,

$$\delta = \frac{1}{(2R)^{(2n-1)}} a^{2n} \tag{4.22}$$

Thus the β follows,

$$\tan\beta = \frac{\delta}{a} = \frac{1}{(2R)^{(2n-1)}} a^{(2n-1)}$$

Replacing the β in Eqn (4.13) yields,

$$P = Y\pi a^2 \left\{ 1.143 + \frac{2}{3} \ln\left(\frac{1}{3} \frac{E^* a^{(2n-1)}}{Y (2R)^{(2n-1)}}\right) \right\} \tag{4.23}$$

It can be reorganized as,

$$P = Y\pi \cdot \delta^{\frac{1}{n}} \cdot (2R)^{(2-\frac{1}{n})} \left\{ 1.143 + \frac{2}{3} \ln\left(\frac{1}{3} \frac{E^*}{Y} (2R)^{(\frac{1}{2n}-1)} \delta^{(1-\frac{1}{2n})}\right) \right\} \tag{4.24}$$

Thus, the contact stiffness follows,

$$k^* = \frac{dP}{d\delta} = Y\pi \cdot \delta^{(-1+\frac{1}{n})} \cdot (2R)^{(2-\frac{1}{n})} \left\{ \frac{2}{3n} \ln\left(\frac{1}{3} \frac{E^* \delta}{Ya}\right) + 0.81 \frac{1}{n} + \frac{2}{3} \right\} \tag{4.25}$$

$$k^* = Y\pi \cdot (2R)^{(2n-1)} \cdot a^{(2-2n)} \left\{ \frac{2}{3n} \ln\left[\frac{1}{3} \frac{E^*}{Y} \left(\frac{a}{2R} \right)^{(2n-1)} \right] + 0.81 \frac{1}{n} + \frac{2}{3} \right\} \tag{4.26}$$

From the Eqn (4.26), we have,

$$E^* = 3Y\left(\frac{2R}{a}\right)^{(2n-1)} \cdot \exp\left[\frac{3n}{2}\left(\frac{k^*}{Y\pi\cdot(2R)^{(2n-1)}\cdot a^{(2-2n)}} - 0.81\frac{1}{n} - \frac{2}{3}\right)\right] \tag{4.27}$$

Substitue Eqn (4.27) back to (4.23), yields

$$P = Y\pi a^2\left\{\frac{1}{3} - \frac{2}{3n} + \frac{nk^*}{Y\pi(2R)^{(2n-1)}a^{(2-2n)}})\right\} \tag{4.28}$$

The radius a in equation 4.28 can be analytically solved, however when n>3, this will result in solving a higher order (n>3) algebraic equation. This will not only add to the calculation difficulty, but also increase the error in the calculation. Since the calculation is based on experimentally measured parameters, where measuring errors are inevitable, the involvement of a higher order calculation will amplify these errors and decrease the stability of the theory. Thus, in this section, only the n=2 and 3 cases are going to be discussed, and n=2 is used for model validation.

When n=2, Eqn (4.28) yields,

$$P = -Y\pi a^2 + \frac{2k^*}{(2R)^{(3)}}a^4 \tag{4.29}$$

and when n=3, Eqn (4.28) yields,

$$P = \frac{7}{3}Y\pi a^2 + \frac{3k^*}{(2R)^5}a^6 \tag{4.30}$$

Real positive solutions for Eqn (4.29) and Eqn (4.30) are

For n=2 $$a=\left\{\frac{(2R)^3Y\pi+\sqrt{[(2R)^3Y\pi]^2+8P\cdot(2R)^3}}{4k*}\right\}^{1/2} \tag{4.31}$$

For n=3 $$a=\left\{\left[\frac{P\cdot(2R)^5}{6k*}\right]-\left[\left(\frac{P\cdot(2R)^5}{6k*}\right)^2+\left(\frac{7Y\pi\cdot(2R)^5}{27k*}\right)^3\right]^{1/2}\right\}^{1/3}$$

$$+\left\{\left[\frac{P\cdot(2R)^5}{6k*}\right]+\left[\left(\frac{P\cdot(2R)^5}{6k*}\right)^2+\left(\frac{7Y\pi\cdot(2R)^5}{27k*}\right)^3\right]^{1/2}\right\}^{1/3} \tag{4.32}$$

Eqns. (4.31) and (4.32) are substituted into Equation (4.27), which for n=2, 3 are in the form of,

For n=2 $$E^*=3Y\left(\frac{2R}{a}\right)^3\cdot\exp\left[3\cdot\left(\frac{k*\cdot a^2}{Y\pi(2R)^3}-0.405-\frac{2}{3}\right)\right] \tag{4.33a}$$

For n=3 $$E^*=3Y\left(\frac{2R}{a}\right)^5\cdot\exp\left[\frac{15}{2}\cdot\left(\frac{k*\cdot a^4}{Y\pi(2R)^5}-0.27-\frac{2}{3}\right)\right] \tag{4.33b}$$

As the effective modulus of the contact is obtained, the elastic modulus of the substrate (tested) material can also be determined using Eqn. (4.2).

4.3.3. Elastic-plastic model with a general contact stiffness

The elastic Hertzian and flat punch models follow the same relationship between contact stiffnes, reduced modulus, and contact area. Here, the general relationship for elastic contact stiffness is utilized with the elastic-plastic core model..

Recall the assumption

$a^2 = 2R\delta$

Thus $\tan\beta = \frac{\delta}{a} = \frac{a}{2R}$

Replacing the β yields,

$$P = Y\pi a^2 \left\{ 1.143 + \frac{2}{3}\ln\left(\frac{1}{6}\frac{E^* a}{YR}\right) \right\} \tag{4.34}$$

Since it follows $E^* = \frac{k^*}{2a}$, the relation can be rewritten as,

$$P = Y\pi\left(\frac{k^*}{2E^*}\right)^2 \cdot \left\{ 1.143 + \frac{2}{3}\ln\left(\frac{1}{12}\frac{k^*}{YR}\right) \right\} \tag{4.35}$$

Analytically, one can solve Eqn (4.35) as,

$$E^* = \sqrt{\frac{Y\pi}{P}\left(\frac{k^*}{2}\right)^2 \cdot \left\{ 1.143 + \frac{2}{3}\ln\left(\frac{1}{12}\frac{k^*}{YR}\right) \right\}} \tag{4.36}$$

Though the $E^* = \frac{k^*}{2a}$ is assumed, the numerical results obtained exhibited solutions closer to the bulk modulus of measured epoxy..

4.3.4. Elastic-plastic contact results

From figures 4.18, 4.19, 4.21, and 4.23, it is evident that the use of elastic-plastic spherical contact analysis can result in a more accurate prediction of epoxy elastic modulus usin AFAM than the elastic Hertzian analysis. The tip geometry effect is the primary contribution to the variation of quantitative modulus determination at low applied loads. Elastic modulus is predicted more accurately due to the consideration of the plastic contact strains at higher loads; though at lower loads the geometry effect is dominate. For a sharp AFM probe, the effect of the elastic-plastic contact occurs at lower loads (Figure 4.21), due to the smaller radius of curvature resulting in an earlier onset of plastic contact Over a wider load range elastic-plastic analysis provides consistent modulus determinations, similar to the tip geometry effect, where both effects are on a similar order for elastic modulus characterization. The elastic-plastic spherical contact utilizing the general contact stiffness relationship was consistently found to improve the results from the elastic spherical analysis (Figures 4.18 and 4.21). The results from the power law shaped geometry (with n = 2) were found to improve the calculated elastic modulus at higher loads for the round probe (Figure 4.20), though at lower loads showed a large variation. This is believed to be due to the inaccuracy in the geometry causing errors at low applied loads. Since the elastic analysis demonstrates that at low loads, the geometry is not sufficiently characterized due to the large modulus determined (resulting due to a smaller contact area predicted using the model than actual), the elastic-plastic analysis will have similar effects. Though, the elastic-plastic analysis shows the opposite trend, with lower values of elastic modulus calculated from the model at low loads, and increasing with load. This is due to the smaller geometry than actual in the model increasing the plastic strain which increases the contact area. The larger contact area then results in a reduction in the computed elastic modulus at the low loads. The values increase as the geometry is more accurately taken into consideration, thus reducing the plastic strain and the contact area. When comparing the three probe geometries (Figures, 4.20, 4.22, and 4.23) similar trends are observed. For the sharp AFM probe, the results present a large slope that increases through the loading range, and crosses the elastic result curve. The inability for the power law elastic-plastic model to provide consistent results is due to an under estimation of the contact area by the model as loads increase. This may be due to the inability of the plastic core model to accurately predict results of high plastic strains that would occur at the edges of a sharp power law indenter, which will induce higher contact stresses than the round and flat probes.

4.4. Visco-Elastic Contact Effects on AFAM Analysis

AFAM quantitative analysis is simplified by using linear models for the material response, though when testing polymeric materials that exhibit visco-elastic properties, non-linear effects may need to be considered. The characterization of visco-elastic properties of epoxy is critical to understand the materials behavior in for applications and is typically measured by techniques such as dynamic mechanical analysis (DMA). However, the AFAM quantitative measurement without the ability to measure contact resonance frequency over time, will not enable the visco-elastic property measurement. The elastic response of epoxy in the context of a visco-elastic material model can be calculated using AFAM and will be discussed here. To study these material characteristics that occur at the time scale of the load application is essential, as the AFAM phase imaging mode is performed in a similar manner while it continuously rasters a sample surface. Single point AFAM testing can be performed immediately after a load is applied or after a timer duration when the material response has stabilized, e.g. a visco-elastic material.

Before the introduction of the visco-elastic models, in the effects of time dependent loading on AFAM single point quantitative measurements will be discussed. After the probe lands on the sample surface with a predefined contact load (σ_1), a higher load is applied (σ_2) as shown in figure 4.24. The load application can be represented by the Heaviside step function. The stress condition remains constant if the material creep or visco-elastic response is not severe, leading to a constant contact area over time by the same applied load.

With creep or a visco-elastic material response, the boundary conditions encountered with the growth of the AFAM probe contact area will cause the contact resonance frequency correspondingly to increase. A shift in the contact resonance frequency was observed from contact at an initial time versus after 30 seconds of contact for an applied load of 1.68 μN (Figure 4.26). The shift was was due to the visco-elastic characteristics of the tested polymer epoxy.

In order to study the materials, several existing visco-elastic models have been reviewed. The Kelvin-Voigh [4.27] and Maxwell [4.27] models are two of the simplest models that can represent the viscoelasticity of a material. Application of these two models to AFAM is limited, since the Kelvin-Voight model is unable to respond at the instant of load application; and the Maxwell model creates and endless creep response. The Standard Linear Solid [4.27] and Delayed Elasticity

[4.3] models are capable of characterizing the contact at two critical moments for AFAM, the point of initial applied load and the equilibrium response of the material.

Analytical solutions to the Maxwell and Kelvin-Voigt boundary conditions [4.14, 28] have been applied to acoustic micrscopy, as well as numerical solutions for the conditions including the Standard Linear Solid Model, the Delayed Elasticity Model, and Maxwell–Weichert contact conditions [4.15-16, 29-30]. However, the AFAM technique is performed by insonifying the sample mounted on an ultrasonic transducer that emits longitudinal acoustic waves with very sample amplitudes of vibration. In AFAM, the vibration amplitude is negligible compared with the cantilever deflection that accounts for the load application in contact (Figure 4.27). Thus, the viscoelastic response from the materials is the major contribution to the AFAM quantitative determination of polymer materials.

It is unrealistic for AFAM devices to capture the resonance frequency response as a function of precise, but approximate time manner; this is due to the nature that some amount of time is needed to acquire the frequency spectrum in each measurement. However, several resonance frequency spectrums were obtained by manual timing and used to analyze the visoelastic response of the epoxy. Due to the short viscoelastic material time constant in the AFM probe contact combined with the delay in obtaining AFAM spectrum, determination of the damping coefficients in the material models is not performed. The elastic characteristics that govern the material behavior were demonstrated to be able to be obtained from AFAM measurements.

a) Delayed Elasticity Model

Following the relation of $\sigma = E\varepsilon$ and $\sigma = \eta \frac{d\varepsilon}{dt}$, where is the applied stress, *E* the Hookean elastic coefficient, the resulting strain, the viscous coefficient, and *t* is the elapsed time, the constitutive relationship for the delayed Elasticity model [4.3] as,

$$\varepsilon = \left[\frac{1}{E_1} + \frac{1}{E_2}\left(1 - \exp\left(-t/T\right)\right) \right] \sigma \tag{4.37}$$

Where $T = \eta / 2E_2$

At $t \approx 0$, the constitutive relation in Eqn (4.37) reduces to

$$\sigma = E_1 \varepsilon \tag{4.38}$$

For the spherical probe, from the Hertzian contact stiffness relationship,

$$k^* = \sqrt[3]{6E_1^{*2}RP} \tag{4.39}$$

where P is the applied normal load and R is the radius of curvature.

At $t = t_s$, the viscous dissipation is taken as $\exp(-t/T) \approx 0$, since the contact takes a long time duration to reach a stabilization point, thus the constitutive relation becomes,

$$\sigma = \left[\frac{E_1E_2}{E_1 + E_2}\right]\varepsilon \tag{4.40}$$

If one simply replaces the constitutive relation into the Hertzian contact equation of,

$$a = \left(\frac{3PR}{4E}\right)^{1/3} \tag{4.41}$$

then,
$$a = \left(\frac{3PR}{4}\frac{E_1 + E_2}{E_1E_2}\right)^{1/3} \tag{4.42}$$

Following the definition of the contact stiffness,

$$k^* = \frac{dP}{d\delta} = \sqrt[3]{6\left(\frac{E_1E_2}{E_1 + E_2}\right)^2 RP} \tag{4.43}$$

Due to resonance frequency increase in the AFAM contact over time, the k^* is expected to be larger at the stabilization point than at the initial applied load. This conclusion does not correspond with Eqn (4.39) and Eqn (4.43), where $\frac{E_1E_2}{E_1 + E_2} \le E_2$, unless either of E_1 and E_2 is negative. Though, the fact that the

AFAM probe in contact before stabilization with a certain holding applied load would continue indenting the material further and correspondingly increase the contact area can not be neglected [4.3, 31-33]. It has been calcualted that the delayed material response mechanism would result in as much as more than 20% contact radius increase than the Hertzian model predicts [4.3] (in some studies, a conversion to the contact area is needed if incensement is expressed by the indentation depth [4.34]). Since most of the increase occurred before reaching the stabilization point, if 20% contact area increase considered, it is admissible to adopt the factor of 1.2 into the existing equation

$$k^* = \frac{dP}{d\delta} = (1.2)\cdot\sqrt[3]{6\left(\frac{E_1 E_2}{E_1 + E_2}\right)^2 RP} \tag{4.44}$$

In doing so, the contact model of the delayed elasticity materials for AFAM quantitative contact determination is achieved. To note, even though the E_1 and E_2 are two separate values, in evaluation of the stabilized state materials response, the effective modulus $E^* = \frac{E_1 E_2}{E_1 + E_2}$ represents the detected materials mechanical response ability.

b) Standard Linear Solid Model (Stress Relaxation)

Referring to the standard linear solid model in Figure 4.28, its constitutive relationship is summarized as [4.27],

$$\frac{d\varepsilon}{dt}=\frac{\frac{E_2}{\eta}\left(\frac{\eta}{E_2}\frac{d\sigma}{dt}+\sigma-E_1\varepsilon\right)}{E_1+E_2} \tag{4.45}$$

Similar to what has been described in the Delayed Elasticity model, in the Standard Linear Solid model, at $t\approx 0$, it has,

$$\frac{d\sigma}{dt}=\infty$$

Referring back to Eqn (4.45), it also must have,

$$\frac{d\varepsilon}{dt}=\infty$$

Ignoring higher order terms, it yields,

$$(E_1+E_2)\frac{d\varepsilon}{dt}=\frac{d\sigma}{dt} \tag{4.46}$$

Which has a solution that corresponds to the constitutive relation,

$$\sigma=(E_1+E_2)\varepsilon+C \tag{4.47}$$

Similarly this constitutive relation can be introduced into the Hertzian analysis,

$$k^*=\sqrt[3]{6(E_1+E_2)^2RP} \tag{4.48}$$

Considering the constitutive relation for Standard Linear Solid model at $t=t_v$, it has $\frac{d\sigma}{dt}=0$, thus leaving,

$$\left(E_1+E_2\right)\frac{d\varepsilon}{dt}+\frac{E_1E_2}{\eta}\varepsilon=\frac{E_2}{\eta}\sigma \tag{4.49}$$

This ordinary differential equation can have a solution of the form,

$$\varepsilon = \frac{1}{E_1}\sigma + C \tag{4.50}$$

Where $C$is a constant.

Introducing the constitutive relation into the Hertzian analysis, the contact stiffness is then obtained,

$$k^* = \sqrt[3]{6E_1^{*2}RP} \tag{4.51}$$

For consistency, 20% contact area increase is also considered in this model, and it leads to,

$$k^* = 1.2 \cdot \sqrt[3]{6E_1^{*2}RP} \tag{4.52}$$

It can be concluded from the results (figure 4.28) that the major material properties from different visco-elastic models are not so different from the Hertzian elastic analysis. Similar conclusion has been made by other researchers [4.35]by observing at smaller indentation depth the Hertzian model shows agreement with experimental results from visco-elastic materials. The AFAM quantitative modulus measurement on Epon862 is shown to be not affected by its visco-elastic properties due to the time delay made in the experiments (~30 seconds to achieve a constant contact stiffness). Determining the contact resonance response over shorter time durations would allow measurement of the viscous response of the epoxy. Nevertheless, the elastic quantitative modulus characterization on polymer materials by AFAM has been shown is sufficient to determine the elasticity features for the visco-elastic materials when delay time is appropriately chosen.

4.5 . Conclusions

Based on the same contact stiffness measurements, the proposed power law type of body revolution model is found to be able to provide more consistent quantitative elastic modulus results than the Hertzian and flat punch models over the range of different applied loads. This advantage will enable the AFAM quantitative technique to be accurately achieved with less applied load desired, and thereby less probe geometry change in measurements. Introducing the probe geometry variation for quantitative determination improves the elastic modulus characterization accuracy. The elastic-plastic contact models based on the probe shapes exhibit different stress-strain response stages for the epoxy in respect to the variation of applied loads, and quantitatively characterize the material with more accurate elastic modulus. The visco-elastic contact was investigated by delayed elasticity and standard linear solid models, and the quantitative elastic modulus coefficients in these models can be quantitatively characterized based on current AFAM set ups. But the accurate determination of damping coefficients in these models, desires the precisely mapping of contact resonance frequency response in number of measurements with a certain time interval.

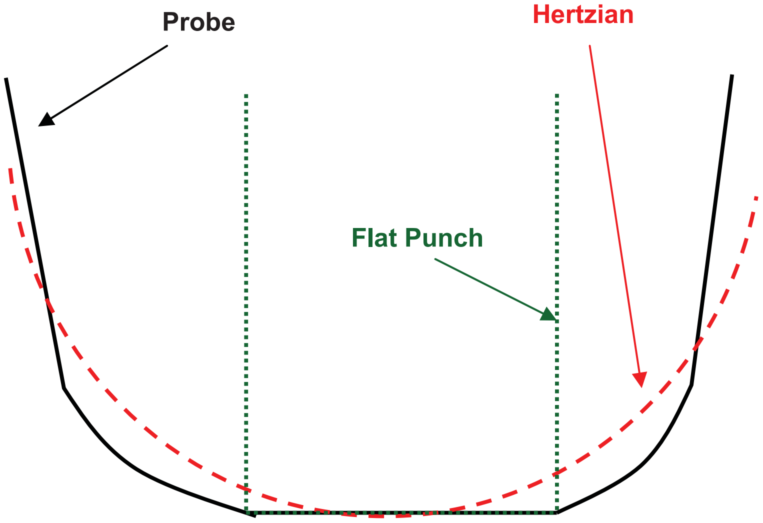

Figure 4.1. Hertzian and flat punch profiles in comparison with real probe profile.

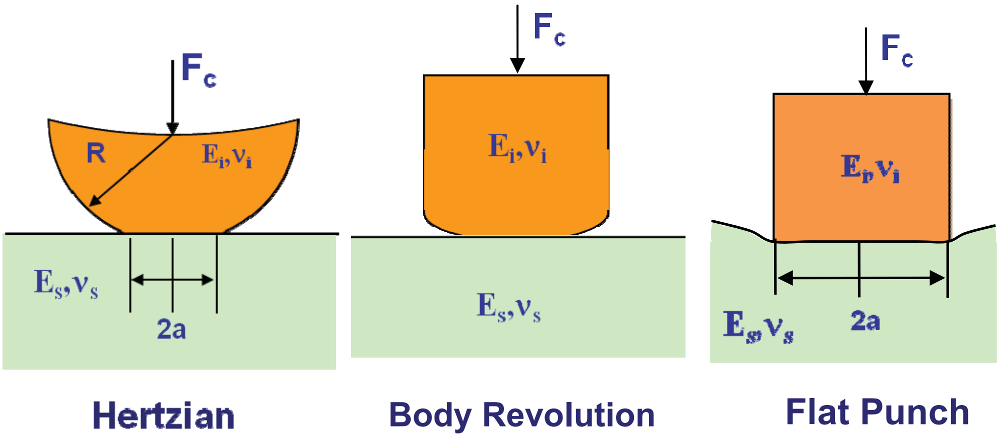

Figure 4.2. Elastic contact models that characterize the geometry features of AFAM probes.

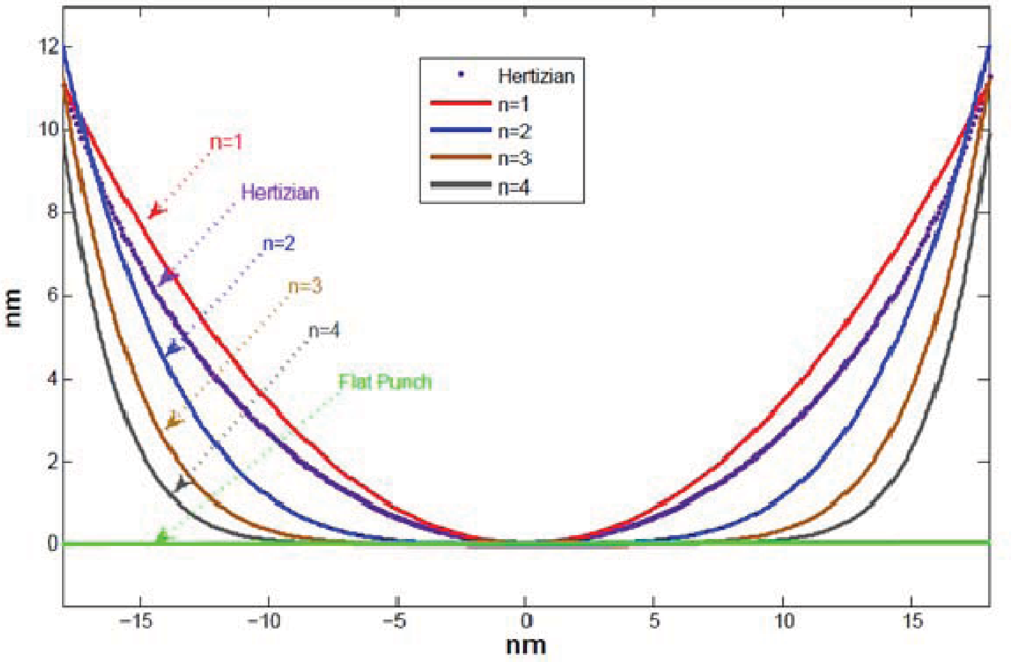

Figure 4.3. Tip Profile curve fitting comparison by different models.

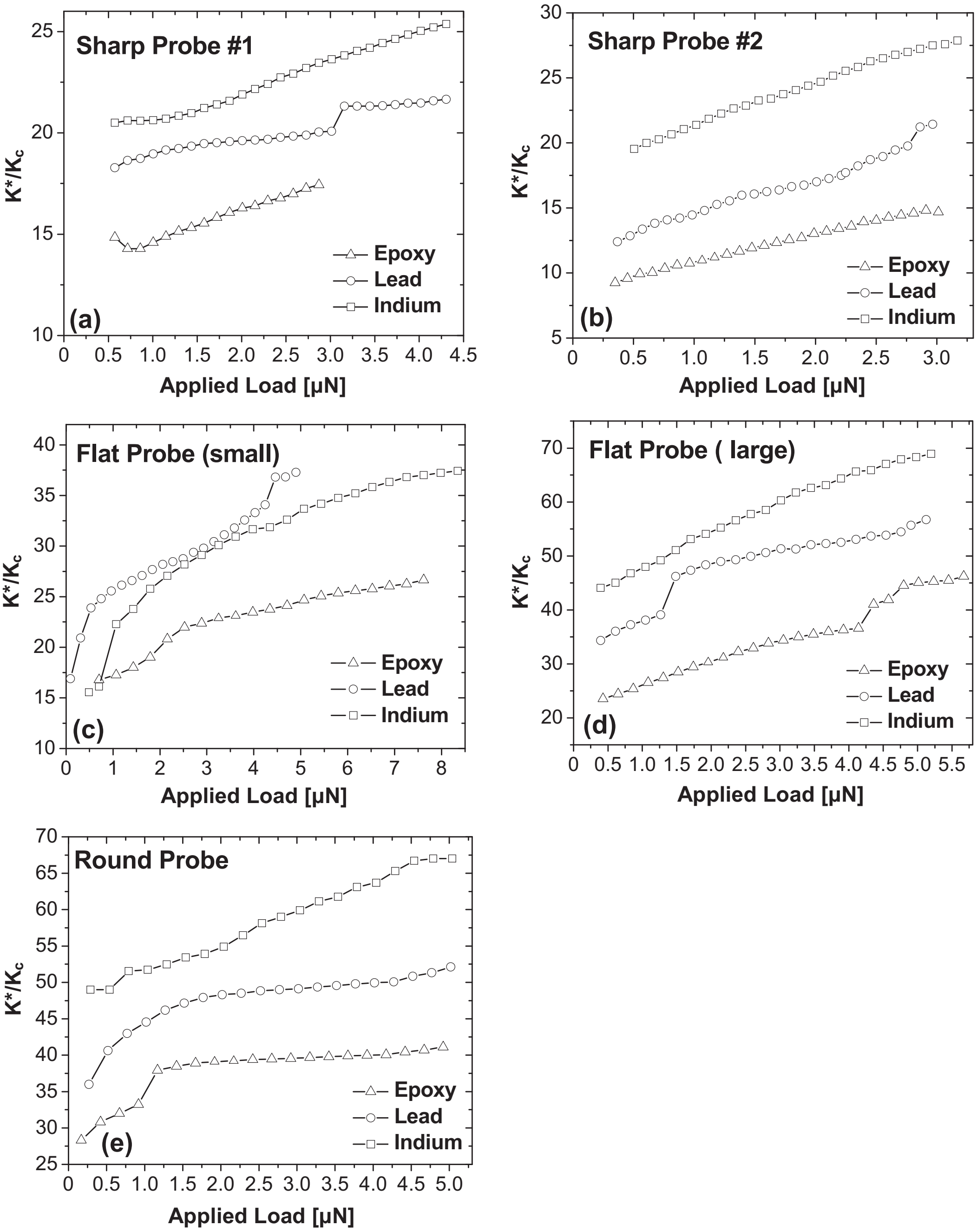

Figure 4.4. Contact Stiffness for a) sharp probe #1, b) sharp probe #2, c) small, flat probe, d) Large flat probe, e) rounded probe.

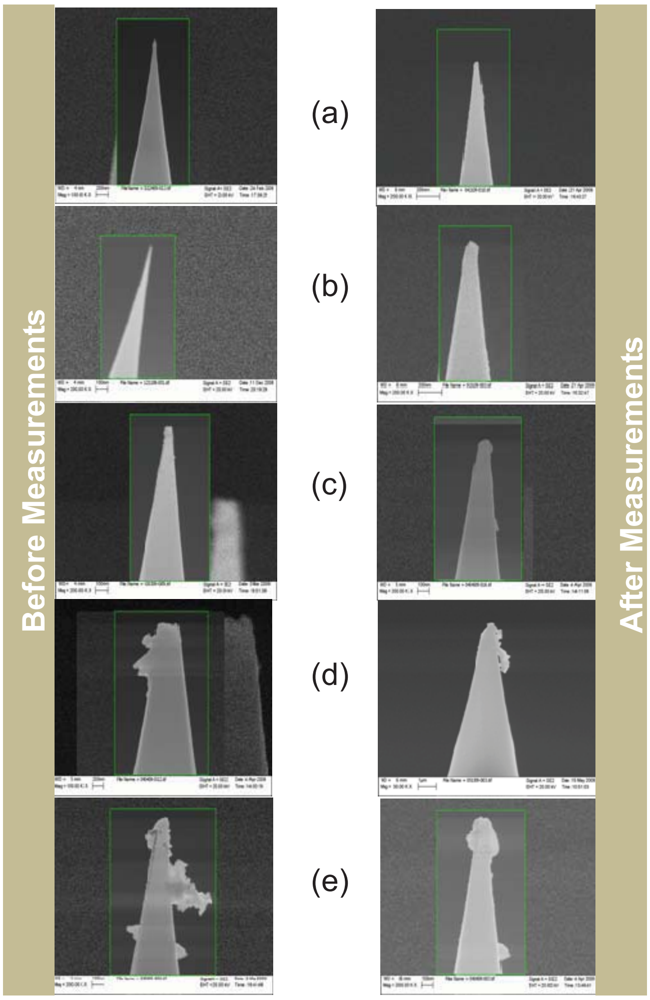

Figure 4.5. SEM images for before and after AFAM measurement a) Sharp Probe #1, b) Sharp Probe #2, c) Small flat Probe, d) Large flat Probe, e) Rounded Probe.

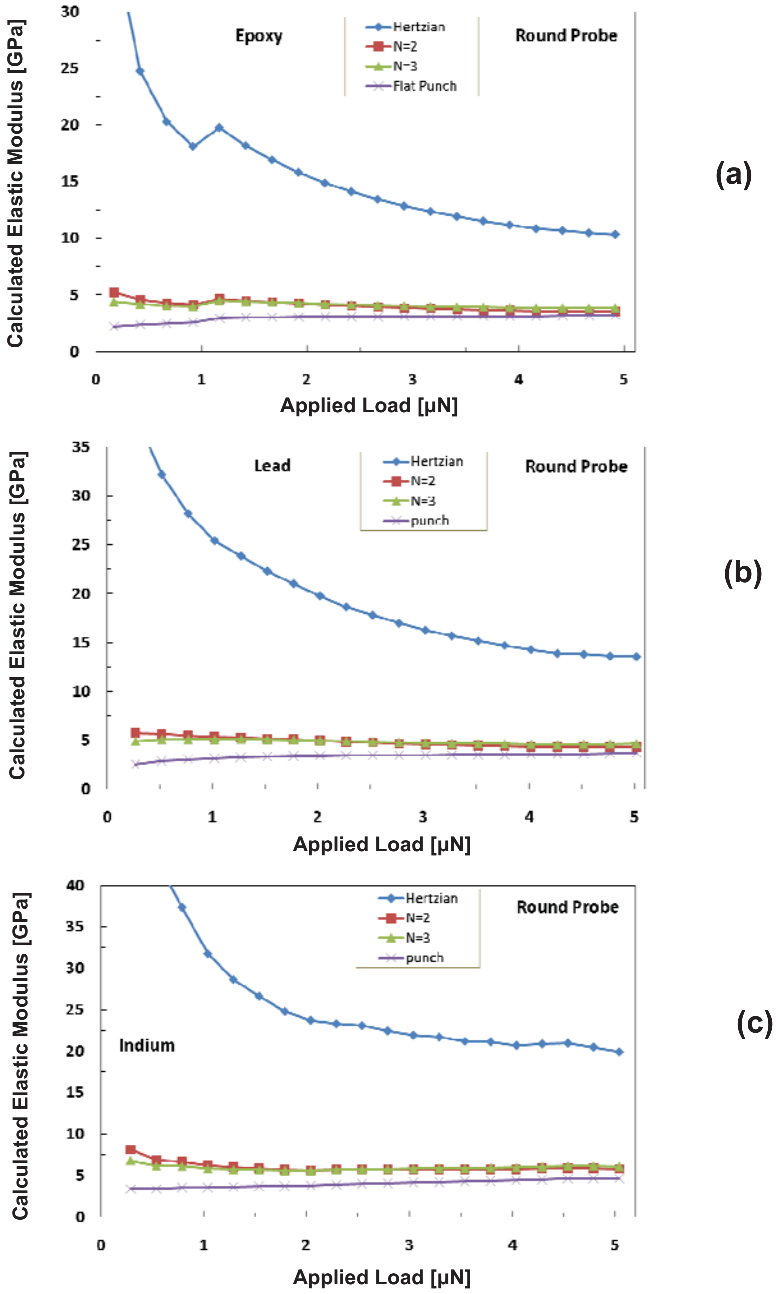

Figure 4.6. Elastic modulus determination by AFAM Round Probe for (a) Epoxy; (b) Lead ; (c) Indium.

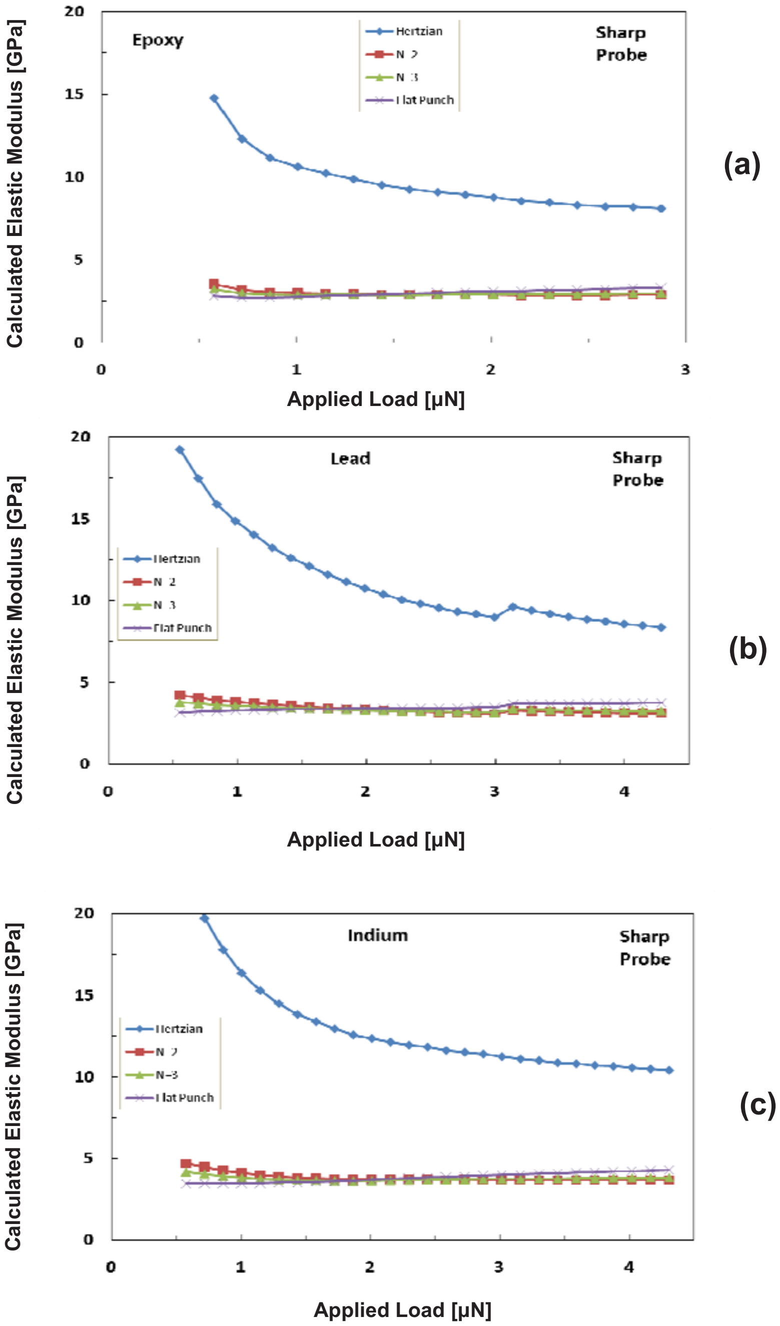

Figure 4.7. Elastic modulus determination by AFAM sharp probe #1 for (a) Epoxy; (b) Lead ; (c) Indium.

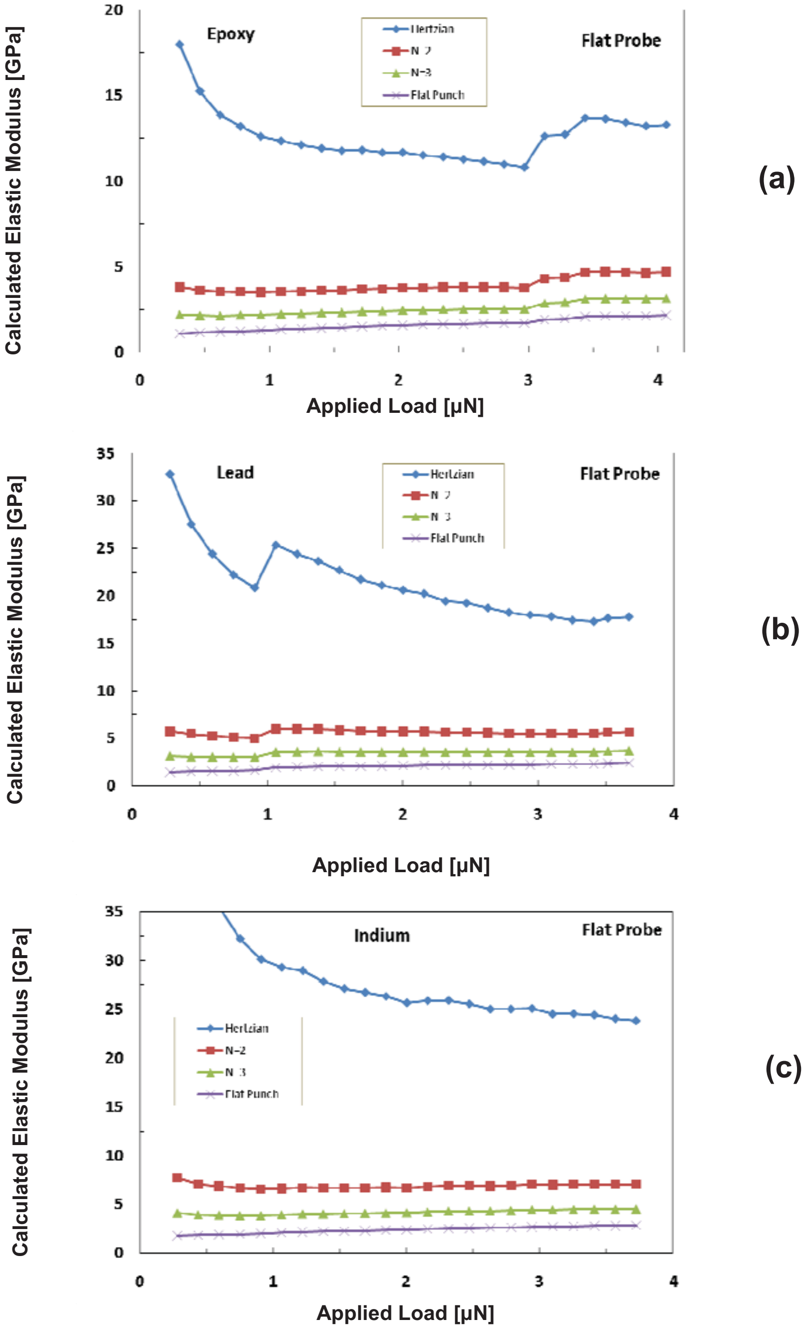

Figure 4.8. Elastic modulus determination by AFAM Large Flat Probe for (a) Epoxy; (b) Lead ; (c) Indium.

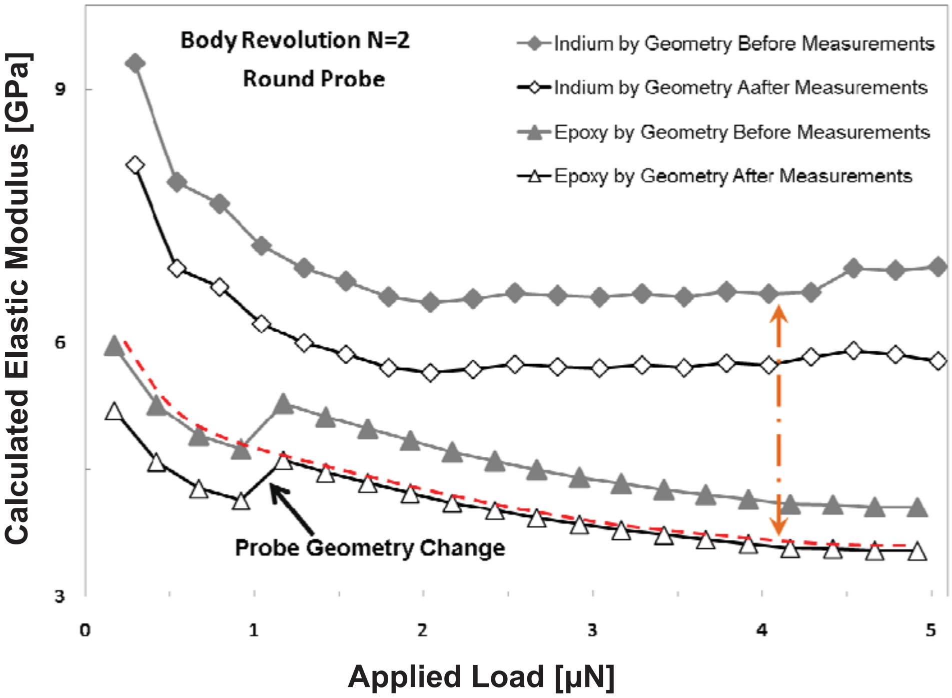

Figure 4.9. Elastic modulus analysis with geometry variation taken into consideration

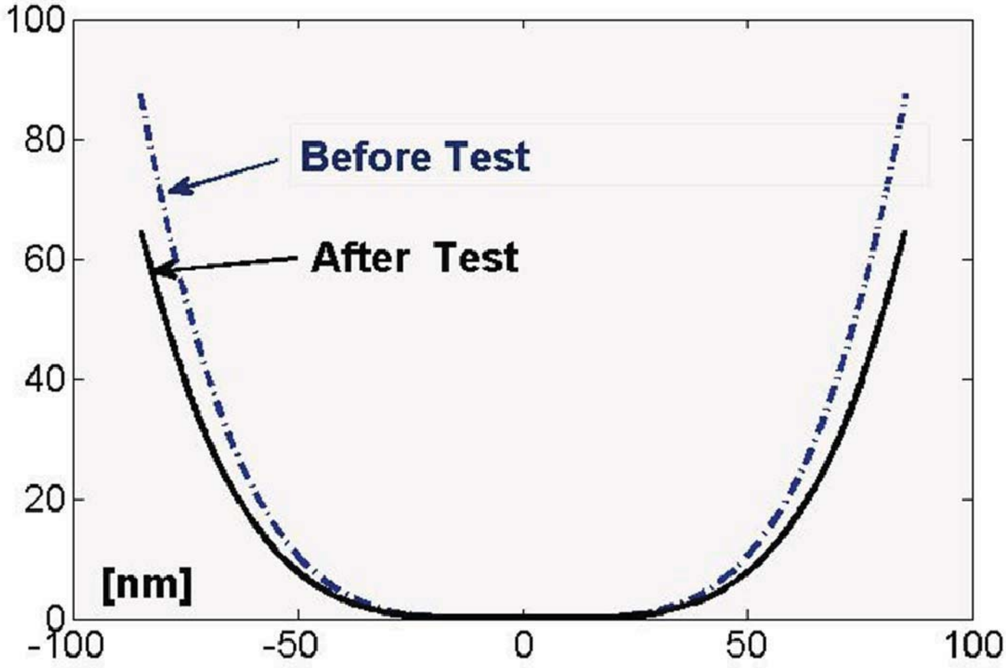

Figure 4.10. Round probe geometry variation characterized by body revolution model

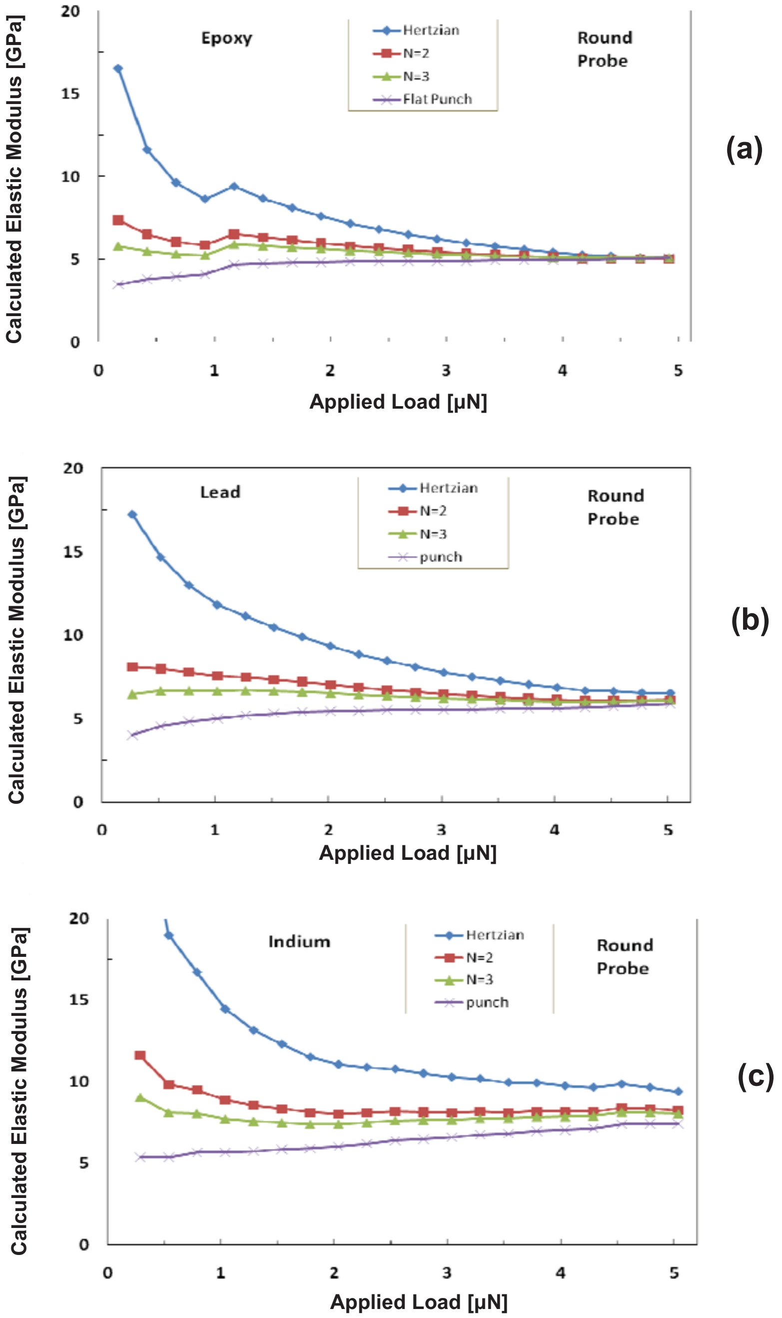

Figure 4.11. Elastic modulus recalculation for (a) Epoxy; (b) Lead; (c) Indium, based upon the round probe geometry that correspondent to 5GPa for epoxy

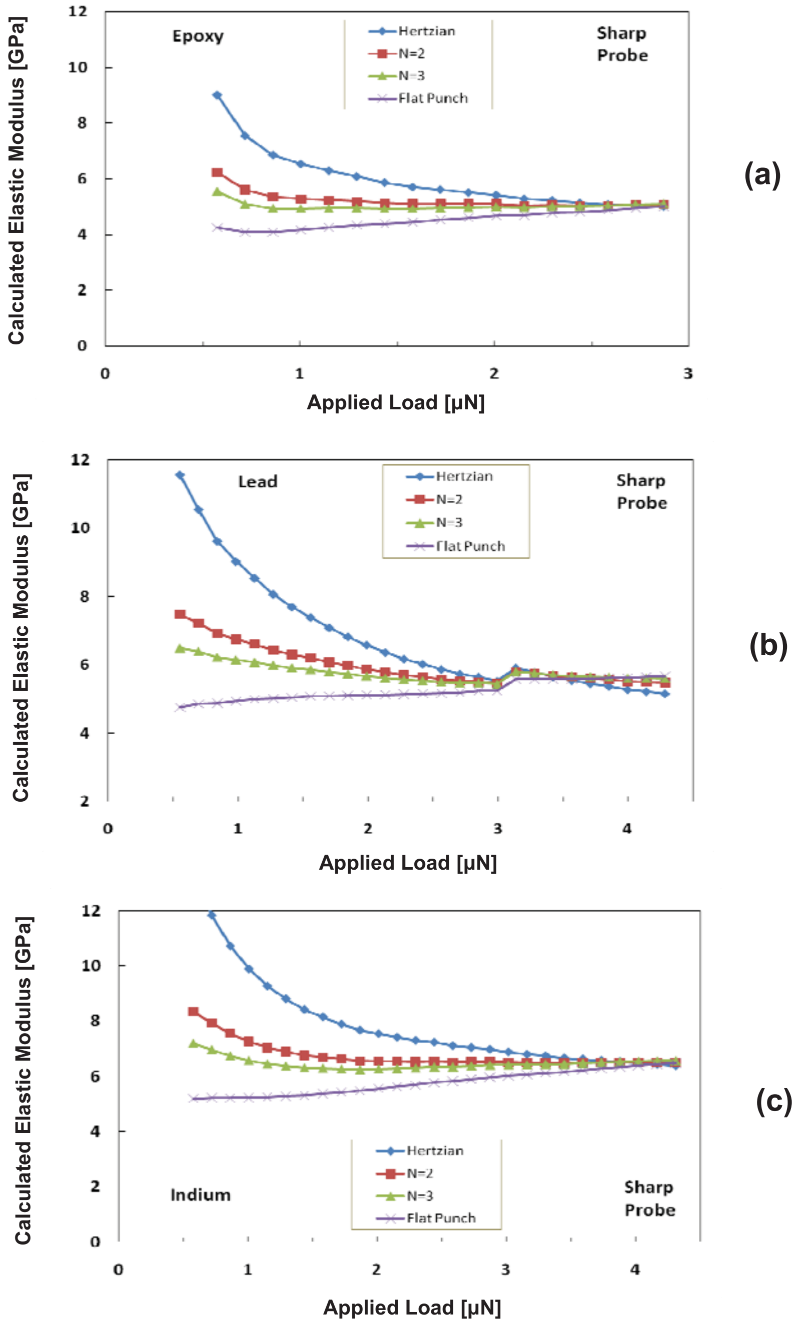

Figure 4.12. Elastic modulus recalculation for (a) Epoxy; (b) Lead; (c) Indium, based upon the sharp probe #1 geometry that correspondent to 5GPa for epoxy

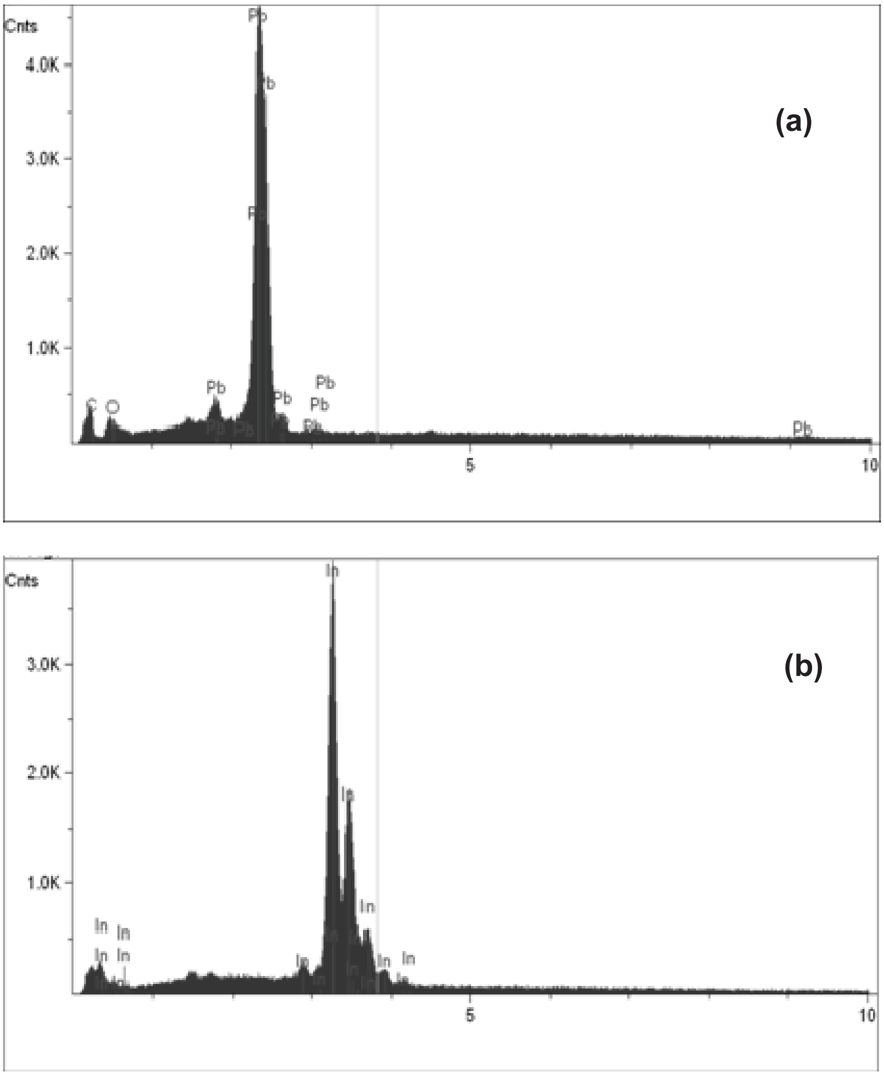

Figure 4.13. EDX measurements on (a) Lead surface (b) indium surface

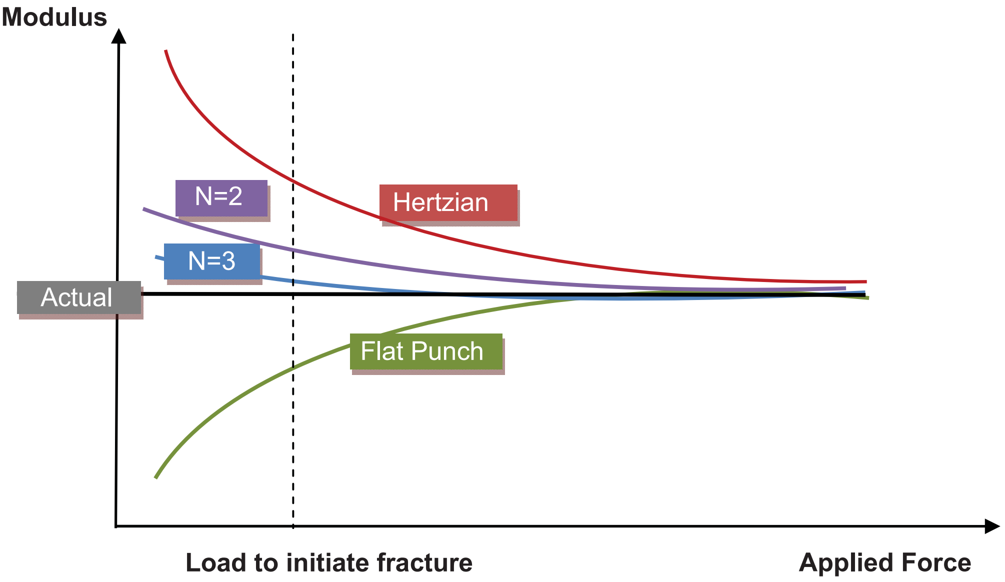

Figure 4.14. Contact mechanics models comparison in quantitative elastic modulus characterization.

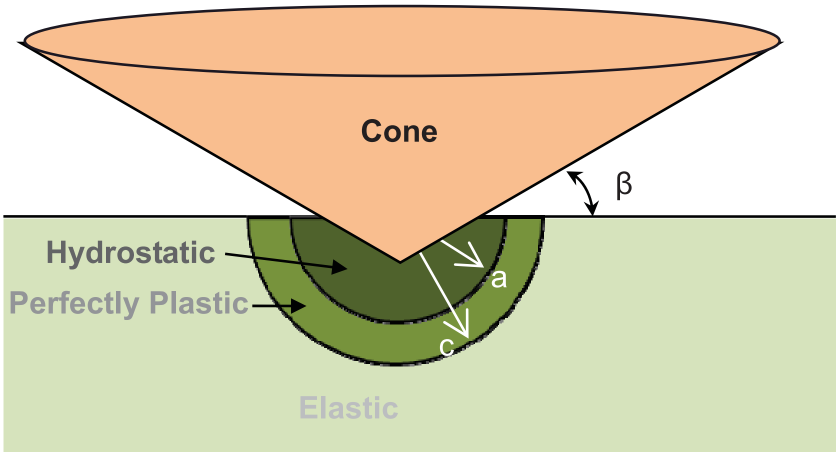

Figure 4.15. Elastic-plastic contact by a cone.

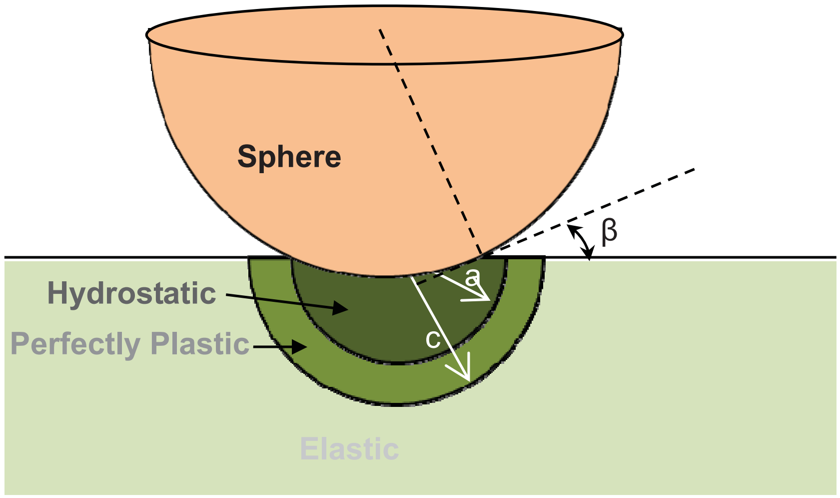

Figure 4.16. Elastic-plastic contact by a sphere.

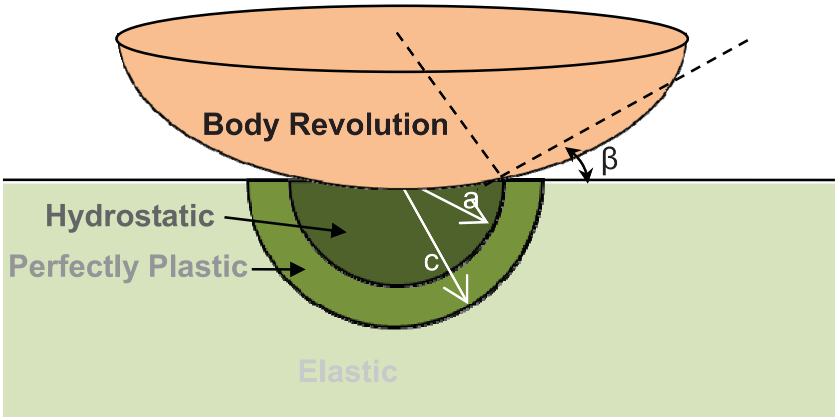

Figure 4.17. Elastic-plastic contact by a power law body of revolution.

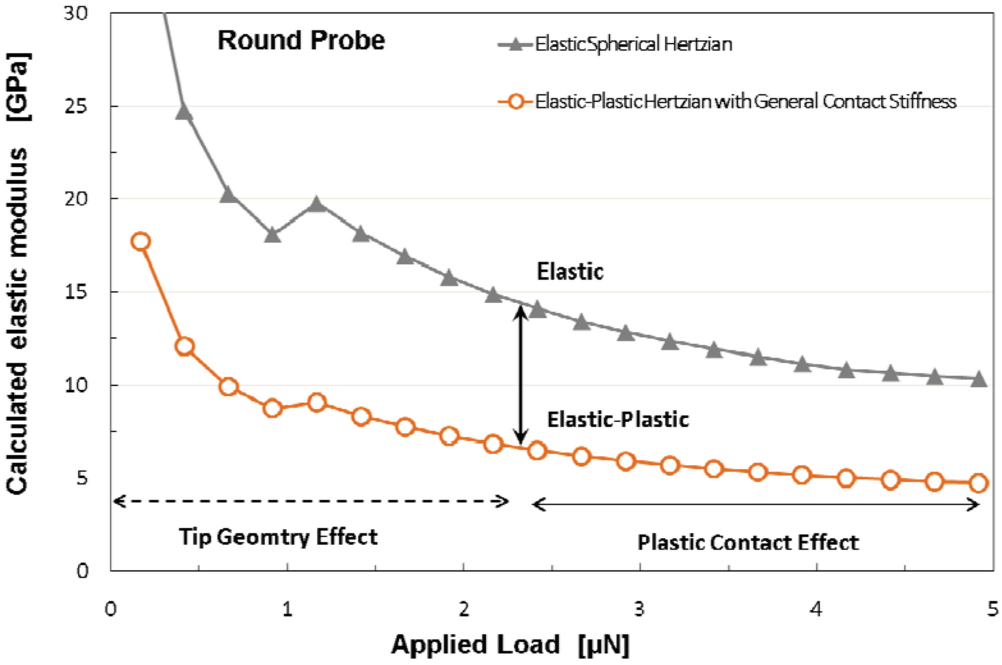

Figure 4.18. Round probe elastic and elastic-plastic contact comparison on epoxy.

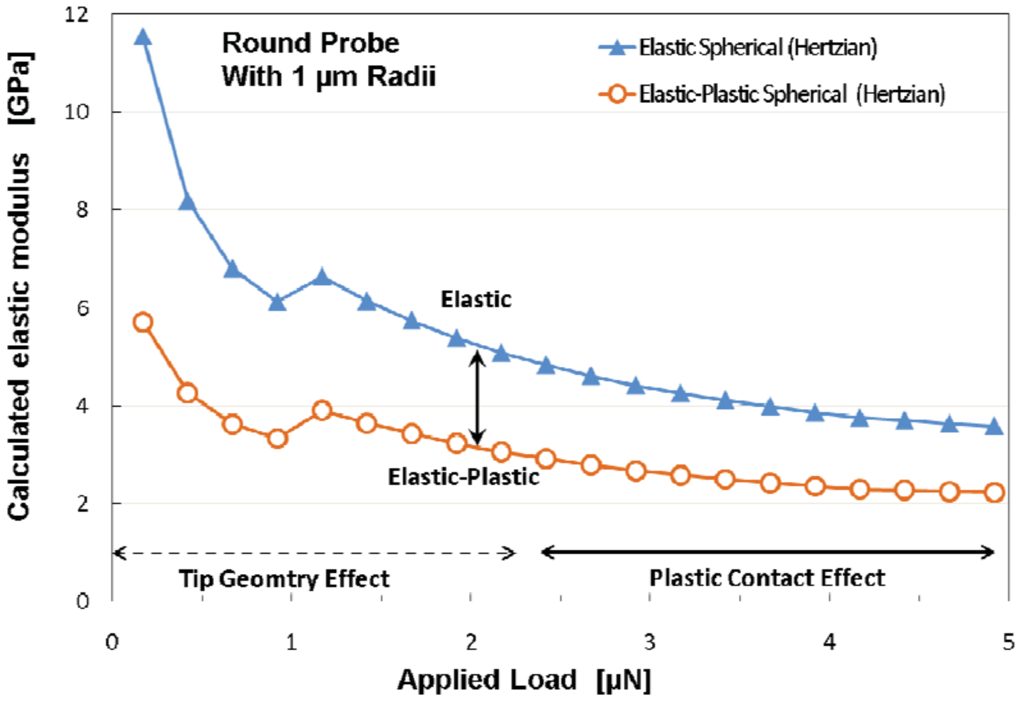

Figure 4.19. Round probe elastic and elastic-plastic spherical Hertzian contact comparison on epoxy with 1micron probe radii assumption.

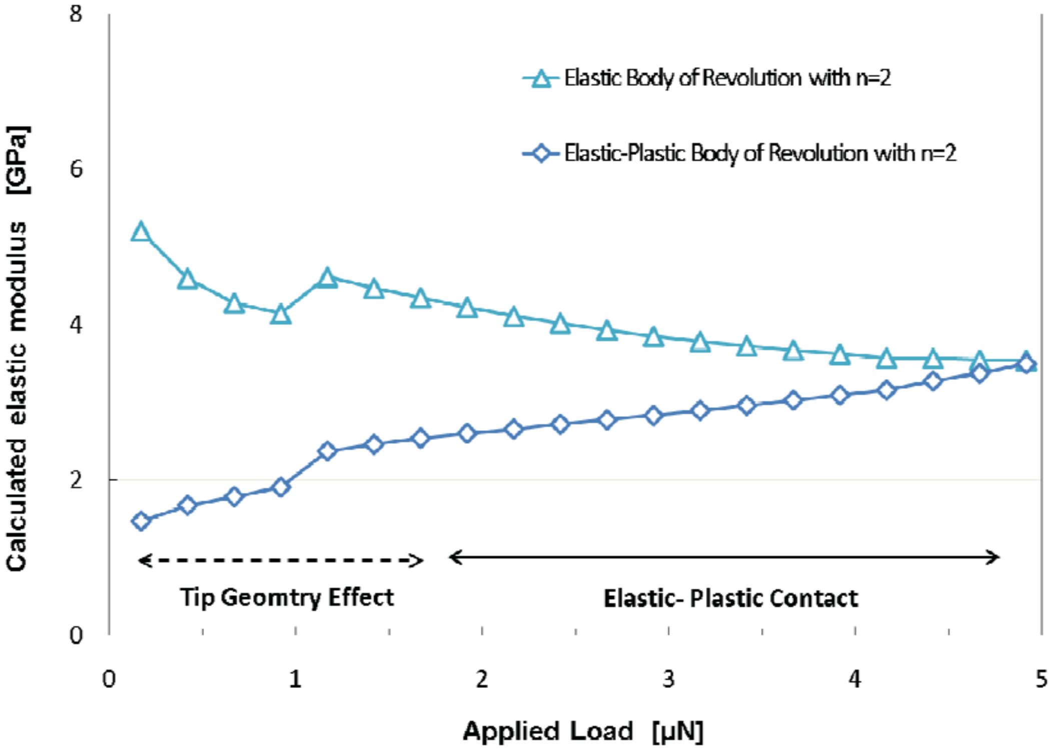

Figure 4.20. Round probe elastic and elastic-plastic body of revolution contact comparison on epoxy with n=2.

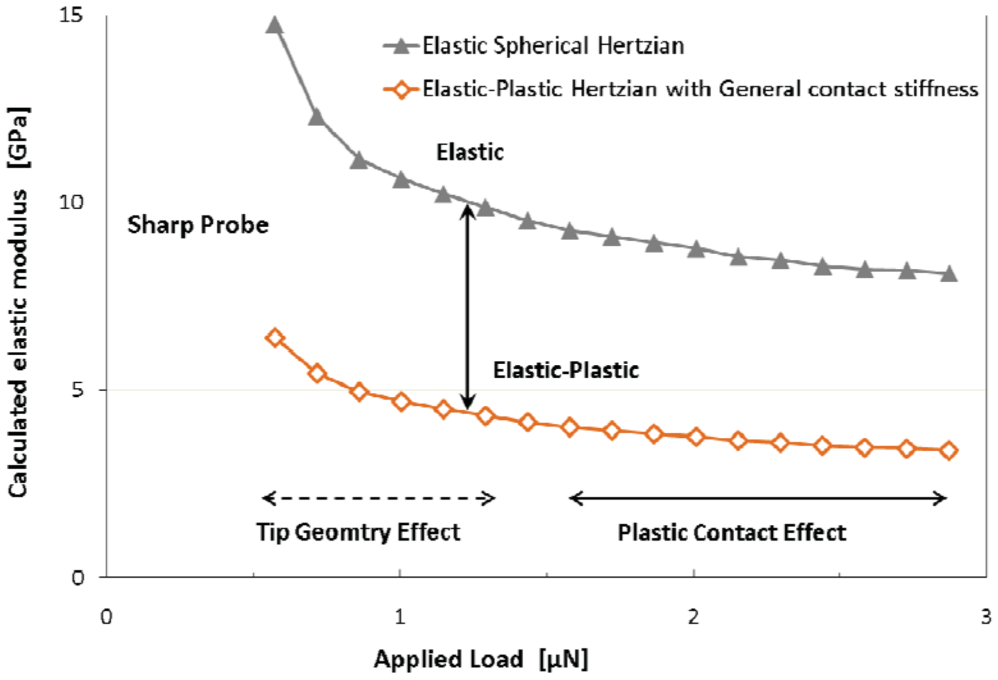

Figure 4.21. Sharp Probe #1spherical elastic Hertzian and elastic-plastic Hertzian with general contact stiffness contacts comparison on epoxy.

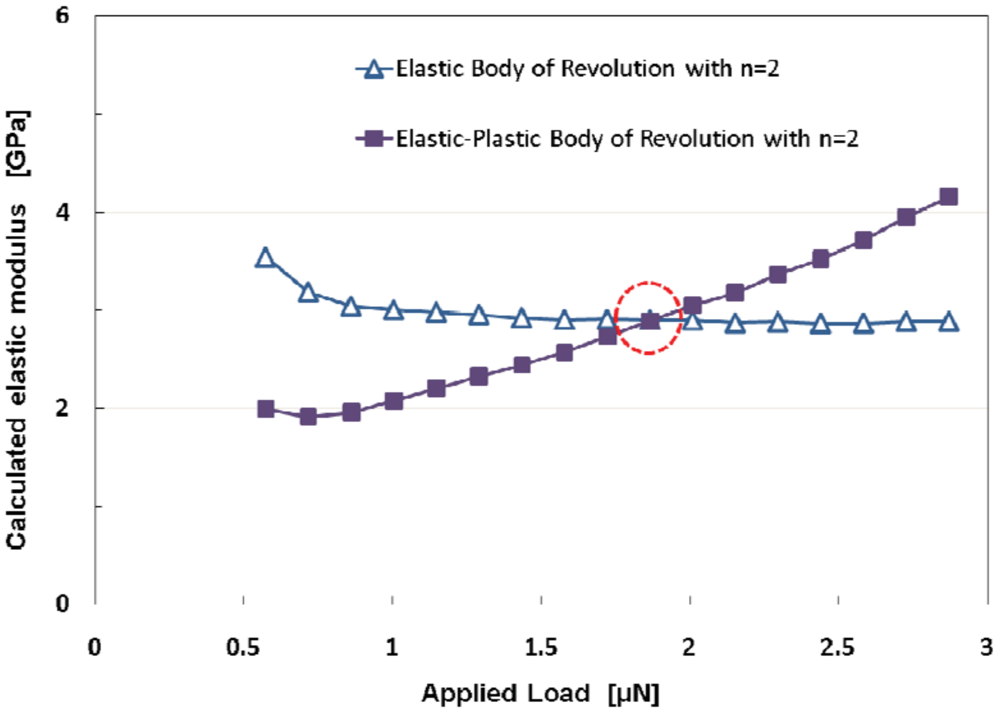

Figure 4.22. Sharp Probe #1 elastic and elastic-plastic body of revolution contact comparison on epoxy with n=2.

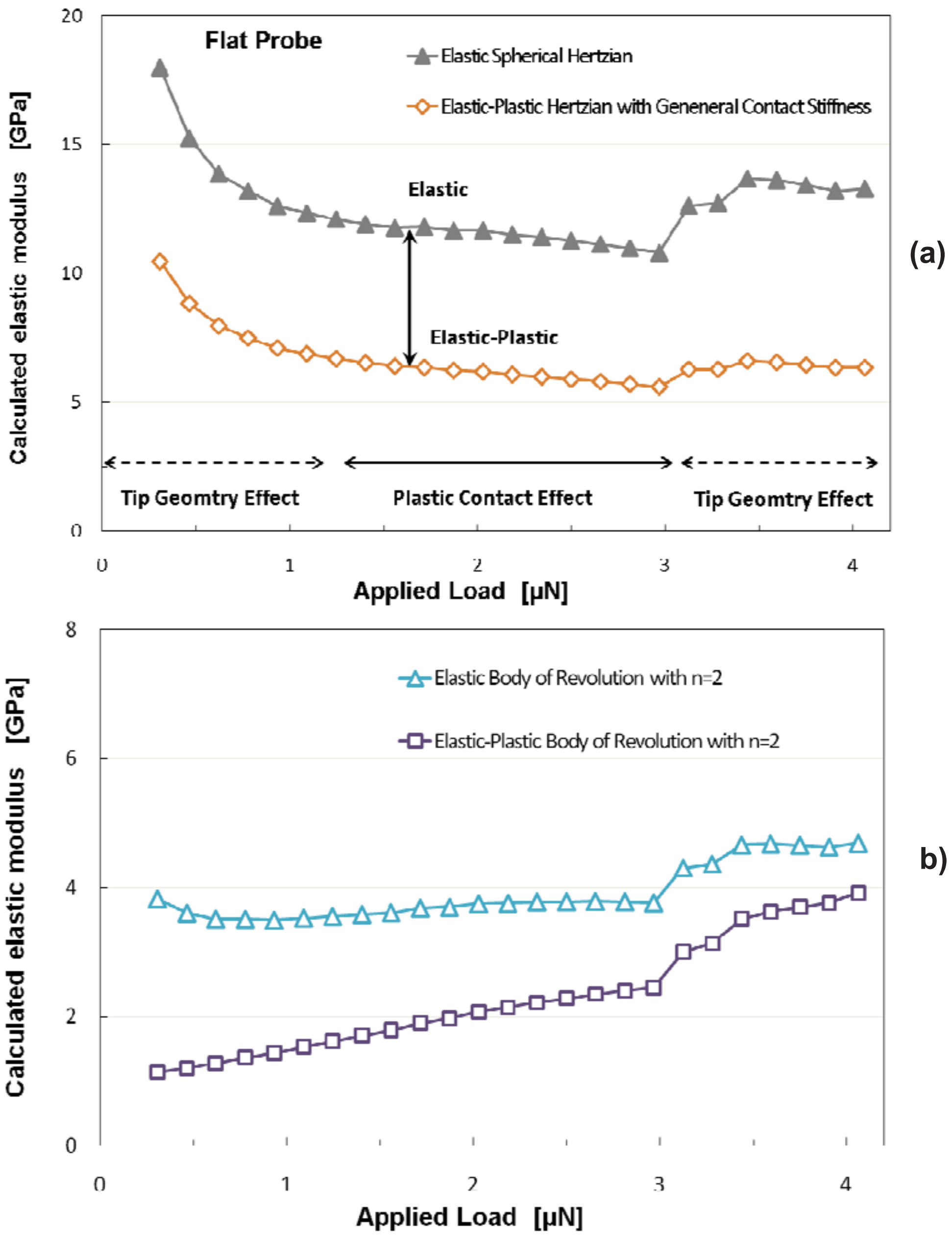

Figure 4.23. Flat probe (a) spherical elastic Hertzian and elastic-plastic Hertzian with general contact stiffness contacts comparison on epoxy (b) elastic and elastic-plastic body of revolution contact comparison on epoxy with n=2.

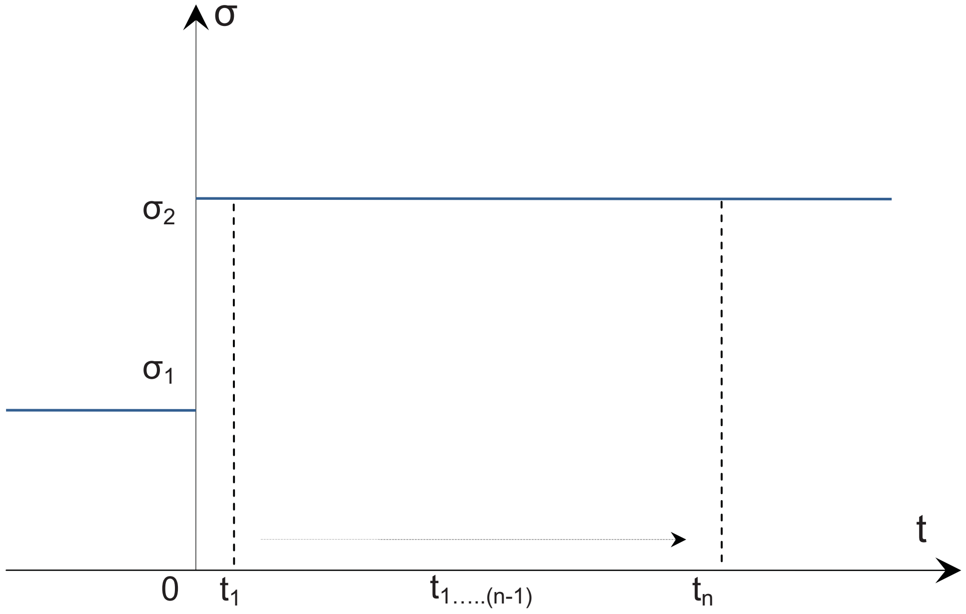

Figure 4.24. Applied load condition in AFAM measurement.

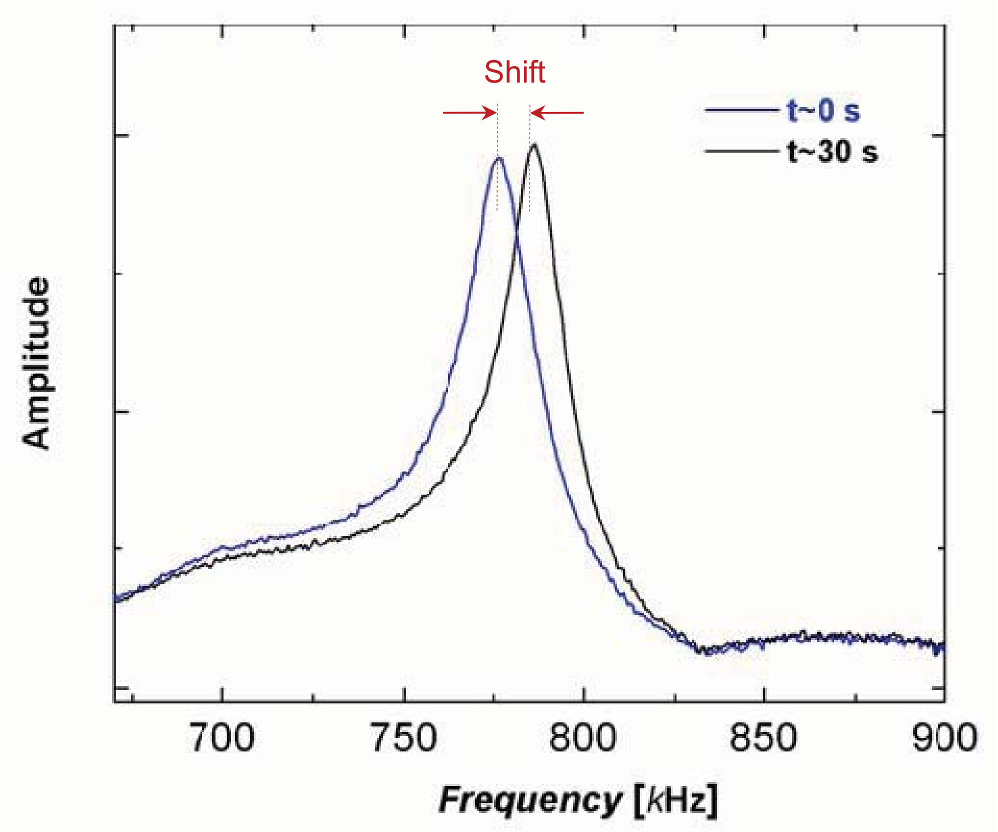

Figure 4.25. The AFAM 1st order contact resonance frequency shift over measurement time.

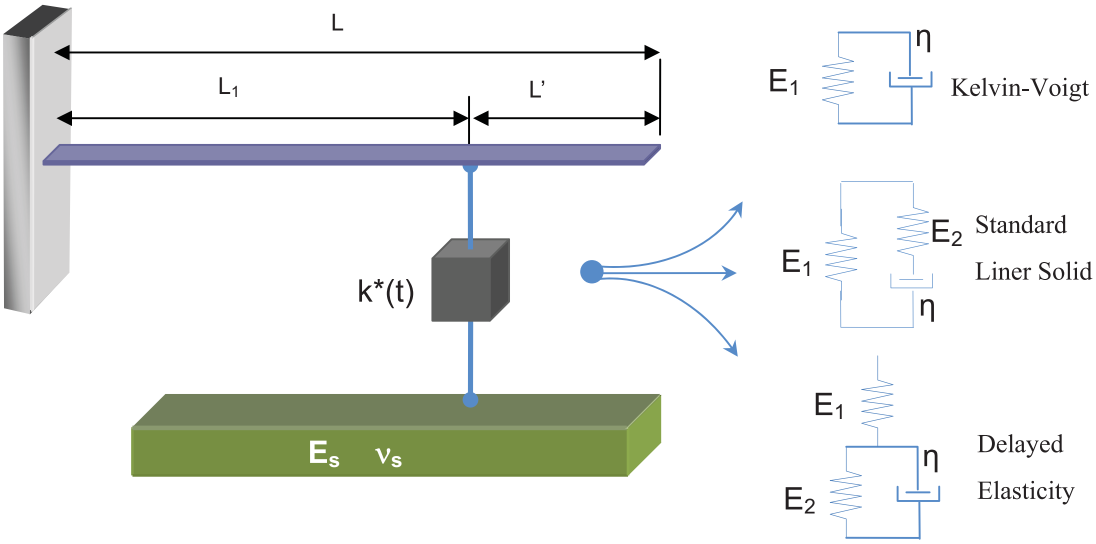

Figure 4.26. Visco-elastic contact models for AFAM

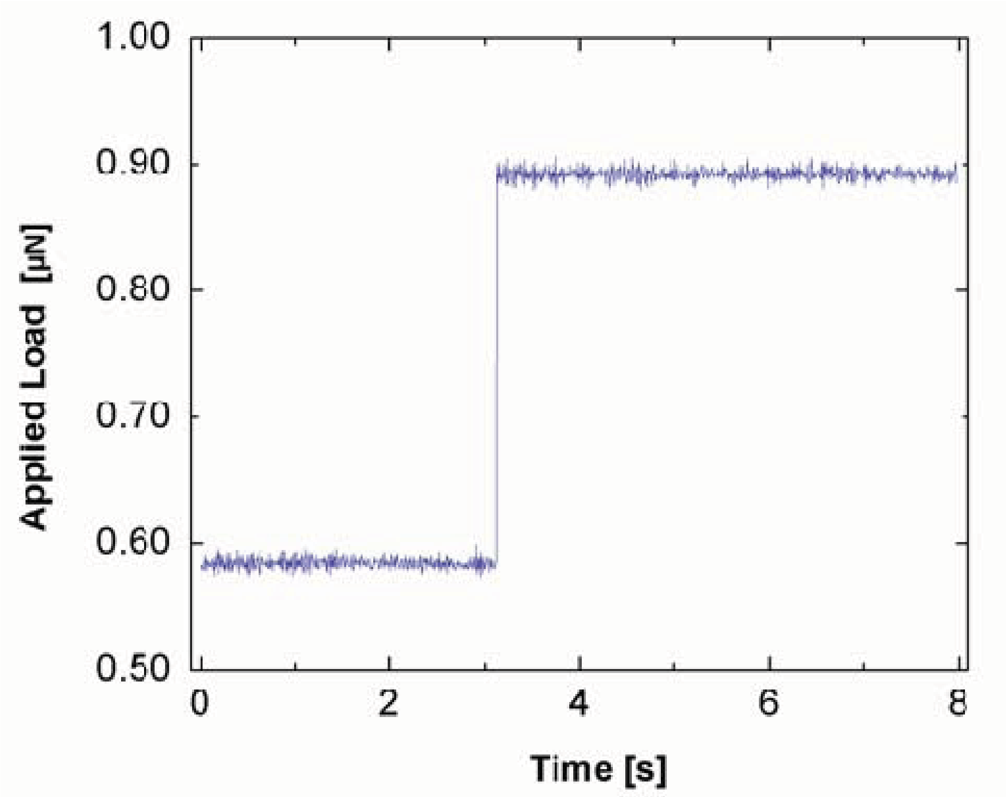

Figure 4.27. The applied load from the cantilever deflection as an indication of small vibration amplitude in presence of the entire cantilever deflection.

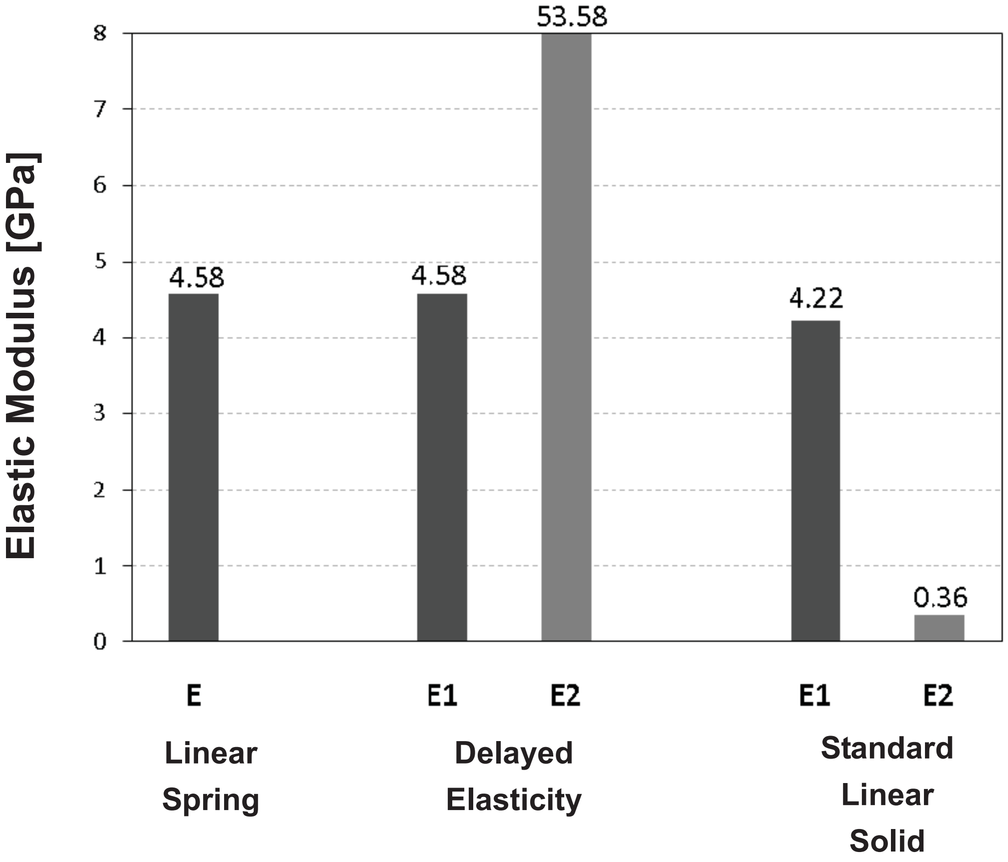

Figure 4.28. Modulus characterization for three different models with the same contact resonance response.

4.6. References

[4.1] Rabe U, Amelio S, Kester E, Scherer V. Hirsekorn S, Arnold W. Quantitative determination of contact stiffness using atomic force acoustic microscopy. Ultrasonics. 2000;38(1-8):430-7.

[4.2] Hurley Dc, Shen K, Jennett Nm, Turner Ja. Atomic force acoustic microscopy methods to determine thin-film elastic properties. J Appl Phys. 2003;94(4):2347-54.

[4.3] K.L. Johnson. Contact Mechanics. Cambridge: Cambridge University Press; 1985.

[4.4] Yamanaka K, Nakano S. Quantitative elasticity evaluation by contact resonance in an atomic force microscope. Appl Phys A Mat Sci Process. 1998;66:313–7.

[4.5] Wei Zhao, Raman P. Singh, Chad S. Korach. Effects of environmental degradation on near-fiber nanomechanical properties of carbon fiber epoxy composites. Composites Part A. 2009;40(5):675-8.

[4.6] L.S. Dongmo, J.S. Villarubia, S.N. Jones, T.B. Renegar, M.T. Postek, J.F. Song. Experimental test of blind tip reconstruction for scanning probe microscopy Ultramicroscopy. 2000;85:141-53.

[4.7] M. Kopycinska-Mu¨ Ller, R.H. Geiss, P. Rice, D.C. Hurley, In: S.V.Kalinin, B. Goldberg, L.M. Eng, B.D. Huey. Scanning-probe and other novel microscopies of local phenomena in nanostructured materials. Materials Research Symposium Proceedings 838E. Warrendale, PA, electronic only publication. p. O-10.6.

[4.8] Malgorzata Kopycinska-Muller, Roy H. Geiss, Donna C. Hurley. Contact mechanics and tip shape in AFM-based nanomechanical measurements. Ultramicroscopy. 2006;106:466-74.

[4.9] F. Stahl, B. Cretin, In: J.P. Jones (Ed.). Acoustical Imaging. Plenum, New York, 1995.

[4.10] Hutter JI, Bechhoefer J. Calibration of atomic-force microscope tips. Rev Sci Instrum 1993;64(7):1868-73.

[4.11] J. Jamari, D. J. Schipper. Experimental Investigation of Fully Plastic Contact of a Sphere Against a Hard Flat. Journal of Tribology. 2006;128:230-5.

[4.12] L. Kogut, I. Etsion. Elastic-plastic contact analysis of a sphere and a rigid flat. Journal of Applied Mechanics. 2002;69:657-62.

[4.13] N. Ye, K. Komvopoulos. Indentation Analysis of Elastic-Plastic Homogeneous and Layered Media: Criteria for Determining the Real Material Hardness. Journal of Tribology. 2003;125:685-9.

[4.14] P.A.Yuya, D.C. Hurley, J.A. Turner. Contact-resonance atomic force microscopy for viscoelasticity. Journal of Applied Physics. 2008;104(074916):1-7.

[4.15] Win-Jin Chang, Chao-Ming Lin, Jenn-Fa Lee, Shu-Lian Lin. Determination of damping force between atomic force microscope tips and sample using an inverse methodology. Physics Letters A. 2005;343:79-84.

[4.16] Daniel Rupp, Ute Rabe, Sigrun Hirsekorn, Walter Arnold. Nonlinear contact resonance spectroscopy in atomic force microscopy. Journal of Physics D: Applied Physics. 2007;40:7136-45.

[4.17] C-Y Hui, J.M. Baney, E.J. Kramer. Contact Mechanics and Adhesion of Viscoelastic Spheres. Langmuir 1998;14:6570-8.

[4.18] M. L. Oyen. Analytical techniques for indentation of viscoelastic materials. philosophical Magazine 2006;86:5625-41.

[4.19] Wright Ob, Nishiguchi N. Vibrational dynamics of force microscopy: effect of tip dimensions. Appl Phys Lett. 1997;71(5):626-8.

[4.20] Rabe U, Janser K, Arnold W. Vibrations of free and surface-coupled atomic force microscope cantilevers: theory and experiment. Rev Sci Instrum. 1996;67(9):3281-93.

[4.21] E. Steuermann. On Hertz Contact Problem with Finite Friction. Journal of Elasticity. 1939(5):297.

[4.22] Egon Wiberg, Nils Wiberg, Arnold Frederick Holleman. Inorganic chemistry: Academic Press; 2001.

[4.23] Poh Chieh Benny Poon. A critical appraisal of nanoindentation with application to elastic-plastic solids and soft materials. Pasadena, California: CALIFORNIA INSTITUTE OF TECHNOLOGY; 2009.

[4.24] Yongwu Zhao, David M. Maietta, L. Chang. An asperity microcontact model incorporating the transition from elastic deformation to fully plastic flow. Journal of Tribology. 2000;122:86-93.

[4.25] Yeau-Ren Jeng, Pei-Ying Wang. An Elliptical Microcontact Model Considering Elastic, Elastoplastic, and Plastic Deformation. Journal of Tribology. 2003;125:232-40.

[4.26] C. Hardy, C. N. Baronet, G. V. Tordion. The elasto-plastic indentation of a half-space by a rigid sphere. INTERNATIONAL JOURNAL FOR NIJMERICAL METHODS IN ENGINEERING. 1971;3:451-62.

[4.27] I.M.Ward, D.W. Hadley. An Introduction to The Mechanical Properties of Solid Polymers: JOHN WILLEY & SONS; 1993.

[4.28] Taher A. Alabed, Osama M. Abuzeid, Mahmoud Barghash. A linear viscoelastic relaxation-contact model of a flat fractal surface: a Maxwell-type medium. Int J Adv Manuf Technol. 2008;39:423-30.

[4.29] D. C. Hurley, J. A. Turner. Humidity effects on the determination of elastic properties by atomic force acoustic microscopy. JOURNAL OF APPLIED PHYSICS.

2004;95(5):2403-7.

[4.30] Hirsekorn S, Rabe U, Arnold W. Theoretical description of the transfer of vibrations from a sample to the cantilever of an atomic force microscope. Nanotechnology. 1997;8(2):57-66.

[4.31] C. Y. Hui, Y. Y. Lin, J. M. Baney. The mechanics of tack: viscoelastic contact on a rough surface. J Polym Sci B: Polym Phys. 2000;38:1485-95.

[4.32] W.H. Yang. The contact problem for viscoelastic bodies. Transactions of the ASME, Series E, Journal of Applied Mechanics,. 1966;33:395-404.

[4.33] Wesley K. Chua, Michelle L. Oyen. Viscoelastic Properties of Membranes Measured by Spherical Indentation. Cellular and Molecular Bioengineering. 2009;2(1):49–56.

[4.34] Shen Xiaojun, Yi Sung, Lallit Anand, Zeng Kaiyang, . Studies on Nano-indentation of Polymeric Thin Films Using Finite Element Methods. Advanced Materials for Micro- and Nano-Systems. 2002(1).

[4.35] Ch. Srinivasa Rao, C. Eswara Reddy. An FEM Approach into Nanoindentation on Linear Elastic and Visco Elastic Characterization of Soft Living Cells. International Journal of Nanotechnology and Applications. 2008;2(1):55-68.

Chapter Five

Conclusions

In this study, nanomechanical characterization have been performed on the surface of human dental enamel and carbon fiber reinforced composites using atomic force acoustic microscopy. The AFAM technique is shown to provide high resolution quantitative measurements on the prism and sheath regions of the enamel microstructure and fiber-matrix interphases. The contact resonance frequency of the AFM cantilever is used to calculate the elastic modulus with a vibrational beam model in conjunction with Hertzian contact analysis.

For tooth enamel, prism modulus was consistently observed to be larger than the sheath, both in premolar and molar. The elastic modulus of the enamel transverse surface were found to be smaller than either of the inner or outer enamel surfaces, and this had been consistently observed in both the prism and sheath regions. In the transverse surface, the regions closer to outer surface are consistently found to possess slightly higher elastic modulus than the one close to DEJ region.

For carbon fiber reinforced composites, elastic modulus of samples were determined by AFAM as a function of environment and time of exposure using accelerated degradation. The mechanical property degradation, based on chemical analysis from FTIR and Raman, is due to the hydrolysis of the C-O-C and Epoxide bonding. The salt water environment condition is found to be more severe than deionized water in degradation for the fiber-matrix interface, which coincides with the macro-scale experiment results from fracture toughness measurements. The fiber-matrix interphase region had been quantitatively studied by AFAM techniques, and the elastic modulus was shown to decrease as a function of the degradation exposure, while interphase dimensions remained constant.

In the contact mechanics effects on AFAM analysis, the power law shaped body of revolution model exhibits a better approximation for the probe geometry, and is able to generate more accurate quantitative results. Probes that began with a large, flat end tends to become rounded after measurements, likewise, new AFM tips were found to blunt after usage. The location of the probe geometry change can be determined from measured contact stiffness variations, and will affect the quantitative results. The analysis based on the geometry variation results in a more accurate quantitative modulus. The fresh tip is more difficult to be measured accurately due to difficulties to characterize its sharp features, in addition to its easy to fracture nature. Though it is expected that the elastic modulus will remain constant for the entire load range, while none of studied model can follow, the quantitative determination based on body of revolution model is shown least affected by applied load. Indium was found as a good reference material to assist in quantitative analysis of epoxy.

The elastic-plastic contact analysis is shown be able to provide a better prediction than the elastic analysis. Elastic modulus is predicted more accurately due to the consideration of the plastic contact strains at higher loads the, though at lower loads the geometry effect is dominate. For a sharper AFM probe, effect of the elastic-plastic contact occurs at lower loads. Elastic-plastic contact analysis for a power-law body of revolution model provided unreasonable quantitative determination for a power order of two, however, as the order increases, it will be less affected by the applied loads and provide good quantitative approximations.

It can be concluded that the major materials properties from different visco-elastic models are not so different from the Hertzian elastic analysis. The AFAM quantitative modulus measurement on Epon862 is not shown to be much affected by its visco-elastic properties, unless the damping parameter is needed to be characterized. The contact resonance based quantitative determination methods is not able to characterize the visco effects of the materials accurately.

Nevertheless, the elastic quantitative modulus characterization on polymer materials by AFAM has been shown is sufficient to approximate the elasticity features for the visco-elastic materials.

References

Infrared and Raman Characteristic Group Frequencies: Tables and Charts New York, John Wiley & Sons.

A. Gruverman, D. Wu, B.J. Rodriguez, S.V. Kalinin, S. Habelitz (2007). "High-resolution imaging of proteins in human teeth by scanning probe microscopy." Biochemical and Biophysical Research Communications 352: 142-146.

AEW, M. (1967). Structural and Chemical Organization of Teeth, Vol. II, Academic Press

AR, T. (1994). Oral Histology: Development, Structure, and Function, Mosby.

B117-03, A. (2003). Standard Practice for Operating Salt Spray (Fog) Apparatus.

Bajaj D, Arola DD (2009). "On the R-curve behavior of human tooth enamel." Biomaterials 30: 4037-4046.

Bajaj D, A. D. (2009). "On the R-curve behavior of human tooth enamel." Biomaterials 30: 4037-4046.

Balooch G, Marshall GW, Marshall SJ, Warren OL, Asif SA, Balooch M (2004). "Evaluation of a new modulus mapping technique to investigate microstructural features of human teeth." J. Biomech 37: 1223-1232.

BW, D. (1998). Materials science for dentistry. Hong Kong, BW Darvell.

C-Y Hui, J.M. Baney, E.J. Kramer (1998). "Contact Mechanics and Adhesion of Viscoelastic Spheres." Langmuir 14: 6570-6578.

C. HARDY, C. N. BARONET, G. V. TORDION (1971). "The elasto-plastic indentation of a half-space by a rigid sphere." INTERNATIONAL JOURNAL FOR NIJMERICAL METHODS IN ENGINEERING 3: 451-462.

C. Y. HUI, Y. Y. LIN, J. M. BANEY (2000). "The mechanics of tack: viscoelastic contact on a rough surface." J Polym Sci B: Polym Phys 38: 1485-1495.

Ch. Srinivasa Rao, C. Eswara Reddy (2008). "An FEM Approach into Nanoindentation on Linear Elastic and Visco Elastic Characterization of Soft Living Cells." International Journal of Nanotechnology and Applications 2(1): 55-68.

Christopher N. Young, William R Scott, Guy M Connelly, Clive R. Clayton, Richard Granata (2009). Relating Matrix Chemistry and Laser Fluorescence in Thermally Damaged Polymer Composites. ASME (IMECE). Lake Buena Vista, Florida, US. IMECE2009-11788.

Cuy JL, Mann AB, Livi KJ, Teaford MF, Weihs TP (2002). "Nanoindentation mapping of the mechanical properties of human molar tooth enamel." Arch. Oral Biol 47: 281-291.

D. C. Hurley, J. A. Turner (2004). "Humidity effects on the determination of elastic properties by atomic force acoustic microscopy." JOURNAL OF APPLIED PHYSICS 95(5): 2403-2407.

D. C. Hurley, K. Shen, N. M. Jennett, J. A. Turner (2003). "Atomic force acoustic microscopy methods to determine thin-film elastic properties." JOURNAL OF APPLIED PHYSICS 94(4): 2347-2354.

Daniel Rupp, Ute Rabe, Sigrun Hirsekorn, Walter Arnold (2007). "Nonlinear contact resonance spectroscopy in atomic force microscopy." Journal of Physics D: Applied Physics 40: 7136-7145.

E. van Overbeke, V. Carliera, J. Devaux, J.T. Carter, P.T. McGrail, R. Legras (2000). "The use of Raman spectroscopy to study the reaction between an amine-terminated thermoplastic and epoxy resins." Polymer 41: 8241-8245.

Egon Wiberg, Nils Wiberg, Arnold Frederick Holleman (2001). Inorganic chemistry, Academic Press.

Eorgakopoulos Andreas, Iordanidis Andreas, Kapina Victoria (2003). "Study of low rank greek coals using FTIR spectroscopy." Energy sources 25: 995-1005.

Erik T. Thostenson , S. Z., Tsu-Wei Chou (2009). "Processing and electrical properties of carbon nanotube/vinyl ester nanocomposites." Composites Science and Technology 69: 801–804.

F. Stahl, B. Cretin, in: J.P. Jones (Ed.) (1995). Acoustical Imaging. Plenum, New York, .

FR, J. (1999). Durability of Reinforced Plastics in Liquid Environments. Reinforced Plastics Durability. P. G, Woodhead Publishing Company: 70-110.

G. Z. XIAO, M. E. R. SHANAHAN (1997). "Water Absorption and Desorption in an Epoxy Resin with Degradation
" Journal of Polymer Science: Part B: Polymer Physics 35: 2659-2670.

Gao S-L, Mäder E (2002). "Characterisation of interphase nanoscale property variations in glass fiber reinforced polypropylene and epoxy resin composites." Composites: Part A 33: 559-576.

Gardiner, D.J (1989). Practical Raman spectroscopy, Springer-Verlag.

Ge J, Cui FZ, Wang XM, Feng HL (2005). "Property variations in the prism and organic sheath within enamel by nanoindentation." Biomaterials 26: 3333-3339.

Gheorghe Stan, William Price (2006). "Quantitative measurements of indentation moduli by atomic force acoustic microscopy using a dual reference method." REVIEW OF SCIENTIFIC INSTRUMENTS 77(103707): 1-6.

GS, S. (1984). Environmental Effects on Composite Materials, Technomic.

Habelitz S, Marshall SJ, Marshall GW, Balooch M (2001). "The functional width of the dentino-enamel junction determined by AFM-based nanoscratching." J. of Struct. Biol 135: 294-301.

Habelitz S, Marshall SJ, Marshall GW, Balooch M (2001). "Mechanical properties of human dental enamel on the nanometer scale." Arch. Oral Biol 46: 173-183.

Higgins, B. A. (2006). CARBON NANOFIBER-POLYMER COMPOSITES FOR ELECTRONIC APPLICATIONS, University of Akron. Doctor of Philosophy.

Hilmar Koerner, Devesh Misra, Ashley Tan, Lawrence Drummy, Peter Mirau, Richard Vaia (2006). "Montmorillonite-thermoset nanocomposites via cryo-compounding." Polymer 47: 3426–3435.

Hirsekorn S, Arnold W (1998). "High-resolution materials characterization by conventional and near-field acoustic microscopy." Ultrasonics 36(1-5): 491-498.

Hirsekorn S, Rabe U, Arnold W (1997). "Theoretical description of the transfer of vibrations from a sample to the cantilever of an atomic force microscope." Nanotechnology 8(2): 57-66.

Hodzic A, Kim JK, Lowe AE, Stachurski, ZH (2004). "The effects of water aging on the interphase region and interlaminar fracture toughness in polymer-glass composites." Composites Science and Technology 64(13-14): 2185-2195.

Hodzic A, Stachurski ZH, Kim JK (2000). "Nano-indentation of polymer-glass interfaces Part I. Experimental and mechanical analysis." Polymer 41(18): 6895-6905.

Hurley DC, Geiss RH, Kopycinska-Muller M, Muller J, Read DT, Wright JE, Jennett NM, Maxwell AS (2005). "Anisotropic elastic properties of nanocrystalline nickel thin films." Journal of Materials Research 20(5): 1186-1193.

Hurley DC, Geiss RH, Kopycinska-Muller M, Muller J, Read DT, Wright JE, Jennett NM, Maxwell AS (2005). "Anisotropic elastic properties of nanocrystalline nickel thin films." Journal of Materials Research 20: 1186-1193.

Hurley DC, Shen K, Jennett NM, Turner JA (2003). "Atomic force acoustic microscopy methods to determine thin-film elastic properties." Journal of Applied Physics 94(4): 2347-2354.

Hurley DC, Shen K, Jennett NM, Turner JA (2003). "Atomic force acoustic microscopy methods to determine thin-film elastic properties." J Appl Phys 94(4): 2347-2354.

Hutter JL, Bechhoefer J (1993). "Calibration of atomic-force microscope tips." Review of Scientific Instruments 64: 1868-1873.

Hutter JL, Bechhoefer J (1993). "Calibration of atomic-force microscope tips." Rev Sci Instrum 64(7): 1868-1873.

I.M.Ward, D.W. Hadley (1993). An Introduction to The Mechanical Properties of Solid Polymers, JOHN WILLEY & SONS.

IR, S. (1997). "A three-dimensional finite-element model of prismatic enamel: a re-appraisal of the data on the Young's modulus of enamel." J. Dent. Res. 76: 1690-1697.

J, B. (1999). Biological performance of materials. New York, Marcel Dekker.

J. Jamari, D. J. Schipper (2006). "Experimental Investigation of Fully Plastic Contact of a Sphere Against a Hard Flat." Journal of Tribology 128: 230-235.

Johnson, K. L. (1985). Contact Mechanics. Cambridge, Cambridge University Press.

Kazuto Tanaka, Kohji Minoshima, Witold Grela, Kenjiro Komai (2002). "Characterization of the aramid/epoxy interfacial properties by means of pull-out test and influence of water absorption." Composites Science and Technology 62: 2169-2177.

Kester E, Rabe U, Presmanes L, Tailhades P, Arnold W (1999). "Measurement of mechanical properties of nanoscaled ferrites using atomic force microscopy at ultrasonic frequencies." Nanostructured Materials 12: 779-782.

Kester E, Rabe U, Presmanes L, Tailhades P, Arnold W (1999). "Measurement of mechanical properties of nanoscaled ferrites using atomic force microscopy at ultrasonic frequencies." Nanostructured Materials 12(5-8): 779-782.

Kim JK, Hodzic A (2003). "Nanoscale characterisation of thickness and properties of interphase in polymer matrix composites." Journal Of Adhesion 79(4): 383-414.

KL, J. (1985). Contact Mechanics, Cambridge University Press.

Kulowitch P., Scott, W. R. (2003). "Detection of Thermal Damage in Epoxy-Based Composites Using Laser Pumped Fluorescence." Nondestr. Charact. Mater. XI, Proc. Int. Symp., 11th: 545-553.

L, H. (1966). Composite Materials. Amsterdam, Elsevier.

L. Kogut, I. Etsion (2002). "Elastic-plastic contact analysis of a sphere and a rigid flat." Journal of Applied Mechanics 69: 657-662.

L. Largeau, G.Patriarche, A. Riviere, J.P.Riviere, E.LE Bourhis (2004). "Indentation punching through thin (011) InP." Journal of Materials Science(39): 943-949.

L.S. Dongmo, J.S. Villarubia, S.N. Jones, T.B. Renegar, M.T. Postek, J.F. Song (2000). "Experimental test of blind tip reconstruction for scanning probe microscopy " Ultramicroscopy 85: 141-153.

Li-Rong Bao, Albert F.Yee (2002). "Effect of temperature on moisture absorption in a bismaleimide resin and its carbon fiber composites." Polymer 43: 3987-3997.

Liao K, Shultheisz CR, Hunston DL, Brinson LK (1998). "Long-term Durability of Fiber-Reinforced Polymer-Matrix Composite Materials for Infrastructure Applications: A Review." SAMPE Journal of Advanced Materials 30(4): 3-40.

Libor Brabec, Petr Bohac, Martin Stranyanek, Radim Ctvrtlik, Milan Kocirik (2006). "Hardness and elastic modulus of silicalite-1 crystal twins." Microporous and Mesoporous Materials 94: 226-233.

Lionel T. Keene, Gary P. Halada, Clive R. Clayton (2005). "Failure of navy coating systems 1: chemical depth profiling ofartificially and naturally weathered high-solids aliphatic poly(ester-urethane) military coating systems." Progress in Organic Coatings 52: 173–186.

Lionel T. Keene, M. Jaime Vasquez, Clive R. Clayton, Gary P. Halada (2005). "Failure of navy coating systems 2: failure pathways of artificially weathered navy coating systems applied to chromate conversion coated AA2024-T3 substrates." Progress in Organic Coatings 52: 187–195.

Lionel T. Keene, Thomas Fiero, Clive R. Clayton, Gary P. Halada, David Cardoza, Tom Weinacht (2005). "On the use of femtosecond laser ablation to facilitate spectroscopic depth profiling of heterogeneous polymeric coatings." Polymer Degradation and Stability 89: 393-409.

Lippert F, Parker DM, Jandt KD (2004). "In vitro demineralization/remineralization cycles at human tooth enamel surfaces investigated by AFM and nanoindentation." J. Colloid Interf. Sci 280(442-448).

Lirong Bao, Albert F. Yee (2002). "Moisture diffusion and hygrothermal aging in bismaleimide matrix carbon fiber composites—part I: uni-weave composites." Composites Science and Technology 62: 2099-2110.

M. Kopycinska-Mu¨ ller, R.H. Geiss, P. Rice, D.C. Hurley, in: S.V.Kalinin, B. Goldberg, L.M. Eng, B.D. Huey Scanning-probe and other novel microscopies of local phenomena in nanostructured materials. Materials Research Symposium Proceedings 838E, Warrendale, PA, electronic only publication.

Mader E, Grundke K, Jacobasch Hj, Wachinger G, (1994). "Surface Interphase And Composite Property Relations In Fiber-Reinforced Polymers." Composites Science and Technology 25(7): 739-744.

Malgorzata Kopycinska-Muller, Roy H Geiss, Donna C. Hurley (2006). "Contact Mechanics and Tip Shape in AFM-based Nanomechanical Measurements." Ultramicroscopy(106): 466-474.

Malgorzata Kopycinska-Muller, Roy H. Geiss, Donna C. Hurley (2006). "Contact mechanics and tip shape in AFM-based nanomechanical measurements." Ultramicroscopy 106: 466-474.

Mallégol, J., , Gardette, Jean-Luc, Lemaire, Jacques (1999). "Long-term behavior of oil-based varnishes and paints I. Spectroscopic analysis of curing drying oils." Journal of the American Oil Chemists' Society 10: 967-976.

Maria Partini, Roberto Pantani (2007). "FTIR analysis of hydrolysis in aliphatic polyesters." Polymer Degradation and Stability 92: 1491-1497.

Mary P. Walker, Paulette Spencer, J. David Eick (2003). " Mechanical property characterization of resin cement after aqueous aging with and without cyclic loading." Dental Materials 19: 645-652.

Meckel AH, Griebstein WJ, Neal RJ (1962). Ultrastructure of fully calcified human dental enamel. In Tooth enamel, its composition, properties and fundamental structure (eds. Stack MV, Fearnhead RW), John Wright.

Meckel AH, Griebstein WJ, Neal RJ (1965). "Structure of mature human dental enamel as observed by electron microscopy." Arch. Oral Biol 10: 775-784.

Miura J, Maeda Y, Nakai H, Zako M (2009). " Multiscale analysis of stress distribution in teeth under applied forces." Dent. Matls 25: 67-73.

N. Ye, K. Komvopoulos (2003). "Indentation Analysis of Elastic-Plastic Homogeneous and Layered Media: Criteria for Determining the Real Material Hardness." Journal of Tribology 125: 685-689.

Nakamura K, Hatakeyama T, Hatakeyama H (1983). "Relationship between hydrogen bonding and bound water in polyhydroxystyrene derivatives." Polymer 24: 871-876.

Naomi Eidelman, Dharmaraj Raghavan, Aaron M. Forster, Eric J. Amis, Alamgir Karim (2004). "Combinatorial Approach to Characterizing Epoxy Curing." Macromol. Rapid Commun 25: 259-263.

Ngwa W, Luo W, Kamanyi A, Fomba KW, Grill W (2005). "Characterization of polymer thin films by phase-sensitive acoustic microscopy and atomic force microscopy: a comparative review." Journal of Microscopy-Oxford 218: 208-218.

Ngwa W, Luo W, Kamanyi A, Fomba KW, Grill W (2005). " Characterization of polymer thin films by phase-sensitive acoustic microscopy and atomic force microscopy: a comparative review." Journal of Microscopy-Oxford 218: 208-218.

OYEN, M. L. (2006). "Analytical techniques for indentation of viscoelastic materials." philosophical Magazine 86: 5625-5641.

P.A.Yuya, D.C. Hurley, J.A. Turner (2008). "Contact-resonance atomic force microscopy for viscoelasticity." Journal of Applied Physics 104(074916): 1-7.

P.K. Aditya, P.K. Sinha (1996). "Moisture Diffusion in Variously Shaped Fiber Reinforced Composites." Computers & Structures 59(1): 157-166.

Park S, Wang DH, Zhang D, Romberg E, Arola D (2008). "Mechanical properties of human enamel as a function of age and location in the tooth." J. of Matls. Sci.: Matls. in Med.(19): 2317-2324.

Piggott, M. (1987). "Water Absorption of Resins and Composites: II. Diffusion in Carbon and Glass Reinforced Epoxies." Journal of Composites Technology and Research 9(4).

Poon, P. C. B. (2009). A critical appraisal of nanoindentation with application to elastic-plastic solids and soft materials. Pasadena, California, CALIFORNIA INSTITUTE OF TECHNOLOGY. Doctor of Philosophy.

Rabe U, Amelio S, Kester E, Scherer V (2000). "Hirsekorn S, Arnold W. Quantitative determination of contact stiffness using atomic force acoustic microscopy." Ultrasonics 38(1-8): 430-437.

Rabe U, Amelio S, Kester E, Scherer V, Hirsekorn S, Arnold W (2000). "Quantitative determination of contact stiffness using atomic force acoustic microscopy." Ultrasonics 38(1-8): 430-437.

Rabe U, Amelio S, Kester E, Scherer V, Hirsekorn S, Arnold W (2000). "Quantitative determination of contact stiffness using atomic force acoustic microscopy." Ultrasonics 38: 430-437.

Rabe U, Arnold W (1994). "Acoustic Microscopy by Atomic-Force Microscopy." Applied Physics Letters 64(12): 1493-1495.

Rabe U, Janser K, Arnold W (1996). "Vibrations of free and surface-coupled atomic force microscope cantilevers: theory and experiment." Rev Sci Instrum 67(9): 3281-3293.

Rabe U, Janser K, Arnold W (1996). "Vibrations of free and surface-coupled atomic force microscope cantilevers: Theory and experiment." Review of Scientific Instruments 67: 3281-3293.

Rabe U, Kopycinska M, Hirsekorn S, Saldana JM, Schneider GA, Arnold W (2002). "High-resolution characterization of piezoelectric ceramics by ultrasonic scanning force microscopy techniques." Journal of Physics D-Applied Physics 35(20): 2621-2635.

Rodriguez BJ, Kalinin SV, Shin J, Jesse S, Grichko V, Thundat T, Baddorf AP, Gruverman A (2006). "Electromechanical imaging of biomaterials by scanning probe microscopy." J. Struct. Biol 153: 151-159.

Shen Xiaojun, Yi Sung, Lallit Anand, Zeng Kaiyang, (2002). "Studies on Nano-indentation of Polymeric Thin Films Using Finite Element Methods." Advanced Materials for Micro- and Nano-Systems(1).

Shimizu D, Macho GA, Spears IR (2005). "Effect of prism orientation and loading direction on contact stresses in prismatic enamel of primates: implications for interpreting wear patterns." Am. J. Phys. Anthop 126: 427-434.

Stabik, J. (2005). "Ageing of laminates in boiling NaCl water solution." Polymer Testing 24: 101–103

Steuermann, E. (1939). "On Hertz Contact Problem with Finite Friction." Journal of Elasticity(5): 297.

Strong, A. B. (2003). Practical Aspects Of Carbon Fiber Surface Treatment And Sizing. Composites Manufacturing,. June.

Taher A. Alabed, Osama M. Abuzeid, Mahmoud Barghash (2008). "A linear viscoelastic relaxation-contact model of a flat fractal surface: a Maxwell-type medium." Int J Adv Manuf Technol 39: 423-430.

Trong-ming Don, J. P. Bell (1998). "Fourier Transform Infrared Analysis of Polycarbonate/Epoxy Mixtures Cured with an Aromatic Amine." Journal of Applied Polymer Science 69: 2395–2407.

VanLandingham, M. R., Dagastine, R. R., Eduljee, R. F., McCullough, R. L., Gillespie, J. W (1999). "Characterization of nanoscale property variations in polymer composite systems: 1. Experimental results." CompositesPart A 30: 75-83.

Wachter E. A., Fisher, W. G., Meyer, K. E. (1996). Laser Induced Fluorescence Imaging of Thermal Damage in Polymer Matrix Composites. Oak Ridge,TN, Oak Ridge National Laboratory.

Wei Zhao, Raman P. Singh, Chad S. Korach (2009). "Effects of environmental degradation on near-fiber nanomechanical properties of carbon fiber epoxy composites." Composites Part A 40(5): 675-678.

Wesley K. Chua, Michelle L. Oyen (2009). "Viscoelastic Properties of Membranes Measured by Spherical Indentation." Cellular and Molecular Bioengineering 2(1): 49–56.

Willems G, Celis JP, Lambrechts P, Braem M, Vanherle G (1993). "Hardness and Young's modulus determined by nanoindentation technique of filler particles of dental restorative materials compared with human enamel." J. Biomed. Matls. Res.(27): 747-755.

Win-Jin Chang, Chao-Ming Lin, Jenn-Fa Lee, Shu-lian Lin (2005). "Determination of damping force between atomic force microscope tips and sample using an inverse methodology." Physics Letters A 343: 79-84.

Wright OB, Nishiguchi N (1997). "Vibrational dynamics of force microscopy: Effect of tip dimensions." Applied Physics Letters 71(5): 626-628.

Wright OB, Nishiguchi N (1997). "Vibrational dynamics of force microscopy: Effect of tip dimensions." Applied Physics Letters 71: 626-628.

Wright OB, Nishiguchi N (1997). "Vibrational dynamics of force microscopy: effect of tip dimensions." Appl Phys Lett 71(5): 626-628.

Xu HHK, Smith DT, Jahanmir S, Romberg E, Kelly JR, Thompson VP, Rekow ED (1998). "Indentation damage and mechanical properties of human enamel and dentin." J. of Dental Res. 77: 472-480.

Xuerong Zhang, James K. Pugh, Philip N. Ross, Jr. (2001). "Evidence for Epoxide Formation from the Electrochemical Reduction of Ethylene Carbonate." Electrochemical and Solid-State Letters 4(6): A82-A84.

Yamanaka K, Nakano S (1998). "Quantitative elasticity evaluation by contact resonance in an atomic force microscope." Applied Physics Materials a- Science & Processing 66: 313-317.

Yamanaka K, Nakano S (1998). "Quantitative elasticity evaluation by contact resonance in an atomic force microscope." Appl Phys A Mat Sci Process 66: 313–317.

Yang, W. H. (1966). "The contact problem for viscoelastic bodies." Transactions of the ASME, Series E, Journal of Applied Mechanics, 33: 395-404.

Yeau-Ren Jeng, Pei-Ying Wang (2003). "An Elliptical Microcontact Model Considering Elastic, Elastoplastic, and Plastic Deformation." Journal of Tribology 125: 232-240.

Ying Wang, Thomas H. Hahn (2007). "AFM characterization of the interfacial properties of carbon fiber reinforced polymer composites subjected to hygrothermal treatments." Composites Science and Technology 67: 92–101.

Yongwu Zhao, David M. Maietta, L. Chang (2000). "An asperity microcontact model incorporating the transition from elastic deformation to fully plastic flow." Journal of Tribology 122: 86-93.

Zhao W, Singh RP, Korach CS (2009). "Effects of environmental degradation on near-fiber nanomechanical properties of carbon fiber epoxy composites." Composites: Part A 40: 675-678.